1-1-2013

The Effect of Bi-Polar Plate and Membrane Materials On Water Transport in PEMFCs

Visarn Lilavivat
University of South Carolina

THE EFFECT OF BI-POLAR PLATE AND MEMBRANE MATERIALS ON WATER TRANSPORT IN PEMFCS

by

Visarn Lilavivat

Bachelor of Engineering
Chulalongkorn University, 2005

Submitted in Partial Fulfillment of the Requirements

For the Degree of Doctor of Philosophy in

Chemical Engineering

College of Engineering and Computing

University of South Carolina

2013

Accepted by:

John W. Van Zee, Major Professor

Sirivatch Shimpalee, Committee Member

Harry J. Ploehn, Committee Member

Xiaodong Li, Committee Member

John W. Weidner, Committee Member

Lacy Ford, Vice Provost and Dean of Graduate Studies

ACKNOWLEDGMENTS

This degree would not have been possible without the influence of Dr. John W. Van Zee and Dr. Sirivatch Shimpalee. They both created an environment conducive to learning through his belief in my abilities, words of encouragement, and support. I am especially thankful to the rest of chemical engineering faulty for the educational support during my graduate studies.

I would like to acknowledge Department of Energy for their continued financial support through the Contract Grant DE-EE0000471.

My time at USC would not have been as entertaining had it not been for my friends those, who have been with me since my first days at USC. They continued to support me inspire of myself. Also, I would like to thank my colleagues, Tong Cui and Hyun Seok Cho. Finally, I would like to thank my family for the love and encouragement over the last five years.

ABSTRACT

An analysis of liquid water transport and removal in Proton Exchange Membrane Fuel Cells (PEMFCs) as affected by different membranes and the geometry and surface roughness of bipolar plates on is presented. Four topics are considered. First, the channel dimension and shape of various flow fields have been shown to affect the cell performance and the uniformity in the distributions of current. Typical variations in the channel width, height, and undercut that may occur with manufactured metal plates are studied. These sample-to-sample variations and distributions are studied and compared with laboratory-scale graphite plates. The goal of the work is to provide fundamental information that can be used to develop tolerance and design principles for manufacturing metal bipolar plates.

Secondly, the effect of roughness was studied experimentally to characterize liquid water droplet movement that may result from significant liquid droplet accumulation on the surface of the flow channel on either side of the membrane. Liquid water droplet movements were analyzed by considering the change of the contact angle as a function of flow velocity. Also, various stainless steel surfaces having different surface roughness were used to determine the relationships between flow rate and the contact angles. The pressures drop and channel characteristics are presented through dimensionless analysis and with a force balance equation. The result shows that the surface roughness has a great impact on pressure drop and liquid droplet removal. A unique relationship between surface roughness and onset of droplet movement has been

discovered that may describe the relationship between surface properties and liquid droplet movement on any surface in the PEMFC.

For the third aspect, a flexible low-cost technique for determining the current distribution was developed and used to understand the transport of water across a PEMFC for various membrane and cell geometries. This aspect built on the knowledge that non-uniform current distributions in PEMFCs result in local over-heating, accelerated ageing, and lower power output than expected. Liquid water transport is also known to qualitatively correlate with these distributions, especially when a fuel cell experiences water flooding. Present-day methods to measure these current distributions may significantly affect the flow path, break up diffusion media, and are usually very expensive. In this dissertation, a cost-effective method of mapping the current distribution in a cell was developed which overcomes many of the above limitations. A current distribution board was designed to add minimal internal resistance as well as minimize the disruption of the flow pattern when used in a cell.

These current distribution boards were used to study the forth aspect of this dissertation: the quantitative correlations between ex-situ measurements of water diffusion coefficients and electro-osmotic drag for different membrane materials, in-situ measurements of water transport, and numerical predictions of the current and water distributions as verified by water balances. The ex-situ measurements were shown to provide the parameters for the 3-D PEMFC mathematical model. The improved knowledge of this model proves to provide a better understanding the water management of the cell.

In addition, different membrane materials were used to study the effect of water transport properties on overall fuel cell performance. In this aspect, the alternative material (hydrocarbon type membrane) was studied and compared with standard membrane material (perfluorinated sulfonated copolymer, Nafion®). Current distribution behaviors of two different membranes were studied in the different operating condition of fuel cell such as humidity of inlet gas to understand the effect of water transport properties from different membrane material. Water balances experiment was also used to analyze water transport for these membranes.

Table of Contents

List of Table

List of Figure

CHAPTER 1

INTRODUCTION

1.1 Proton exchange membrane fuel cells

Fuel cells have been emerging as an alternative power source that are environmentally friendly and are more efficient than many generators and engines. The main advantage of using fuel cells as power sources is that it converts the chemical energy in the fuel directly to electrical energy. This direct conversion of energy allows for higher possible system efficiencies than engines. As the number of power generators using fossil fuel energy increases in all applications, the necessity for alternatives to the internal-combustion engine become even more obvious. Automakers and industrial developers are investigating many ways to significantly reduce emissions and for stationary and transportation applications, Proton exchange membrane fuel cells (PEMFCs) are now widely seen as a possibility. PEMFCs use hydrogen and airs as fuel and operate systems are becoming competitive with conventional technologies. Engineers have designed PEMFC systems for home power, automotive, air plane, Uninterruptible Power Supply (UPS) applications and much more. The main problems hindering wider adoption of PEMFC technology are fuel supply chain issues, high component cost, and short system lifetime.

In 1959, Grubb introduced an idea of using the thin membrane as a solid electrolyte in electrochemical cell. At present the PEMFC is one of the most capable

candidate system of fuel cell in term of application and operation. As shown in Figure 1.1, a PEMFC consists of two electrodes and a proton exchange membrane which acting as an electrolyte or proton conductor. The electrochemical reactions that arise at both electrodes are follows:

Anode : $$H_2 \rightarrow 2H^+ + 2e^- \quad (1.1)$$

Cathode : $$\frac{1}{2}O_2 + 2H^+ + 2e^- \rightarrow H_2O \quad (1.2)$$

Overall : $$H_2 + \frac{1}{2}O_2 \rightarrow H_2 + Enegry + Heat \quad (1.3)$$

The proton exchange membrane conducts protons from anode to cathode while insulates electrons flow between the electrodes and forces the electron to travel through an external circuit. This flow of electrons can be used as electrical energy.

1.2 Bipolar plate material

Inexpensive components, materials and manufacturing processes are necessary for successful implementation of PEM fuel cells into the commercial energy sector. The bipolar plate is one component that contributes significantly to the total PEM fuel cell manufacturing cost [1-3]. Figure 1.2 shows the PEMFC component cost for low and high production volume [4]. For high production system, the bipolar plate is one of dominate cost for PEMFC system. The most commonly used materials for bipolar plates in laboratory scale research are graphite. This material shows adequate electrical conductivity, light weight, and good corrosion resistance, therefore, producing precise flow-field channels in the graphite is difficult and expensive. On the other hand, there are mechanical issues, such as brittleness of thin graphite within the stack, that have led to

the exploration of different bipolar plate materials. Metallic bipolar plates are an attractive alternative to graphite, providing the necessary electrical and thermal conductivity while offering good mechanical strength to support the forces within the stack even at a reduced plate thickness. Stainless steel, which is relatively inexpensive, sufficiently conductive, corrosion resistant, and offers high strength, has shown satisfactory performance as a bipolar plate for several thousand hours of testing [5]. In the development of stamped, hydro-formed, or etched metal plates, one might expect variations in channel depth and undercut of any mask or pattern [6-11]. In addition, machining tolerances and tool wear may cause a variance in laboratory plates obtained from various suppliers.

1.3 Water transport in PEMFCs

Liquid water transport, accumulation and removal are the major problem in maintaining high performance in PEMFCs operation [12, 13]. The existence of liquid droplet has strongly effect cell performance [14], these water droplets create significant pressure gradient in flow channel [15]. According to complexity of small scales and porous media, it is difficult to fully understand water transport mechanism. Although water is essential in PEMFCs because the electrolyte membrane needs to be fully hydrated to ensure proton conductivity, excess liquid water may prevent the transport substrate to site catalyst, a phenomenon commonly known as "flooding". Therefore, understanding liquid water transport to achieve optimum water management is significantly important [16]. Various mathematical models and computational fluid dynamic (CFD) models have recently been presented in literature. However, the motion mechanism of liquid water is still not clear.

Bikerman studied water droplet on different surface roughness of stainless steels that have the contact angle round 90˚ and proposed that the surface roughness provides resistance for water droplet movement[17]

1.4 Current distribution devices

There has been much interest and develop methods to accurately measure the current distribution in an operating fuel cell. It is considered that durability and cost are the major hurdles for the large-scale application of PEM devices. Therefore, preventing membrane degradation will lead the way to a desirable lifetime of PEM fuel cells. Non-uniform current distribution in polymer electrolyte membrane fuel cells results in local over-heating, accelerated ageing, and lower power output than expected. This issue is very critical when fuel cell experiences water flooding [18].

Understanding of current distributions when fuel cell operated along with the variation of gas composition in the cell is critical for studying the fuel cell [19]. In an attempt to understand the current distributions, the numerical simulation mostly is used [20]. However, experimental data is required to validate the numerical result and also to have better understanding of current distribution and its effect. The measurement results from the current distribution can then be used to observe possible water transport in the cell. Currently, many methods for current distribution significantly affect flow path and break up diffusion media and are usually very expensive. A cost-effective method of mapping the current distribution in a cell was developed without disrupting flow

1.5 Proton exchange membrane

The proton exchange membranes are usually base on the polymer backbone attached with negatively charged groups. An improved Nafion® membrane manufactured by Dupont generally used as the benchmark membrane for proton exchange membrane fuel cells. A perfluorinated sulfonated copolymer, Nafion®, exhibits good thermal and chemical stability. Also Nafion® shows high proton conductivity under hydrated state but dramatically decrease with temperature above 90˚C because of the loss of absorbed water in the membrane.

The limitations to commercial use is poor conductivity at low humidity and elevated temperature, chemical degradation at elevated temperatures and the most importantly membrane cost. The challenge is to produce a cheaper material for PEMFC membrane that can satisfy the thermal and chemical stability, and high conductivity. Presently, one of the most promising candidates is the use of hydrocarbon polymer for polymer backbones.

1.6 Modeling for PEMFC

The number of PEMFC related models has increased intensely in the past few years [21]. Not only are there more models being published, but they are also increasing in complexity and scope. Due to the increased computational power these day, more detailed and complex simulation are possible. Full, 3-D fuel-cell models and the treatment of such complex phenomena including materials, transport, electrochemistry, and catalysis are becoming more common. Because of the mixture and complexity of electrochemical and transport phenomena involved in a fuel cell and occurring at

different length and time scales, fuel cell modeling and simulation requires a methodical framework parallel to computational fluid dynamics (CFD) [22]. CFD models which based on finite-element framework can solve complex equation such as the Navier-Stokes equation in multiple dimensions. CFD models are usually offered through commercial packages, some of which include an electrochemistry module.

1.7 Objectives of the study

This dissertation is focused on analysis of the bipolar plate material, flow field configurations and channel dimension and shape. These changing flow field configuration and channel characteristic have been shown to affect the cell performance and uniformity in distributions of current. In another chapter, typical variations in the channel width, height, and undercut that may occur with manufactured metal plates are studied. These sample-to-sample variations and distributions that may occur are studied and compared with laboratory-scale graphite plates. The objective of the study is to provide fundamental information that can be used to develop tolerance and design principles for manufacturing metal bipolar plates.

In addition, an analysis of liquid water (e.g. droplet) movement as affected by bipolar plate roughness and perhaps nano structure. An analysis of the influence of bipolar plates on liquid water transport and removal in PEMFCs is presented. Both experiments and modeling are used to characterize liquid water movement. In a PEMFC, the liquid transports from the cathode generating site through the gas diffusion layer (GDL) and then into the flow channel of the bipolar plate. Liquid water may also diffuse from the cathode to the anode, move through the anode GDL and then flow into to the

anode flow channel of the bipolar plates. There can be significant liquid droplet accumulation on the surface of the flow channel on either side of the membrane. Here, liquid water droplet movements were analyzed by considering the change of the contact angle by flow velocity. Also, various stainless steel surfaces having different surface roughness were used to determine the relationships between flow rate and the contact angles. The pressures drop and channel characteristics are presented through Volume of Fluid (VOF) computations and analyzed with a force balance equation. The goal is to describe the relationship between Reynolds number and contact angle on any surface in the PEMFC.

It is well known that non-uniform current distributions in PEMFCs result in local over-heating, accelerated ageing, and lower power output than expected. Liquid water transport is also known to qualitatively correlate with these distributions, especially when a fuel cell experiences water flooding. Present-day, methods to measure these current distributions may significantly affect the flow path, break up diffusion media, and are usually very expensive. In this dissertation, a cost-effective method of mapping the current distribution in a cell was developed, which overcomes many of above limitations. Furthermore, a current distribution board was designed to add minimal internal resistance as well as minimize the disruption of the flow pattern when used in a cell. The printed board circuit designed consists of a Kapton® base layer, copper deposit, nickel deposit, and gold flash to prevent oxidation. The current distribution board consists of 10 individual current collecting areas that match the flow field and that are separated by thin sections of Kapton® from the base layer. Adaptors are attached to both sides of the board, which collect the current thru Hall-effect sensors. The Hall-effect sensors output

an analog signal that is proportional to the amount of current detected. Additionally, a mathematical model is being developed based on experimental results. This model will help determine the fuel cell's performance based on different testing conditions and ultimately be used as a tool for understand water management of the cell.

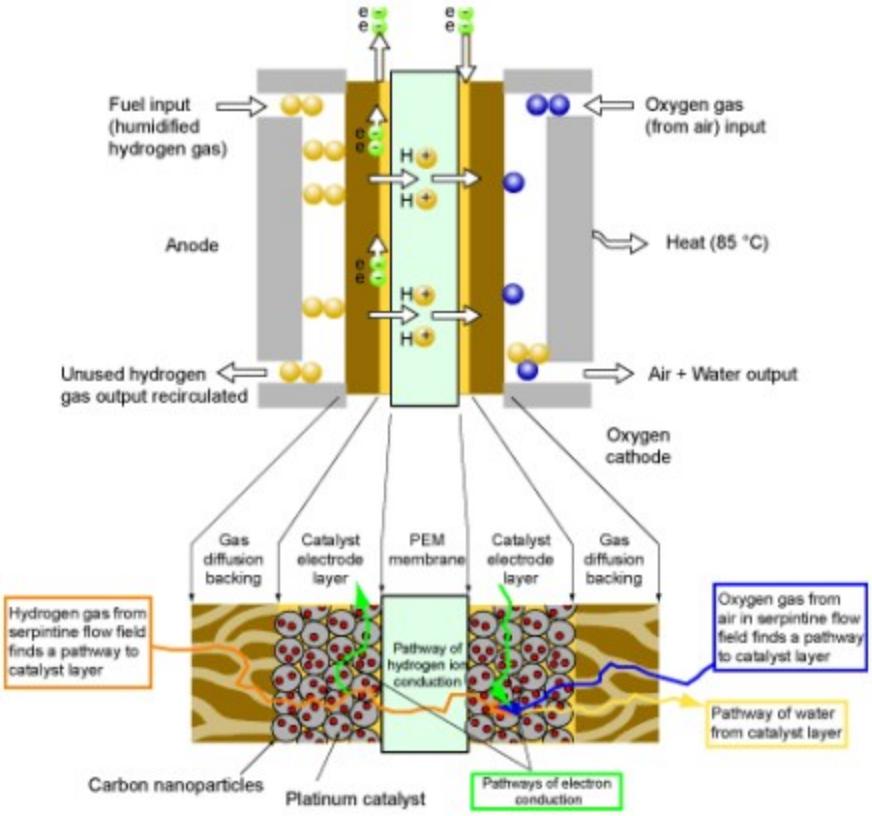

Figure 1.1. Schematic of PEMFC operation[23].

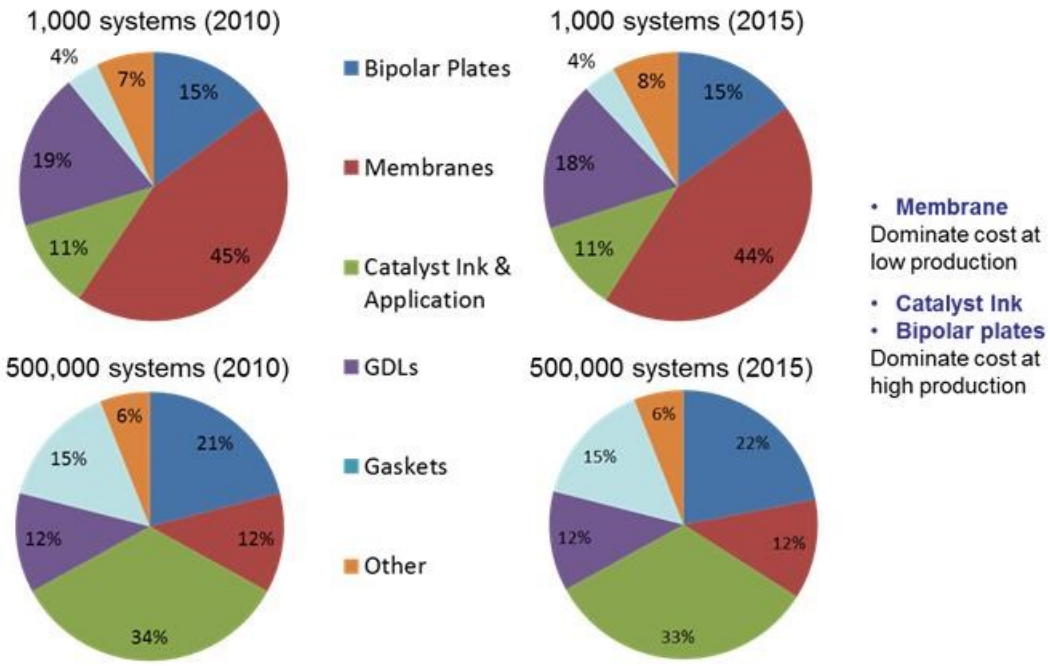

Figure 1.2. PEMFC component cost for low and high volume production [4].

CHAPTER 2

LITERATURE REVIEW

2.1 Bipolar plate materials

Materials selection for a commercial product that involved in design and manufacturing process eventually becomes specific to the particular product and application [24]. Bipolar plate is one of the most important parts in PEMFC which account for 40% of fuel cell stack cost and about 80% of the total weight [25-27].

Bipolar plate have performed various function such as distribute the fuel and oxidant into the cell, mechanical support for the cell, carry current from the cell, remove water away from cell, and also keep the cell cool [28]. Materials have been on the basic of mechanical strength, thermal and electrical conductivity, corrosion resistance, and most importantly cost. Development of new materials for the bipolar plate is the key to reducing the cost, volume, and weight of fuel cell stacks [29].

2.1.1 Graphite

Bipolar plates have conventionally been made from graphite. It has shown that graphite has the chemical stability and mechanical strength as well as thermal and electrical conductivity for high performance PEMFC [30]. However, pure graphite is relatively costly material and requires expensive machining. Since graphite is brittle and relatively porous, thick bipolar plate must be used. These are reducing the specific volumetric and gravimetric power density of the stack [31].

2.1.2 Metallic

The metallic plates are considered as alternative materials for PEMFC bipolar plate. In Table 2.1, there are comparisons between the properties of metals commonly used for bipolar plate production [32]. They have high electrical conductivity, low porosity, and are generally less expensive than graphite from both a material and processing perspective [33, 34]. Since, the gas permeability is so low, metallic plates can be made much thinner than porous material such as graphite [29]. For these reasons, the uses of metallic plate potentially increase the volumetric power density and gravimetric power density of PEMFCs. The most advantage of metallic plates is relatively cheap and ease of manufacture but they tend to corrode in the fuel cell environment [35, 36]. The limiting factor of metallic material is corrosion resistance and contact resistance, thus the bulk resistance of metal is very low [34].

A typical stainless steel is one of the most promising candidates for PEMFCs bipolar plate. The stainless steel might meet all the necessary requirements in fuel cell stacks such as conductivity, strength and ease of machining when compared with other metal plates [37]. Stainless steel alloys are a common, low-cost metal that could be fabricated into bipolar plates in large quantities by continuous rolling or by stamping into thin layers of sheets. However, the significant drawback with the metal bipolar plates is corrosion resistance [35, 38]. When corrosion arises from chemically reactive, the metal plate will form oxide layers at the surface. These oxide layers are electrically insulating which leading to high contact resistance resulting of a voltage drop in the fuel cell. To overcome the corrosion problem of metallic bipolar plates, various coating and surface treatments have been proposed [34]. The combination of the metallic bipolar plate and

coating makes it more difficult to meet the cost requirement. The major challenge in effectively using stainless steel in the production of a bipolar plate is the reduction, control of the oxide layer and the development of low cost coatings to prevent ion leaching which contaminates the PEMFC [32].

2.1.3 Composite plates

Composite plate can be as metal, polymer or carbon based material[33]. Composite materials have been developed for PEMFC bipolar plates to improve their corrosion resistance and contact resistance. Fu et al. [39] reported that using electrodeposited an Ag-polytetrafluoroethylene composite layer on 316L stainless steel bipolar plates exhibited lower interfacial contact resistance, higher corrosion resistance, and better hydrophobic characteristics. Carbon-carbon composites (a carbon matrix reinforced with carbon fibers [40]) are now being developed and applied to PEMFC bipolar plate. Carbon-carbon composites provide the strength, low density, chemical stability, high electrical and thermal conductivity, and the ability to operate at temperatures [41]. But the major disadvantage of carbon-carbon composites is take longer processing time with the high-temperature process which is potentially expensive. Carbon-polymer composites are made by incorporating carbonaceous material into a polymer. This material offer excellent corrosion resistance and can be formed by injection or compression molding. These plates are low cost, light weight, and easy processing. The drawback of carbon-polymer composites is low electrical conductivity [42].

2.2 Metallic bipolar plate fabrication

There has been significant study in manufacturing bipolar plates using vary of different processes. The aim is to develop a manufacturing process that is cost effective and efficient in order to make a metallic plate a viable candidate for commercial production [27]. Commonly used manufacturing processes include compression molding, stamping, and etching.

2.3 Flooding and Water Management

One of the most important issues of PEMFC influenced by flow field design is water management [43]. This is a critical for PEMFCs development [44, 45], because liquid water can accumulate and flood the gas flow channel blocking delivery fuel and oxidant into micro-channels and the porous electrodes; thus causing a drop in PEMFC performance [45]. The cell performance depends on factors operating conditions, transport phenomena in the cells, and flow channel design [46, 47].

Flooding has a significant undesirable effect on PEMFC performance, because when a large amount of liquid water accumulates in the porous layer's pores and flow channel, the oxygen and hydrogen transport resistance increases which reduce the oxygen and hydrogen flow rate into the cell. However, humidification for the PEMFC also importance as dehydration of the membrane results in lower proton conductivity and risks the membrane degradation [48]. Thus, water management has been a major consideration in PEMFC flow channel design. Water distribution in the membrane of PEMFCs is determined mainly by the mechanisms of electro-osmotic drag, back diffusion and also water generation in the cell. In practice, there is much more water causing flooding in the

cathode than in the anode, especially at high current density because of the domination of electro-osmotic drag water from anode to cathode and the water generation at cathode reaction [49].

This makes the cathode flow field design a key factor for enhancing reactant and product transport and for removing liquid water. Researchers have studied the onset and effects of flooding in PEMFCs, and have investigated methods of mitigating this occurrence, such as flow field design modification.

2.4 Current distribution devices

There has been much interest and develop methods to accurately measure the current distribution in an operating fuel cell. It is considered that durability and cost are the major hurdles for the large-scale application of PEM devices, therefore preventing membrane degradation will lead the way to a desirable lifetime of PEM fuel cells. Non-uniform current distribution in polymer electrolyte membrane fuel cells results in local over-heating, accelerated ageing, and lower power output than expected. This issue is very critical when fuel cell experiences water flooding [18].

Understanding of current distributions when fuel cell is operated along with the variation of gas composition in the cell of PEMFC is critical for studying the fuel cell [19]. In an attempt to understand the current distributions, the numerical simulation mostly is used [20]. However, experimental data is required to validate the numerical result and also to have better understanding of current distribution and its effect. The measurement results from the current distribution can then be used to observe possible water transport in the cell.

There are several methods of measuring current distribution in PEMFC have been reported, these include segmenting the electrode either by the machining of insulated electrode blocks [19, 50-52] or using a printed circuit board technology [53, 54]. Weiser *et al*. described a technique that developing a magnetic loop array embedded in the current collector plate to measure two-dimensional current distribution in PEMFC [55]. Zhang *et al*. used partially segmented anode GDL and current distribution measurement gasket on anode flow field to measure local current [56]. Alaefour *et al*. investigated the impact of flow channel orientation on fuel cell performance by using segmented cell system [54, 57]. Reshetenko *et al*. studied impact of serpentine flow field parameter, using segmented cell and also demonstrated the capability of segmented cell in resolved cyclic voltammetry [58]. Several authors used mathematically model of water, temperature, and current distribution in PEMFCs [59-63]. These efforts included modeling of the water, temperature, and current distribution profiles across the membrane [64]. Models have shown that local current distribution is depended upon local water and temperature profiles [59, 65]. Gerteisen *et al*. used segmented cell to investigate effect of cell voltage, relative humidity, and flow configuration and to acquire the parameter for PEMFC modeling [66]. Nguyen *et al*. studied the effectiveness of three difference anode humidification. The authors showed that insufficient back diffusion of water from the cathode to the anode cause poor current distribution[62]. Carnes *et al*. compare computational PEMFC data with experimental data collected by segmented current collector under various conditions [63]. However, those methods of current distributions may significantly affect the flow path, break up diffusion media, and are usually very expensive. Therefore in this work, a cost-effective method of mapping the current

distribution in a cell was developed that will overcomes many of above limitations. This work aims to use the innovative measurement system [27] for the mapping of current distribution in the PEMFC as well as understanding of water transport when fuel cell is operated.

Currently, many methods for current distribution significantly affect flow path and break up diffusion media and are usually very expensive. A cost-effective method of mapping the current distribution in a cell was developed without disrupting flow

2.5 Model development

One of the first PEMFC models was develop by Springer et al [59]. This model is isothermal and considers water transport mechanism. The model used data that including water content and water diffusion coefficient, proton conductivity, and electro-osmotic water drag as a function of membrane water content. The model result showed the important of water manage for PEMFC[59]. Springer et al [65] added a detail of cathode to the original model. This model considered the cathode catalyst layer and GDL. They studied the effect of the GDL porosity in the operating cell.

Bernardi and Verbrugge [67] published the fuel cell model based on gas diffusion electrode model [68]. Their model also highlight the importance of water management. This model is 1-D isothermal and includes transport of both gas and liquid in the diffusion media. The limitations of this model is the assumed to be fully hydrated of membrane and the neglect of true two-phase flow; the model only uses constant volume fraction.

Almost all of the fuel cell models are based on Springer and Bernardi and Verbrugge model. Several researchers were influenced by Springer work. One of the most renowned researchers to follow Springer model is Nguyen and White [62]. Their model examined 2-D effect along the gas flow channel. Although the 2-D model has very similar basic to the Springer model, it is nonisothermal and considers the liquid-water flow. The model exhibited that water and heat management are very important for optimal PEMFC operation.

Shimpalee and Dutta [69] established one of the first fuel cell model with 3-D CFD based on Springer model. Later model by Shimpalee and Dutta [70-75] also examined mass transfer and complete 3-D effect.

Table 2.1. Properties for common metals compared with graphite used to make bipolar plates [32].

	Titanium	**Aluminum**	**Stainless steel**	**Graphite**
Bulk conductivity, S cm^{-1}	1500	376000	10000	110-680
Corrosion prone	Yes	Yes	Yes	Low
Density, g cm-3	4.54	2.7	8.0	1.8-2.0
Thermal conductivity, W m^{-1} K^{-1}	17.2	205	16.3	N/A
Thickness, mm	1-2	1-2	1-2	5-6
Permeability	Negligible	Negligible	Negligible	Low
Cost, $/lb	4.5	2	0.15	0.5-1.0

CHAPTER 3

UNDERSTANDING THE EFFECT OF CHANNEL TOLERANCES ON PERFORMANCE OF PEMFCS

Distributions in the concentration of reactant species in a PEMFC can cause distributions in local current density, temperature, and water content over the area of a PEMFC. These distributions can lead to effects such as flooding and MEA dehydration thus causing stresses in different regions of the fuel cell. Changing flow-field configurations and channel characteristics have been shown to also affect the cell performance and uniformity in distributions. This work investigates how performance and distributions in a baseline laboratory cell prepared by a precise machining method compared with others from alternative manufacturing processes (e.g., stamping, electrochemical etching, hydroforming, etc.). Specifically we examine "typical" variations in the channel width, height, and undercut that may occur with alternatively manufactured metal plates and compare those with sample-to-sample variations that may occur with between laboratory-scale graphite plates. This work will provide fundamental information that can be used to develop tolerance and design principles for manufacturing PEMFC bipolar plates.

3.1 Introduction

As the number of power generators using fossil fuel energy increases in all applications, the necessity for alternatives to the internal-combustion engine become even more obvious. Automakers and industrial developers are investigating many ways to significantly reduce emissions and for stationary and transportation applications, PEMFCs are now widely seen as a possibility.

Inexpensive components, materials and manufacturing processes are necessary for successful implementation of PEM fuel cells into the commercial energy sector. The bipolar plate is one component that contributes significantly to the total PEM fuel cell manufacturing cost[1]. While graphite has been widely used in laboratory scale research due to adequate electrical conductivity, light weight, and good corrosion resistance, to produce precise flow-field channels into the graphite is difficult and expensive. In addition, there are mechanical issues, such as brittleness of the thin graphite within the stack, that have lead to the exploration of different bipolar plate materials. Metallic bipolar plates are an attractive alternative to graphite, providing the necessary electrical and thermal conductivity while offering good mechanical strength to support the forces within the stack even at reduced plate thickness. Stainless steel, which is relatively inexpensive, sufficiently conductive, corrosion resistant, and offers high strength, has shown satisfactory performance as a bipolar plate for several thousand hours of testing[5]. Figure 3.1 shows samples of bipolar plates manufactured by different technologies.

In the development of stamped, hydro-formed, or etched metal plates, one might expect variations in channel depth and undercut of any mask or pattern[6-11]. In addition,

machining tolerances and tool wear may cause there to be a variance of laboratory plates 4 obtained from various suppliers. This work will provide numerical studies in an attempt to develop tolerance and design principles for manufacturing PEMFC bipolar plates. Specifically we will examine "typical" variations in the channel undercut or so-called draft angle or etch factor[6], bending angle, and channel depth profile that may occur with alternatively manufactured metal plates as shown in Figure 3.2. Clearly, companies with these processes have an understanding of their own tolerances, how to change them, and the economics associated with these changes, but the purpose of this work is to help answer the question of "how much do these variations affect performance and the reported data."

3.2 Model development

A computational continuum mechanics (CCM) technique based on a commercial flow solver, STAR-CD 4.14, was used to solve the coupled governing equations[76]. This software has an add-on tool called expert system of PEMFC (es-pemfc) version 2.50 that incorporates the requirement of the source terms for species transport equations, two-phase equations for water, and heat generation equations created by electrical losses[77]. The subroutines with the inclusion of solubility effect and electron transport were included to calculate the electrochemical and permeability for this simulation[64, 71, 72, 78]. Note that this model has been validated with experimental data and the results were satisfied in both polarization data[71] and water balance data[64].

The numerical simulation in this work consisted of three tasks. The first task was focused on the effect of draft angle or etch factor at the channel cross section on the

PEMFC performance and local distributions. From Figure 3.2, the draft angle (θ) is typically calculated as:

$$\theta = 90 - \tan\text{-}1(\text{depth/undercut}) \quad (3.1)$$

And Etch factor is calculated as:

$$\text{Etch factor} = \text{depth/undercut} \quad (3.2)$$

Several studies found in literature were aimed at understanding the impact of channel cross section area, channel width/height ratio, and/or the ratio between channel width and rib width on PEMFC performance[73, 79-82], but none of them has been referred to the design off-set from manufacturing process. In this task, four draft angles were selected based on bipolar plate manufacturing reports[6, 7] as shown in Figure 3.3. It is noted that the draft angle of zero or etch factor of infinity is a typical cross section shape from the laboratory graphite plate made using a machining process[83] and also most commonly used in the geometry for numerical simulations[64, 72, 73, 78]. The fuel cell geometry used in this task consisted of a 2.54 cm2 reacting area with a two pass serpentine flow-field. It is not necessary to use the complete full-scale PEMFC geometry (e.g., 25 cm2, 50 cm2, etc.) in this task because the shape of the channel cross section was not changed along the serpentine length and the cathode and anode gas stoichiometries were constant. Therefore using smaller size, as shown in Figure 3.3, was enough to report the difference in performance and distributions.

For the second task, the impact of the channel bending radius at the turning locations on PEMFC performance and pressure drop was studied. Four different radii were used in this task as shown in Figure 3.4. Note that the first picture in Figure 3.4 is a standard bending radius (i.e., sharp turning), which was used as baseline results. Similar

to the first task, the small size geometry was used in this analysis. Four different bending designs were selected as shown in Figure 3.4. They are sharp turning (baseline), 0.3 mm, 0.6mm, and 1.0 mm in radius. These selected angles at the channel bending location should cover all off-set from the manufacturing processes.

The last task in this work focused on the intent to understand the effect of channel depth uniformity on PEMFC performance, pressure drop, and uniformity of distributions. For most manufacturing technologies, it is nearly impossible to obtain consistent channel dimensions for an entire flow-field on the bipolar plate. Figure 3.5 shows five axial average channel depth profiles on a 25-cm^2 PEMFC flow-field. The overall average channel depth was 0.4 mm. The profiles for plates # 2 and 3 were measured with a Mitutoyo SJ400 contact profilometer. Plate # 1 was a machined graphite plate, which is typically used in laboratories. Plates # 2 and 3 were stainless steel PEMFC flow-fields created by an electrochemical etching technology[6, 7]. Plates # 4 and 5 were designed for comparison with the first three plates. In this task, the model geometries needed to be the same size for each of the plates used for measurement. Therefore five PEMFC geometries were created using the channel depth profiles shown in Figure 3.5.

In general, the PEMFCs simulated in these three tasks consisted of two flow-field patterns (upper is anode and lower is cathode) separated by GDLs and a membrane electrode assembly (MEA). The properties and parameters used in the simulation are shown in Table 3.1. Operating conditions considered for these studies were 80°C/70°C dew point at 1.2/2.0 stoichiometry of 40% H2/Air anode/cathode with 101 kPa system pressure and 70°C cell temperature for stationary applications, and 75% RH 80°C/DRY

at 1.3/2.0 stoichiometry of neat H2/Air anode/cathode with 274 kPa system pressure and 80°C cell temperature that is usually applied for automotive applications.

There were a maximum of 1 million computational cells in geometries used in Task 3. Therefore, a parallel computing of STAR-CD, PRO-HPC was chosen by using multiple processors for these simulations. Consequently, each model had to be decomposed (i.e., one piece per processor) for computation. Each processor's solutions were communicated by InfiniBand over fast Ethernet connection. Again, in this work we considered the "typical" variations in the channel width, height, and undercut that may occur with alternatively manufactured metal plates and compare those with sample-tosample variations that may occur between laboratory-scale graphite plates. The results of electrochemical variables, temperature, and pressure drop with three aspects of channel off-set due to fabrication of bipolar plate were compared and are discussed further.

3.3 Results and discussion

3.3.1 The effect of draft angle or etch factor on PEMFC performance

Figure 3.6 shows polarization curves for the four different draft angles. Figure 4.6a presents the results for the stationary operating condition and Figure 3.6b reveals the results from automotive conditions. Both Figures 3.6a and 3.6b show similar tendencies for the polarization curves, though the cross section channel with a 33.7° draft angle or 1.5 etch factor shows the lowest performance while the standard cross section channel (draft angle ~ 0° or Etch factor ~ ∞) gives the highest performance. Note that there is not a significant difference in performance for the Standard, 11.3°, and 14.7° draft angles;

they are just slightly different from each other. It should also be pointed out that for the stationary condition, the performance drop starts at a current density greater than 0.6 A/cm^2, but for the automotive condition, the performance drop begins after the kinetic region (i.e, cell potential below 0.85 V and current density greater than 0.1 A/cm^2). This could be due to the change in channel area. That is by changing the ratio of channel width and rib width according to the difference of draft angles shows more impact to PEMFC performance under automotive conditions than stationary conditions. For further analysis, the additional plots of current density, membrane water content, and temperature are discussed.

Figure 3.7 shows current density distributions on MEA surface for the four different draft angles or etch factors at I_{avg} of 1.0 A/cm^2 under stationary conditions (Figure 3.7a) and automotive conditions (Figure 3.7b). For current density distributions under stationary conditions shown in Figure 3.7a, all distributions of local current density are decreasing from inlet toward outlet due to the consumption of the reacting gases. However, the standard channel gives the most uniformity in distribution compared to other draft angles. For standard channel with ~ 0˚ draft angles, the maximum current is 1.2 A/cm^2; for 11.3˚ draft angle, the maximum current is 1.3 A/cm^2; for 14.7˚ draft angle, the maximum current is 1.37 A/cm^2; for 33.7˚ draft angle, the maximum current is 1.48 A/cm2 and all four draft angles have similar minimum current of 0.72 A/cm2. Furthermore, by increasing the draft angle of the channel cross section, the uniformity of current density distribution under channel and side-by-side rib areas is reduced as also shown in Figure 3.7a.

For automotive operating condition shown in Figure 3.7b, all four draft angles also show similar distribution but they are totally different from the case of the stationary condition shown in Figure 3.7a. For overall distributions, the local current density is decreasing from inlet toward the first turning due to the water transport across the MEA rather than gas consumption. This condition is relatively dry compared to the stationary condition, where the membrane is well hydrated. Therefore, hydration of the MEA is a major factor of its performance. From the first turning toward the exit, water from reaction and electro-osmotic forces at the cathode side diffuses to the anode to hydrate the membrane and increases the proton conductivity, thus increasing the local current density. This phenomenon applies to all draft angles in this study. Moreover, in the dry condition encountered under automotive conditions the higher degree of draft angle gives more global uniformity in current density distribution. For the standard channel, the maximum current is 1.41 A/cm^2 and minimum is 0.88 A/cm^2; for 11.3˚ draft angle, the maximum current is 1.35 A/cm^2 and minimum is 0.88 A/cm2; for 14.7˚ draft angle, the maximum current is 1.3 A/cm^2 and minimum is 0.88 A/cm2; for 33.7˚ draft angle, the maximum current is 1.1 A/cm^2 and minimum is 0.91 A/cm2.

The proton conductivity condition of the MEA can be justified by water content inside the membrane. Figure 3.8 presents this information in the local distribution profiles and it confirms the PEMFC performance from Figure 3.7 that for both stationary (Figure 3.8a) and automotive (Figure 3.8b) conditions, the averaged membrane water content is decreasing when the draft angle is increased. Obviously in stationary conditions where the membrane is well humidified, the membrane water content value is much higher than in automotive conditions where the membrane is relatively dry. From Figure 3.8a, the

distributions of membrane water content show significantly lower and more nonuniformity when the draft angle increases. It is also shown that the local distribution under channel and side-by-side rib area is also more non-uniform as the draft angle increases. This distribution is consistent with the current density distributions shown in Figure 3.7a. Similarly to Figure 3.8b, the overall distribution agrees with those shown in Figure 3.7b where the value is decreasing around one-third of channel length from the inlet and then it begins increasing toward the outlet. The average value is lower when the draft angle is getting bigger but their differences of membrane water content value and non-uniformity in local distribution are not significant when compared to Figure 3.8a when the membrane is well humidified. The change in lambda value from standard shape to 33.7˚ draft angle is a 44% reduction for the stationary condition and 23% reduction for the automotive condition.

The major reason for the performance decrease, the membrane water content dropping, and other electrochemical variables changing when the draft angle is increased could be that the ability of heat transport inside fuel cell is reduced. Figure 3.9 shows the temperature distribution at cross section area where x = 15 mm at an average current density of 1.0 A/cm2 for the four different draft angles under stationary condition. For all contour plots, the highest temperature occurs at the cathode MEA/GDL interface and then it decreases toward top (anode) and bottom (cathode) of the cell. The membrane and GDL located under the channels display a higher temperature than those under the land areas. This is because the heat is easier to transport toward the land compared with the channel due to the higher thermal conductivity of the bipolar plate. Furthermore in this study, when the draft angle is getting bigger the land area is becoming smaller thus

restricting the heat transport from MEA toward the current collector. Therefore the temperature inside of the cell is increasing particularly at MEA and GDLs. The hydration of the membrane is reduced due to the higher temperature, thus dropping its water content and ability for proton transport. Note that this effect is applied to the case of automotive condition as well.

3.3.2 The effect of radius on channel bending areas on PEMFC performance

Figure 3.10 shows the polarization curves (a) and maximum pressure drop profiles as a function of current density (b) compared to four different radii of channel bending; standard, 0.3mm, 0.6mm, and 1.0mm, as shown in Figure 3.4. Figure 3.10a presents the numerical prediction of their polarization curves for both stationary and automotive conditions. For both conditions, all four cases of bending radii show similar performance. The standard case in which it has the sharp turning gives slightly higher performance than others at cell potential between 0.8V and 0.6V under stationary conditions. For automotive conditions, all polarization curves looks identical.

It might be anticipated that changing the radius value at the turning location of the fuel cell's serpentine flow-field could change flow behavior, such as pressure, inside fuel cell. However, the predictions reveal that these values do not impact the flow behavior inside the fuel cell as shown in Figure 3.10b. This Figure shows maximum pressure drop as a function of current density for both operating conditions. For both cases, the maximum pressure drop increases when the current density is raised due to the increase of inlet flow rate by maintaining constant stoichiometry. The pressure drop under automotive conditions is lower than stationary conditions because the anode and cathode flow rates for automotive conditions are lower than those values given in stationary

condition. This Figure shows that the effect of radius at turning location on maximum pressure drop is insignificant.

3.3.3 The effect of channel depth uniformity on PEMFC performance

As stated above that the fabrication of fuel cell flow channel can give several off-sets from the original design due to the limitation of each technology. These off-sets can impact fuel cell performance and physics inside the fuel cell for both global and local views. The uniformity of channel depth after fabrication is another factor that was studied this work as already shown in Figure 3.5.

Figure 3.11 shows the effect of non-uniformity of channel depth on (a) PEMFC performance and (b) maximum pressure drop. Five different channel depth uniformity profiles on 25-cm^2 PEMFC were selected in this study and reported for both stationary and automotive conditions. Again, Plate # 1 represents the perfect uniformity that can be found from machining technology; Plate # 2 provides the flow-field where the channels at the inlet area are shallower than channels at the outlet area; Plate # 3 shows the flowfield where channels at the inlet area are deeper than the channels at the outlet area; Plate # 3 presents the extreme case where the inlet channel is the deepest then the channels gradually get shallower toward the outlet; Plate # 4 shows another extreme case where the inlet channel is the shallowest then the channels are getting deeper toward the outlet. Note that all of the flow-fields have the same average channel depth of 0.4 mm.

Polarization curves for both the stationary and automotive conditions are shown in Figure 3.11a. The results show that there is no significant difference in overall performance from those flow-fields. However, the maximum pressure drop profiles from Figure 3.11b confirms that Plate # 1, where the channel depth is the most uniform, gives

the lowest pressure drop for both operating conditions. Further, the maximum pressure drop is shown at Plate # 4, which has the shallowest channel at the outlet or the deepest channel at the inlet. Finally, this figure also reveals that the shallower channels at the outlet result in a higher pressure drop than the deeper channels and this statement applies to both operating conditions. This is because the flow restriction due the change of channel size shows more impact on system pressure when it is located near the outlet than the inlet.

The current density distributions on MEA surface for the five flow-fields under stationary (a) and automotive (b) conditions are shown in Figure 3.12. Those current distributions have an averaged value of 1.0 A/cm2. For the stationary condition shown in Figure 3.12a, all five distributions shows similar profiles, where the highest current density is located near the inlet and the current density value decreases along the channel's pattern toward the outlet. The uniformity distributions of those five channel depth profiles are different but not significant. The maximum local current density value of 1.52 A/cm2 is shown at Plate # 1 but the lowest value of 0.41 A/cm2 is given at Plate # 5. From those distributions, it might be difficult to distinguish which plate has the most uniformity and non-uniformity in distribution. Therefore, a statistical technique is introduced to assist the analysis in this work. Figure 3.13a presents the area distribution of the current density profiles taken from Figure 3.12a for the stationary condition. These profiles represent the local current density value that is distributed on the largest MEA area. The X-axis is current density and the Y-axis is percentage of MEA surface area. For the distribution that has the most uniformity, the area distribution graph should show a small range of current density with high percentage of MEA surface area. This will make

the standard deviation for the data a low value. From Figure 3.12a and 3.13a, the most uniformity in distribution is Plate # 4 followed by Plate # 3 with standard deviation of 16 and 17, respectively. Note that both plates have shallow channel depth at the outlet. The most non-uniformity in current density distribution is presented at Plate # 1, which it has the most uniform in channel depth with the standard deviation of 0.21.

Similar reports and analysis from Figure 3.12a and 3.13a are shown in Figure 3.12b and 3.13b for the automotive condition. The current density distributions of five channel depth profiles for this condition are revealed to be more identical than the case of stationary condition even though their contour profiles look completely different. The overall contour profile from this operating condition has the local current density value decreasing from inlet toward one-third of MEA surface then increasing toward the outlet. The maximum current density value of 1.56 A/cm2 is presented at Plates # 2, 3, and 4.The lowest current density value of 0.8 A/cm2 is shown at all five plates. The area distribution of current density profiles shown in Figure 3.13b is completely different from Figure 3.13a. The profiles from Fig. 13b have a similar range of current density. The percentage of MEA surface area by current density of Plates # 2, 3, and 4 are higher than Plates # 1 and 5. For standard deviation, all five channel depth profiles have a very similar number, which are between 0.18 and 0.19. So it is concluded that the uniformity of current density for the automotive condition is the same for all five channel depth profiles.

3.4 Conclusions

The effect of draft angle or etch factor shows the most impact to PEMFC performance, heat transport, uniformity in distributions and pressure drop. For higher draft angle (lower etch factor), the gas channel will become bigger causing lower pressure drop in the flow channel. However, these giving lower performance because the rib space will be smaller which increase the heat conduction resistance.

The effect of radius at turning location (bending) on PEMFC performance is not significant for both stationary and automotive conditions compared to baseline flow-field (sharp turning).

The effect of channel depth non-uniformity shows the major impact on pressure drop and uniformity in distributions inside PEMFC. The more non-uniformity in channel depth from an average depth increase the flow resistance resulting higher pressure drop. The shallower channels at the outlet numerically give higher pressure drop than shallower channels at the inlet. For the stationary condition, shallower channels at the outlet seem to give more uniformity in distributions than shallower channels at the inlet and perfect channel depth uniformity. For automotive condition, the perfect channel depth uniformity has the most uniform distributions. The effect of channel depth non-uniformity on the overall steady state performance is minimal.

Table 3.1. Properties and parameters

Current Collector	
Thermal conductivity (W/m-K)	16.2
GDL	
Thickness after compressed (μm)	250
Permeability (m^2)	10^{-12}
Porosity after compressed (%)	70
Diffusion adjustment (%)	50
Thermal conductivity (W/m-K)	0.21
Membrane Electrode Assembly	
Thickness (μm) *(including 12.5 μm thickness of catalyst layer)*	50
Thermal conductivity (W/m-K)	0.15
Dry membrane density (g/cm^3)	2.0
Equivalent weight of dry membrane (g/mol)	1100
Cathode exchange current density (A/cm^2)	0.02
Cathode transfer coefficient	0.6
Anode exchange current density (A/cm^2)	0.2
Anode transfer coefficient	1.2

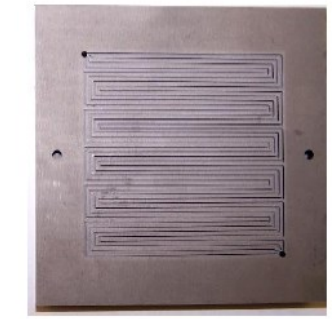

Machined graphite channel
Flow-field [Fuel Cell Technology, Inc.)

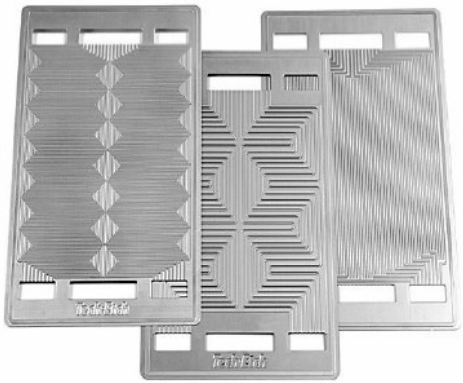

Photo etched SS and Ti *[Tech-etch, Inc.)*

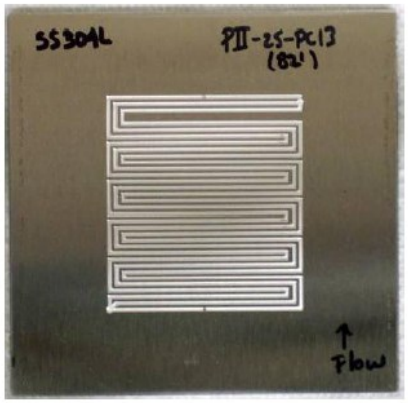

ElectroEtched SS *[Faraday Technology, Inc.)*

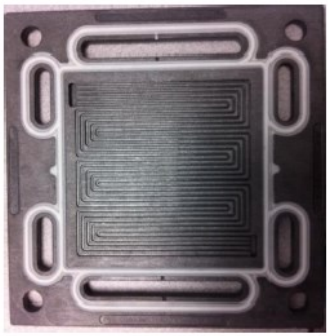

Compression molding plate
[BMC)

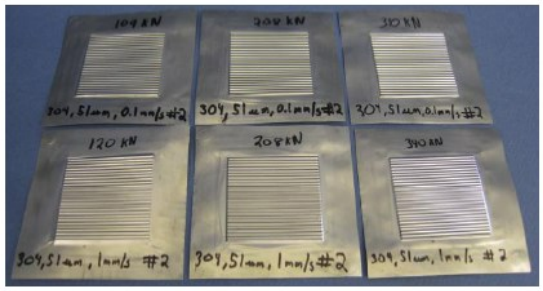

Stamped SS plates *[Virginia Commonwealth University (VCU))*

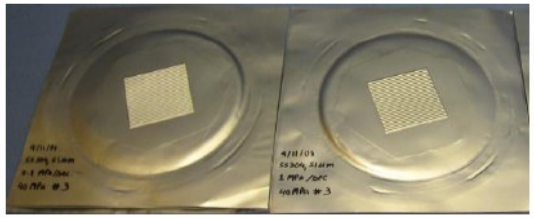

Hydroformed SS plates *[VCU)*

Figure 3.1. Fabrication technologies fo PEMFC's bipolar plate.

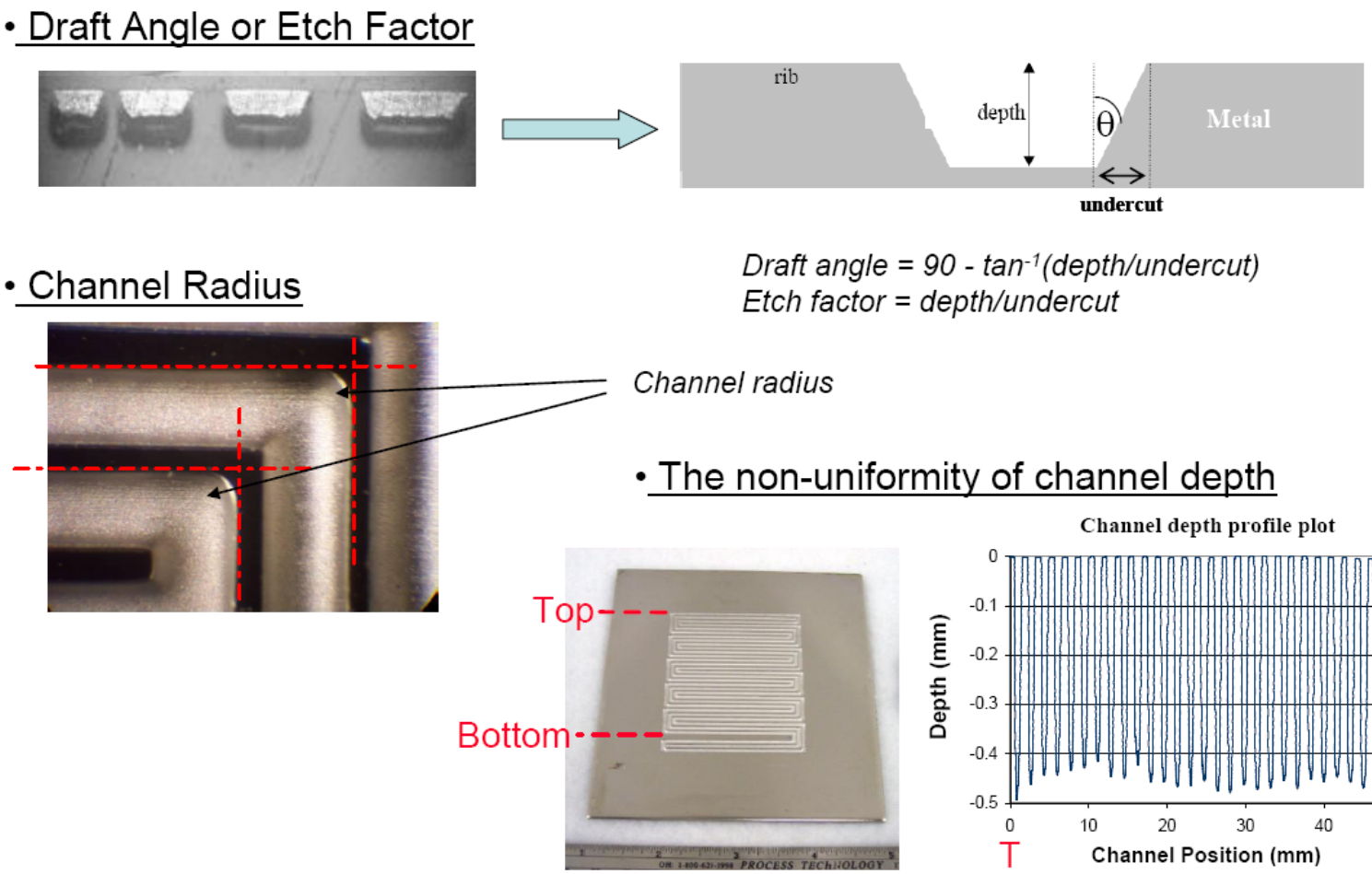

Figure 3.2. Typical channel off-set due to fabrication of bipolar plate

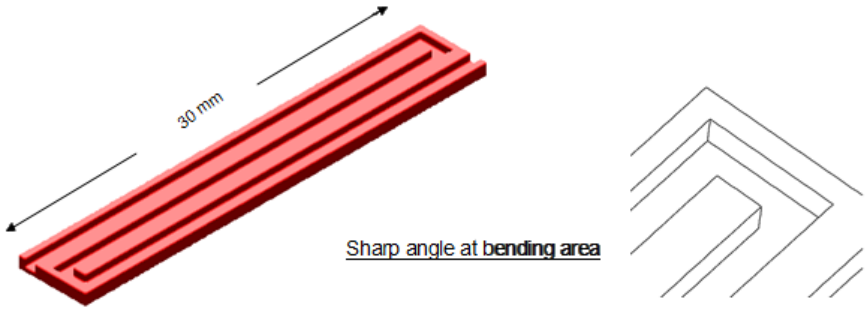

Cross section

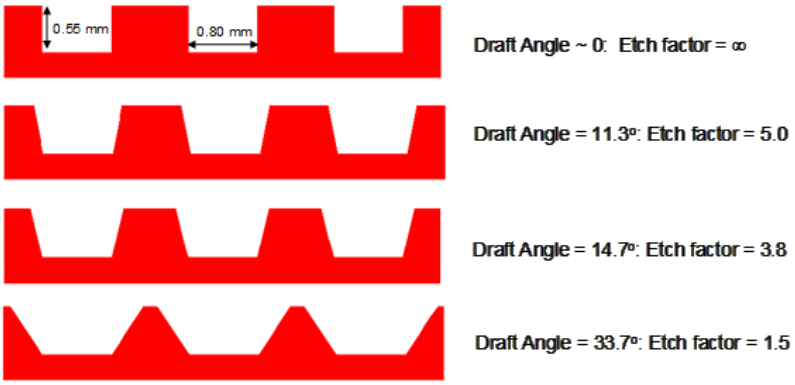

Figure 3.3. Geometries with four different draft angles used in this study. Note that the standard channel shape in this study is ~0 draft angle.

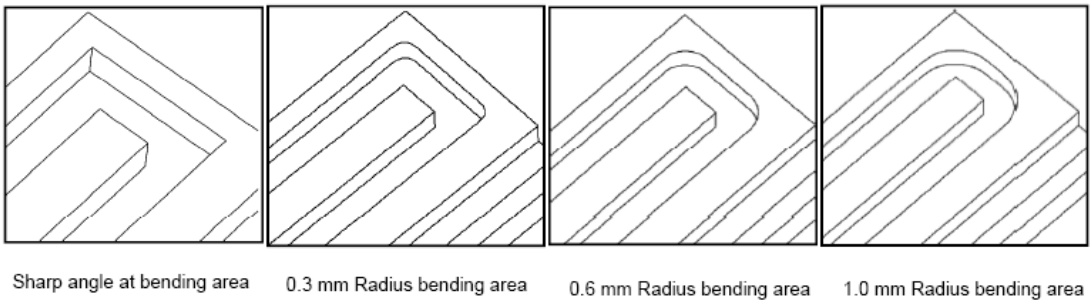

Figure 3.4. Geometries with four different radiuses at channel bending areas. Note that the standard bending radius in this study is the sharp turning.

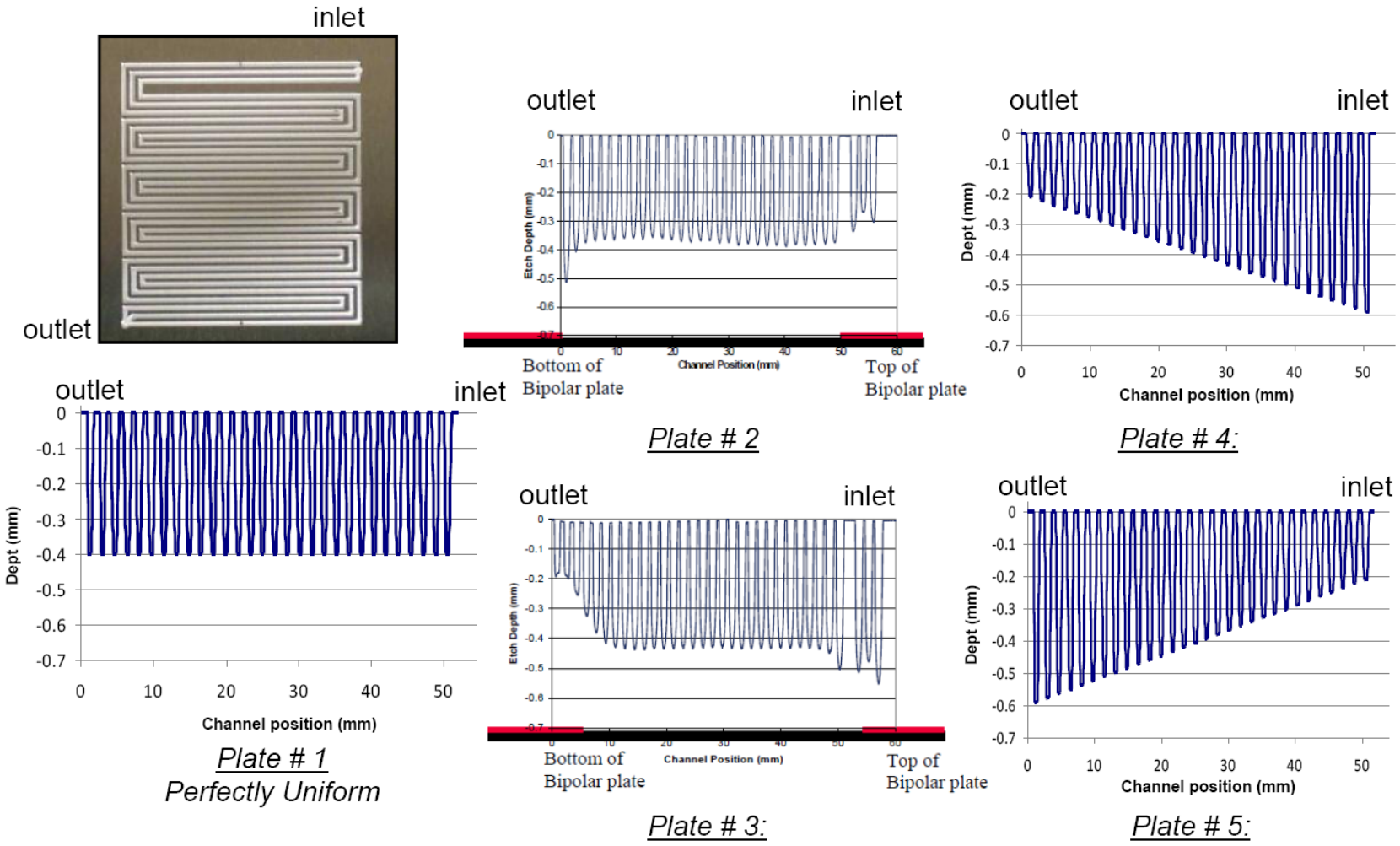

Figure 3.5. 25-cm^2 PEMFC flow-fields with five different channel depth profiles. The averaged channel depth of those five flow-fields is 0.4 mm. Note that the standard channel depth profile in this study is Plate # 1, perfectly uniform.

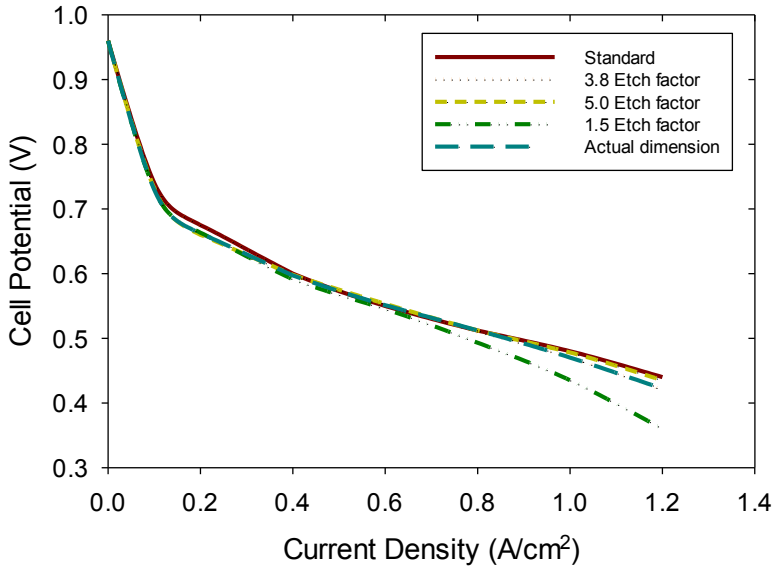

(a)

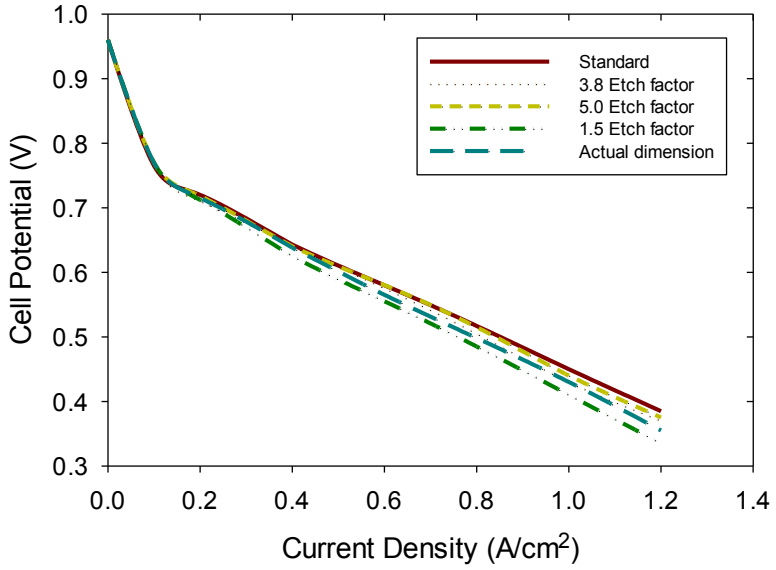

(b)

Figure 3.6. The effect of draft angle on PEMFC performance under (a) Stationary condition and (b) Automotive condition.

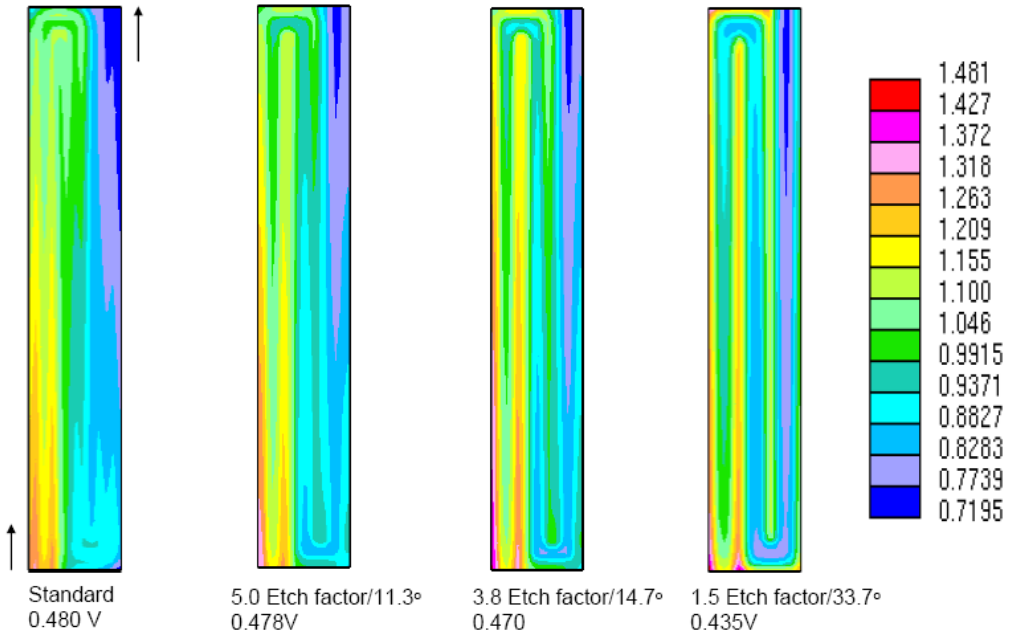

a)

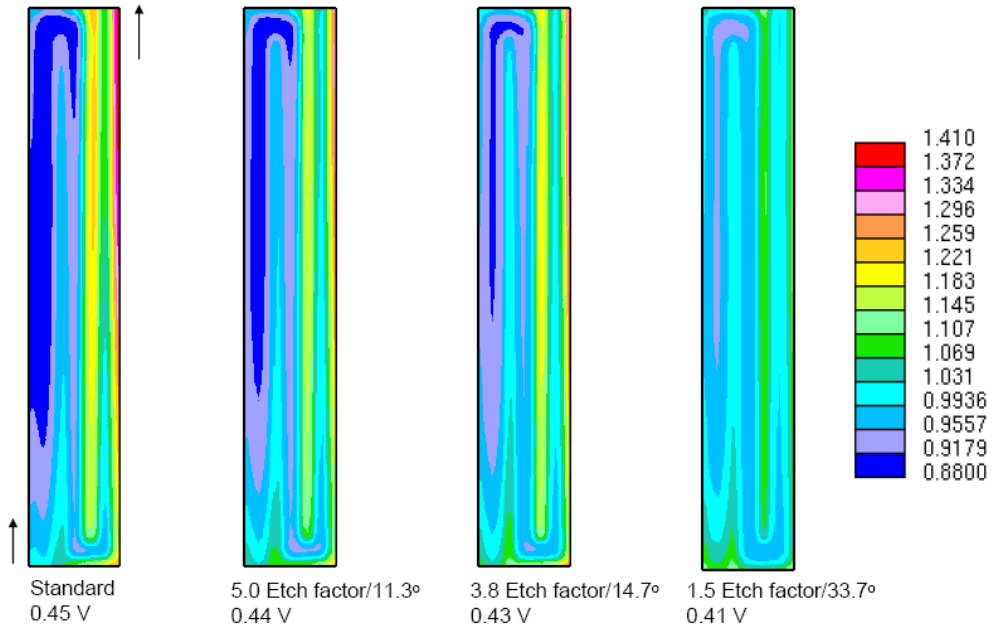

b)

Figure 3.7. The effect of draft angle on current density distribution at I_{avg} = 1.0 A/cm^2 under (a) Stationary condition and (b) Automotive condition.

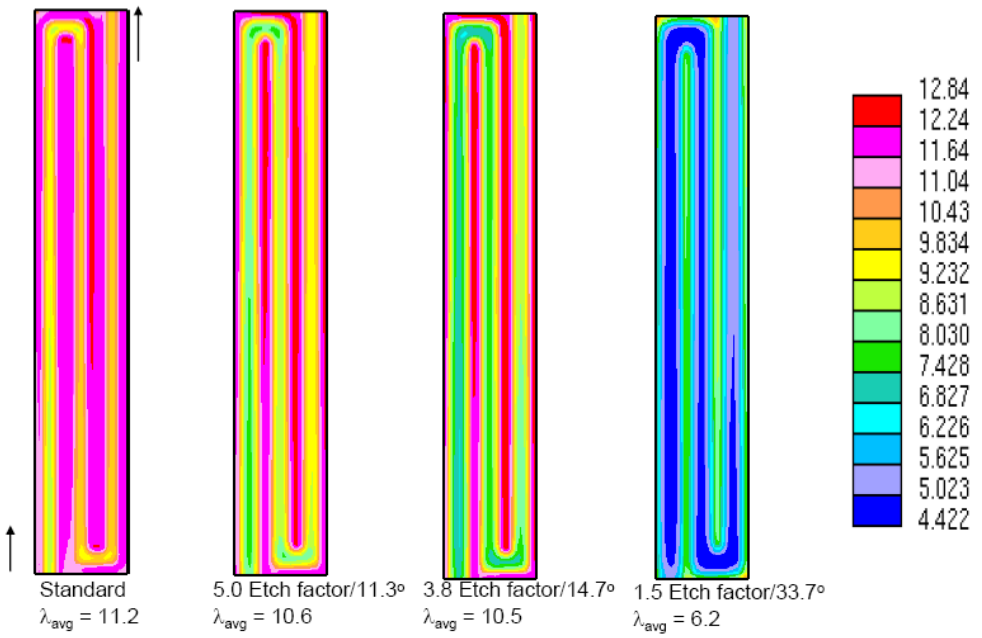

a)

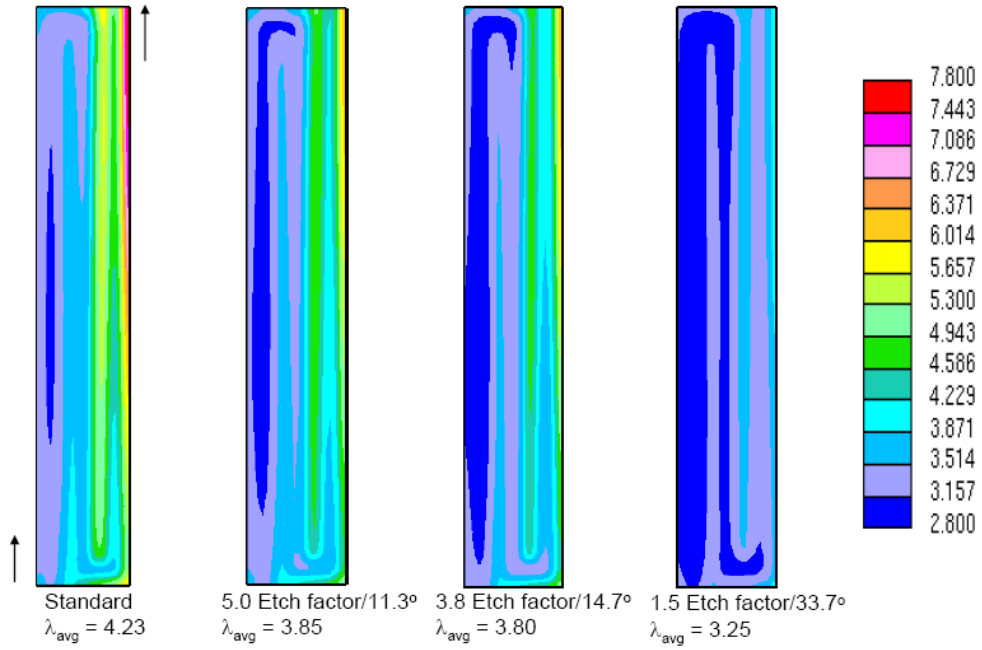

b)

Figure 3.8. The effect of draft angle on membrane water content distribution at I_{avg} = 1.0 A/cm2 under (a) Stationary condition and (b) Automotive condition.

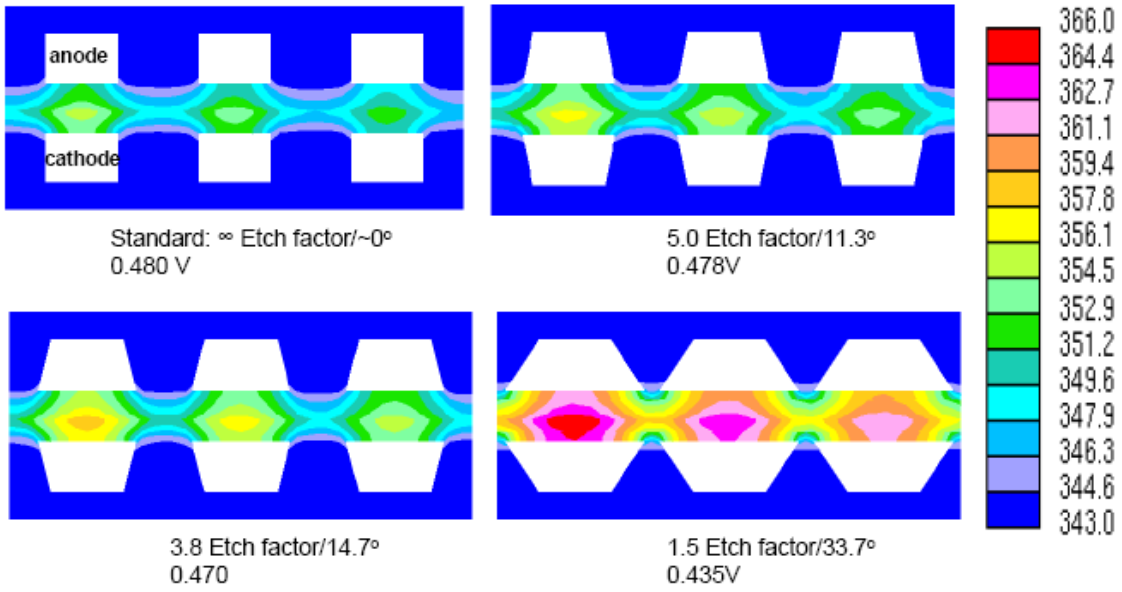

Figure 3.9. The effect of draft angle on temperature (K) distribution at cross section plane (15mm,y,z) for I_{avg} = 1.0 A/cm2 under Stationary condition.

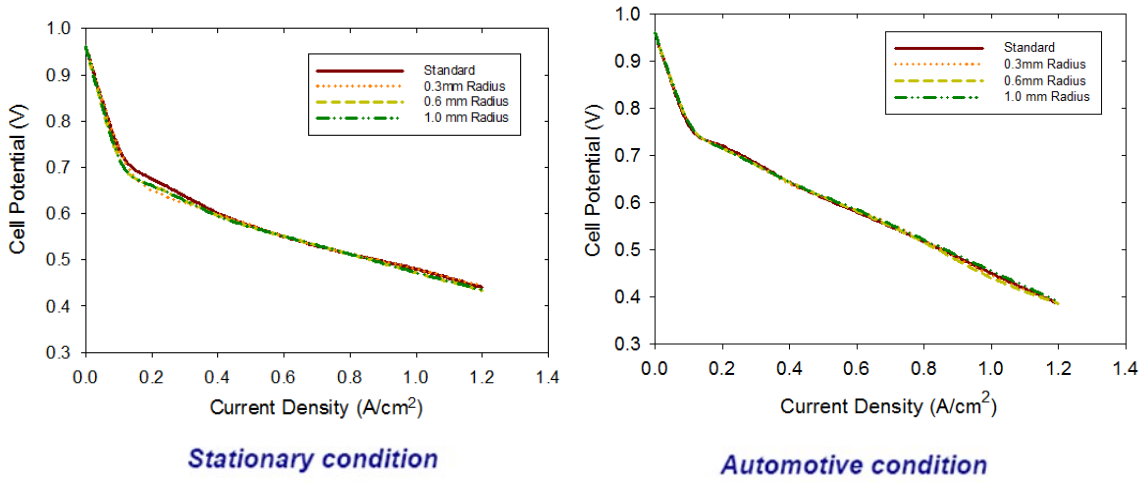

(a)

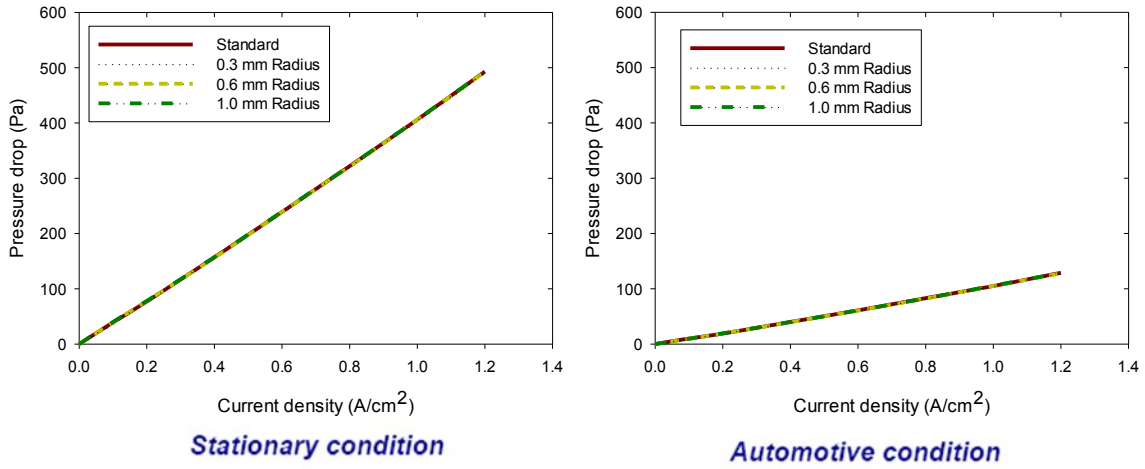

(b)

Figure 3.10. The effect of channel radius on (a) PEMFC performance and (b) maximum pressure drop (Pa) under Stationary and Automotive conditions.

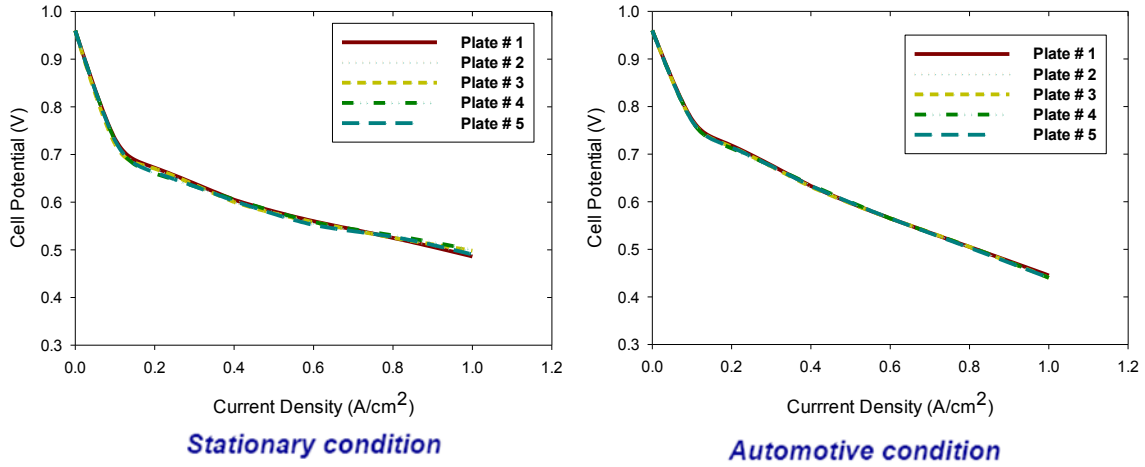

(a)

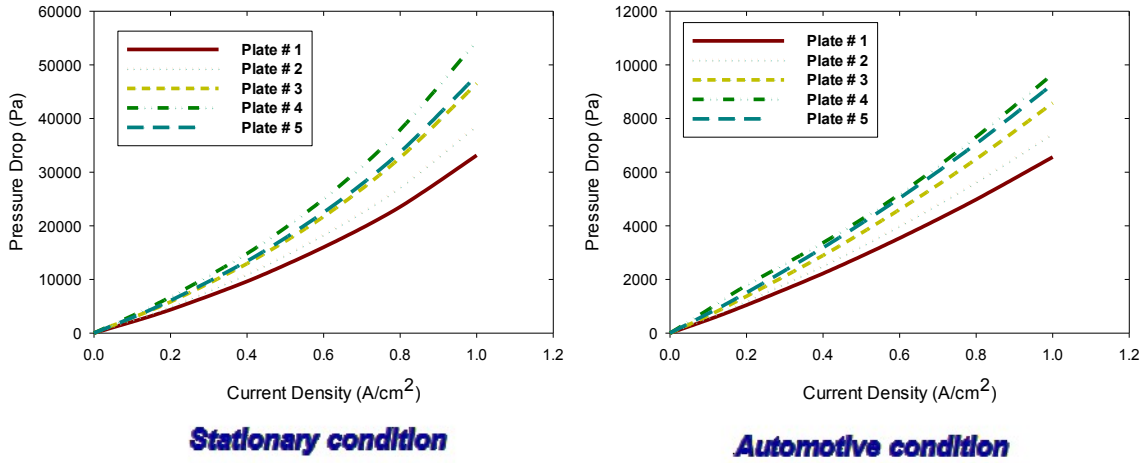

(b)

Figure 3.11. The effect of channel depth uniformity on (a) PEMFC performance and (b) maximum pressure drop (Pa) under Stationary and Automotive conditions.

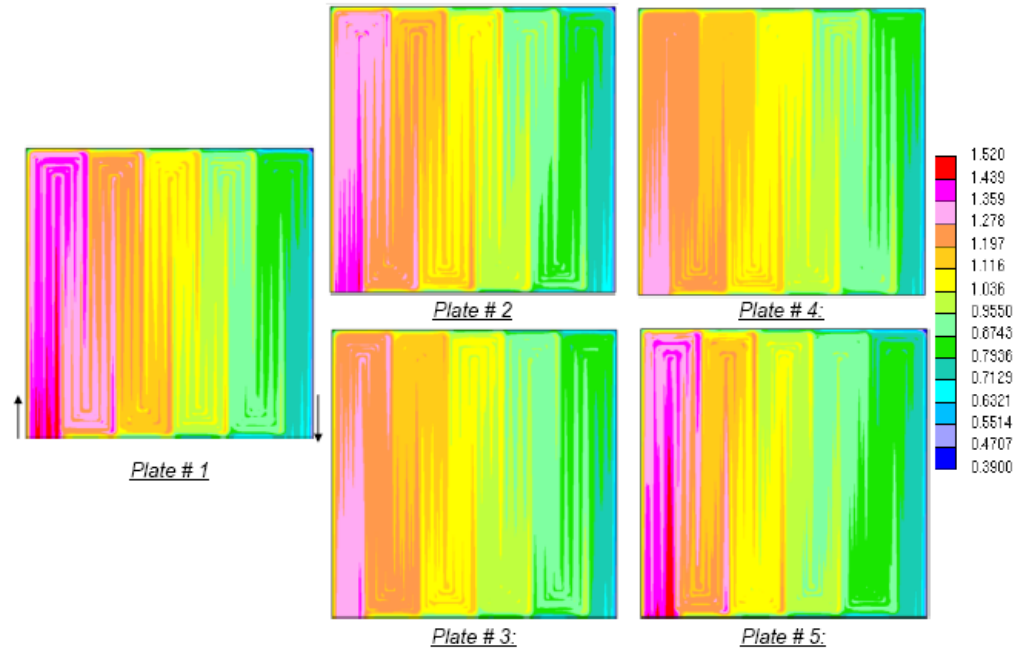

(a)

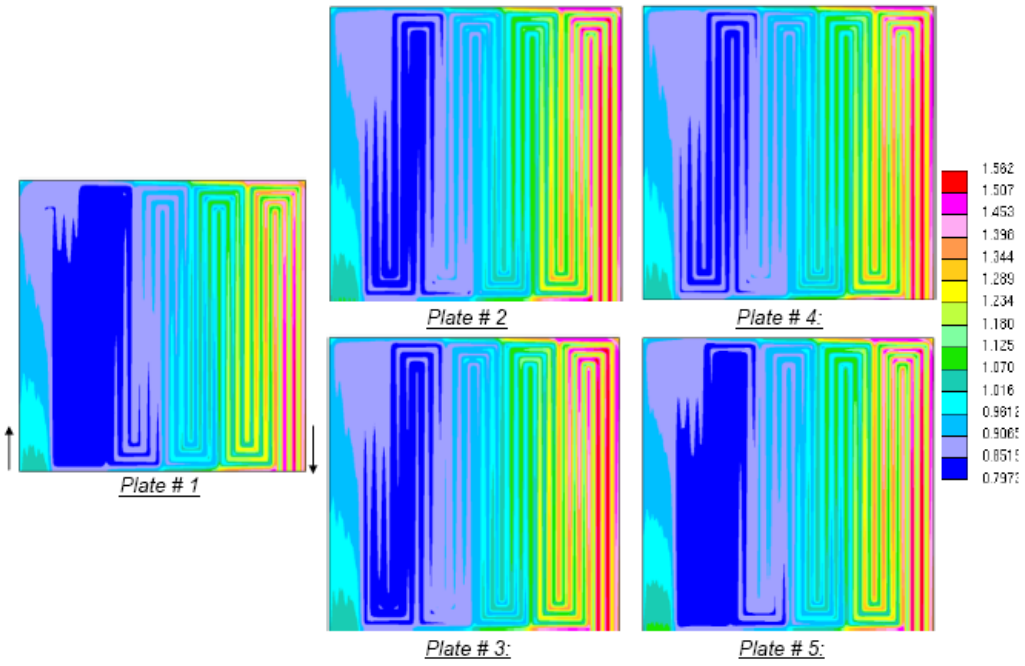

(b)

Figure 3.12. The effect of channel depth uniformity on current density distribution at I_{avg} = 1.0 A/cm^2 under (a) Stationary condition and (b) Automotive condition.

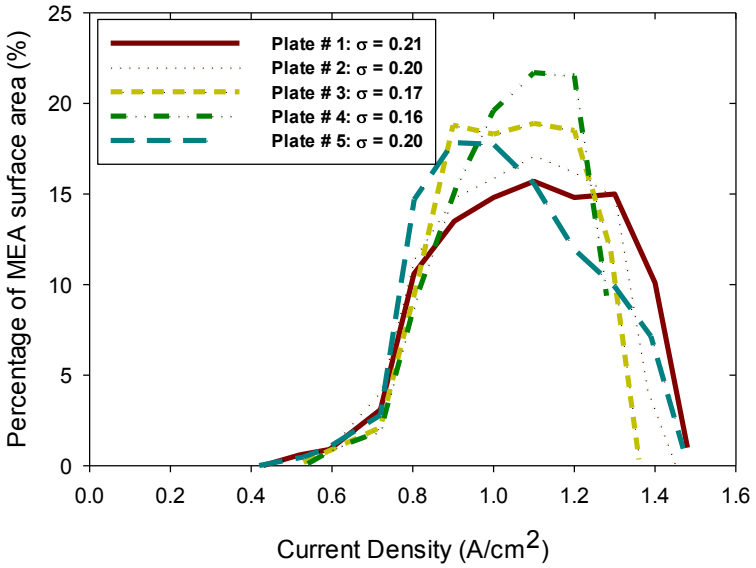

(a)

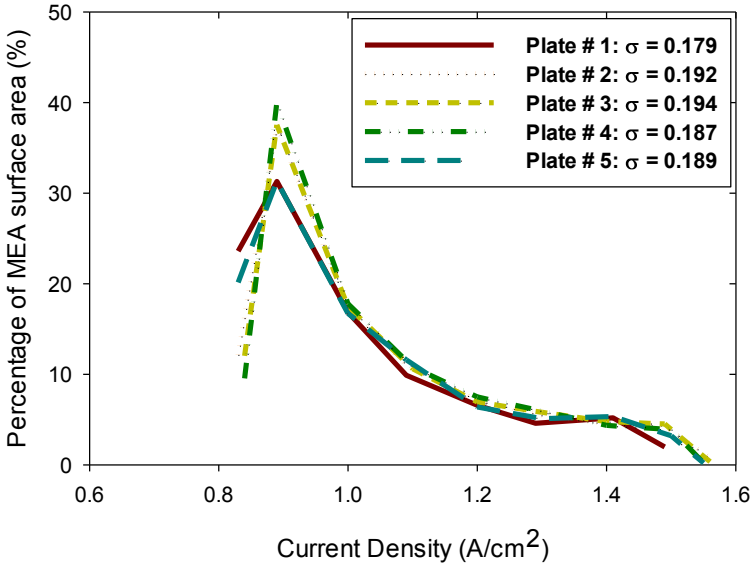

(b)

Figure 3.13. The effect of channel depth uniformity on area distribution of current density at I_{avg} = 1.0 A/cm^2 under (a) Stationary condition and (b) Automotive condition.

CHAPTER 4

FUNDAMENTAL ANALYSES, OBSERVATIONS, AND PREDICTIONS OF LIQUID DROPLET MOVEMENT ON ETCHED-METAL SURFACES FOR PEMFC

In a proton exchange membrane fuel cell (PEMFC), the liquid transports from the cathode generating site through the gas diffusion layer (GDL) and then into the flow channel of the bipolar plate. There can be significant liquid droplet accumulation on the surface of the flow channel on either side of the membrane. Liquid water and flow dynamic characteristics in the transparent channel consisting of an optical window were studied experimentally. Ex-situ observations of the liquid water and flow patterns inside the channel were established. In this work, liquid water droplet movements were analyzed by considering the change of the contact angle by flow velocity. Also, various stainless steel surfaces having different surface roughness were used to determine the relationships between flow rate and the contact angles. The pressure drop and channel characteristics become more important when liquid water presents in the gas channels of PEMFCs. Characteristics of water droplet motion in the flow channels of PEMFCs are important. The model equation was derived to describe the relationship between contact angle and surface roughness of stainless steel surface.

4.1 Introduction

Proton Exchange Membrane Fuel Cells (PEMFCs) are energy converters suitable for various applications with differing requirements. Liquid water transport, accumulation, and removal are the major problem in maintaining high performance in PEMFCs operation [12, 13]. Generally, water is produced in cathode catalyst layer, and liquid water transports in gas diffusion layer (GDL) by pressure gradient in flow channel [84]. Excess liquid water may prevent the anode and cathode gas transports to the catalyst site, a phenomenon commonly known as "flooding". Also, the liquid accumulation inside the fuel cell is mostly observed in the GDL [85]. Turhan et al. [86] addressed significant liquid droplet accumulation in fuel cell occurred on the surface of flow channel with in-situ neutron imaging. These existences of liquid droplet has strongly effect pressure gradient in flow channel. Water management is a key issue in PEMFCs, which is a significant technical challenge and is of vital important to achieve maximum performance and durability from PEMFCs.

Among all of fuel cell components, bipolar plate is the component that has liquid droplet be presented the most [87]. Also, the bipolar plate is one of the major components that contribute in the PEMFCs manufacturing cost [1-3]. The present research focuses on metal bipolar plate manufactured by electrochemical etching technology, which is a low cost, high volume manufacturing process for metallic bipolar plates capable [6, 7]. The experiments were setup on different surface roughness of electrochemical etching steel plate [16].

The contact angle of droplet is another important factor, which used to characterize the wettability of solid surface [88]. It was introduced by Thomas

Young[89]. The contact angle is related to the interfacial tension of solid, liquid, and vapor. Young proposed an equation describing the contact angle on a smooth surface by considering the interfacial energies at the triple line where the solid, liquid, and vapor phases contact as shown in Figure 4.1.

$$\cos\theta = \frac{\gamma_{SV} - \gamma_{SL}}{\gamma_{LV}} \tag{4.1}$$

where γ_{SL}, γ_{SV} and γ_{LV} indicate the interfacial free energies per unit area of solid-liquid (*SL*), solid-gas (*SV*), and liquid-gas (*LV*) interfaces, and θ is the contact angle of droplet. If the liquid wets the surface (hydrophilic surface), the value of the static contact angle is $0 \leq \theta \leq 90^{\circ}$, whereas if the liquid does not wet the surface (hydrophobic surface), the value of the contact angle is $90° \leq \theta \leq 180°$

Wenzel [90] proposed an equation describing the contact angle on a rough surface by modifying Young's equation to the following:

$$\cos\theta' = \frac{r(\gamma_{SV} - \gamma_{SL})}{\gamma_{LV}} = r\cos\theta \tag{4.2}$$

where r is a roughness factor and θ' is the apparent contact angle. In this equation, value of r is always larger than unity. Therefore, surface roughness improves hydrophilicity of hydrophilic surface under these parameters. For this reason, the contact angle will be decreased from the roughness of the surface.

Cassie-Baxter [91] reported an equation describing the contact angle at a heterogeneous surface composed of solid and air. When a unit area of the surface has a wetted solid surface area fraction (f) with a water contact angle θ, the contact angle on the surface can be expressed using the following equation, assuming water-air contact angle of is 180°

$$\cos\theta' = f\cos\theta + (1-f)\cos 180° = f\cos\theta + f - 1 \quad (4.3)$$

There were many works on the validity and derivation of the Wenzel and Cassie-Baxter equations [92-96]. When the surface roughness is significant, the Cassie-Baxter's model is more important than Wenzel's [97]. In the case of Cassie-Baxter's model, the liquid droplet on the rough surface can cause air to be trapped between solid and liquid interface, resulting in addition of air-liquid interfaces. Bikerman et al. [17] have studied water droplet on different surface roughness of stainless steels with the contact angle round 90˚ and proposed that the surface roughness provides resistance for sliding water droplet movement.

The behavior of the liquid droplet was predicted on the basis of dynamic contact angle measurements, which can be estimated the adhesion force on the surface. During the experiment, the dynamic behavior of the droplet was analyzed through the contact angle measurements as reported by Theodorakakos et al. [98]. In this work, various surfaces roughness of stainless steel was chosen to study the effects of surface properties on the droplet behavior.

4.2 Experimental Procedure

To determine the onset of distortion and movement of a drop in a small flow channel, an experimental channel was setup as shown in Figure 4.2. This figure shows a picture of the channel assembly used in this experiment and it was reported by Venkatraman et al. [15]. It consists of three parts: a top, a bottom, and an inserted floor. The top and bottom are constructed from transparent polycarbonate (PC). This allows an observation of water drops inside the channel. The top piece was solvent polished to

produce an optical finish. The bottom part has slot for inserting a piece of sample. The inserted floor, located in the mid-length of the channel, is for installing the sample. The sample can be changed for different materials those are being studied. To determine the distortion and movement of liquid droplet under different surface properties, few samples of electrochemical etching stainless steel plate were placed into the inserted channel floor space. For visualization, this experiment must be performed in larger channel than typical fuel cell flow channel but keeping the same ratio of channel width (*w*) and channel depth (*d*) of 2.0In this work, ,*w* is 4 mm and *d* is 2 mm while the typical fuel cell's flow channel, *w* is 1.0 mm and *d* is 0.5 mm . The length of the channel is 120 mm which is sufficient for the flow rate up to 2500 cm3/min to be fully developed at laminar flow. One side of the channel is connected via compressed air pressure through a pressure regulator and a nozzle valve is controlled by flow meter to control flow rates. The other side air and pressure is set slightly above 1 atm.

Venkatraman *et al*. [15] have studied the effect of the droplet height per the depth of flow channel (*h/d*) to pressure drop in the channel. They found that if the droplet hight per the depth of flow channel (*h/d*) is grater than 80%, it has a significant to pressure drop in flow channel. The 10 μL of liquid water droplet size, which is equivalent to h/d of 84 % respectively, was chosen to perform the experiments.

A 10 μL water drop was placed on top of the sample piece and then the channel was closed. The air was applied to a channel for this experiment which corresponding to cathode side of PEMFC. The air was exposed to a channel at certain flow rate which controlled by mass flow controller. Then, the shape of the water drop is monitored by the microscope. Because water can evaporate, especially at higher air flow rates, a new

droplet was replaced after exposed the air to a channel and the experiment is repeated at progressively higher flow rates. The flow rate was gradually increased from 0 to 2500 cm^3/min (Re = 0 to 925). The experiment was stopped if the droplet begins to move. All experiments are performed at 25 ºC.

Reynolds numbers (Re), for the various volumetric flow rates (Q) and cross-sectional areas (A), were computed using the density (ρ) and viscosity (μ) of dry air at 1 atm and 25 ºC, ρ = 1.205 kg/m^3 and μ = 1.81 x 10^5 Pa·s,

$$Re = \frac{\rho Q D_r}{A\mu} \tag{4.4}$$

where D_h is the hydraulic diameter of the rectangular channel [99]. The hydraulic diameter was calculated using the wetted perimeter (P) and the cross-sectional area:

$$D_h = \frac{4A}{P} = \frac{4wd}{2d + 2w} = \frac{2}{3}w \tag{4.5}$$

The contact angles (θ) of liquid drops were measured to verify the assumption that drops were spherical segments. Advancing and receding contact angles, θ_a and θ_r, of distorted drops were measured from images using a protractor. Figure 4.3 illustrates the water droplet deformation and the changing of advancing and receding contact.

4.3 Theoretical analysis of macroscopic force balance

A macroscopic force balance has been established in the flow channel in order to predict the behavior of the water droplet [100]. In general, the shape of the liquid droplets on the surface is controlled by the normal stress on the free surface as a result of gravity, fluid flow within the drops, and surface tension. The gravity does not affect the small droplets, and the shape of a simple drop is spherical. Figure 4.4 illustrates a macroscopic

force balance model of the droplet in the presence of air flow. The control volume is defined as A and B planes, with a depth equal to the diameter of the droplet. The pressure difference between A and B is the total pressure force. Pressure force (F_p) is created by pressure difference in the flow field and can be written as,

$$F_P = (P_A - P_B) \times Area \tag{4.6}$$

where P_A and P_B represent the pressure at A and B plane. The drag force (F_{drag}) is caused by fluid shear along the droplet surface and it is a function of the flow velocity. The pressure gradient is the total exerted force on the droplet. Therefore, the macroscopic force balance in the x-direction is given by

$$F_{drag} = F_P + F_{shear} \tag{4.7}$$

where F_{shear} represents the shear force which the fluid exerts on the top due to the no slip condition. In static condition, F_{drag} is balanced by Surface tension force (F_{st}). Surface tension force is the force that is directly related to adhesion tension and surface contact angles of the droplet emerging on the plate. Equation 4.8 represents the stable condition. If the adhesion force is equal or more than the drag force, the droplet will not move from the channel. The critical condition is defined as the point before the droplet starts to move. In the force balance model, the critical state is the point when surface tension (F_{ST}) is balanced by drag force. If F_{drag} is increased above the critical point, the droplet will become unstable and start to move from the channel.

$$F_{ST} \geq F_{drag} \tag{4.8}$$

The surface tension force is a key factor in the force balance equation because it is directly related to traction and surface contact angle of water droplets emerging in the channel surface. By considering the flow of gas to be Newtonian, fully developed, and

laminar, the pressure drop is related to pressure, average velocity, and height of the channels. The pressure drop across the control volume can be written [100, 101],

$$P_A - P_B = \frac{3\mu u'}{b^2} 2r \tag{4.9}$$

where u′ is the average velocity above the droplet. Based on incompressible fluid, u′ can be approximately, $u' = (B/b)U$, where U is the average velocity of air in channel. From equations 4.6 and 4.9, the pressure force become,

$$F_P = \frac{24\mu B^2 U h^2}{\left(B - \frac{h}{2}\right)^3 (1 - \cos\theta_A)^2} \tag{4.10}$$

where

$$r = \frac{h}{1 - \cos\theta_A} \tag{4.11}$$

The shear stress at the top wall of Newtonian fluid is

$$\tau_{xy} = \frac{3\mu u'}{b} \tag{4.12}$$

Substituting *u'* and *b*, the shear force of the control volume becomes

$$F_{shear} = \frac{3\mu BU}{\left(B - \frac{h}{2}\right)^2} (2r)^2 \tag{4.13}$$

From equation above, the drag force was calculated by droplet geometry and the Reynolds number.

4.4 Result and discussions

This experiment was setup to understand liquid water droplet behavior inside the flow channel at different Re and to study the effect of surface roughness on contact angle and pressure drop inside flow channel.

4.4.1 Effect of surface roughness on contact angle

The static contact angle of droplet on different surface roughness was measured as shown in Figure 4.6. This figure shows static contact angle of 10 μL liquid water droplet on different surface roughness. The results show that static contact angle of droplet increased with large surface roughness (Ra). In this case, the static contact angle of droplet on a stainless steel plate is 82° for Ra=0.02 μm, 85° for Ra=0.30, 86° for Ra=0.27, and 95° for Ra=0.73 μm. Thus, the contact angle is depending on surface roughness. Moreover, with the same volume of droplet, the height of the droplet also depends on the contact angle. The height of droplet is increased with the growth of the contact as shown in Figure 4.6.

From the results, we propose a model describing contact angles on rough surfaces by using combination of Wenzel's and Cassie-Baxter's models[102]. The surface roughness was assumed as a series of uniform needles, as illustrated in Figure 4.7. The contact angle on this model surface is described by equation as follows

$$\cos\theta' = rf\cos\theta + f - 1 \qquad (4.14)$$

where θ' is the apparent contact angle on a rough surface, θ is the equilibrium contact angle on a flat surface, r is a roughness factor, and f is the solid surface area fraction. The roughness factor (r) is the ratio of the side area to the bottom area of the needle, which is represented by 2a/b in Figure 4.7. The solid surface area faction (f) is area fraction of the surface contacted with water, which is represented in one dimension to be $\sum b / (\sum b + \sum c)$ in Figure 4.7. Using this equation, the relation between contact angles on the surface and surface roughness can be derived. The water interface area to surface area is represented by rf.

From the uniform needles model, the roughness factor, *r*, can be calculated from the surface roughness number, Ra. The definition of the Ra is shown in Figure 4.8. The ratio of the side area to the bottom area of the needle *r* can be derived from the model. Figure 4.9 shows relationship between the base value of uniform needles and calculated value of roughness factor (*r*). These graphs show that if the base size is too large, there is no different of roughness factor with different surface roughness. On the other hand, if the base is too small, these unreasonably enhances roughness factor. The base of the needles was selected as 1 μm showing appropriate value of roughness factor (*r*).

$$Ra = \frac{\frac{1}{2}hx}{x} = \frac{1}{2}h \tag{4.15}$$

$$r = \frac{2\sqrt{\left(\frac{x}{2}\right)^2 + h^2}}{x} \; ; x = 1\ \mu m \tag{4.16}$$

Table 4.1 shows the value of *r* and *f* from the model with surface roughness and contact angle. The results shows that contact angle increased while area fraction of the surface decreased. This means more air can be trapped in rougher surface.

4.4.2 The effect of surface roughness on pressure drop.

Figure 4.10 illustrates the sequence photography of dynamic behavior of the 10μl water droplets on the stainless steel plate with roughness (Ra=0.73μm) under different flow rate (Re). The flow rate of air inlet was initiated at 0 cm^3/min (Re=0) and then gradually increased. The results show that contact angle hysteresis increased with high flow rate (large Reynolds number) for every values of the roughness. These results are similar to the sliding angle of droplet [93, 103]. The shape of droplet at different flow rates (Re) was observed. From these sequence photographs, the shapes of droplet with different Ra at each Re were combined together as shown in Figure 4.11. The dimensions

such as height of water droplet were used to calculate the pressure drop across droplet as shown in Equation 4.9.

Low flow resistant is the aim of flow in the gas channel and the pressure drop indicates flow resistance of the gas channel. Thus, pressure drop in the flow channel is an important parameter to evaluate the performance of the gas flow channel. Figure 4.12 shows the result of calculate pressure drop at critical point before droplet moved versus roughness of the flow channel. The result indicates that pressure drop is increased with increasing the rougher surface of the flow channel. From Equation 4.9, the height of the droplet has critical impact to pressure drop in the flow channel, which is significant increased with the height of droplet. Note that the larger contact angle on the surface yields the higher of the droplet height. Sakai et al. [93] stated that there is the resistance force relate to solid surface against pressure force which holding the droplet on the surface.

From sliding angle of droplet, Wolfram and Faust [104] proposed an empirical equation relating the sliding angle of droplets on surface of various materials

$$mg \sin \alpha = k^2 R\pi \tag{4.17}$$

where m is the weight of droplet, g is the gravitation acceleration, α is the sliding angle, R is the radius of contact circle, and k is a proportionality constant. Bikerman [17] also recommended similar equation of sliding angle of droplets on different surface roughness that

$$mg \sin \alpha = kw \tag{4.18}$$

Where w is the width of the droplet and k is constant. The value of k increased with surface roughness. For droplet in the flow channel, the term $mg \sin\alpha$, gravitation force, can be written as a pressure force instead.

Miwa et al. [102] point out that the interaction energy between water and solid surface is proportional to the contact area, which is rf times as the apparent contact area. Therefore, the constant k in equations 4.17 and 4.18 is assumed to be rf times for flat surface. Figure 4.13 represents relation between the total drag force from the calculation in Figure 4.5 with the square of roughness factor and solid area fraction, $(rf)^2$. It is inferred that the surface tension force of solid surface was governed by solid area fraction f and roughness factor r.

4.5 Conclusions

In this study, the droplet deformation and removal from surface of a fuel cell channel was determined by employing visualization of a water droplet in a presented air flow. The contact angles measurement on different surface roughness were reported. The results show that contact angle slightly increases with the increasing of surface roughness. Surface model given in this work can describes the relationship between contact angle, roughness factor and solid area fraction. This model reveals that surface structures that can trap air between liquid and solid interface is importance. Also, the interaction energy between water and substrate is proportional to the true contact area. The resistant force, which is act against the pressure force, is governed by of solid area fraction and roughness factor. Resistant force is proportional to square of solid area faction and roughness factor $(rf)^2$. Relatively smooth flow channel may help to reduce

pressure drop cause by liquid droplet and also improve the water removal away from flow channel.

Table 4.1. Effect of surface roughness on wetting properties of stainless steel in the present of water droplet.

Ra (μm)	Contact angle (deg)	roughness factor (*r*)	surface area fraction (*f*)
0.02	82	~1	~1
0.27	86	1.5	0.88
0.3	85	1.6	0.89
0.41	87	1.9	0.83
0.73	94	3	0.66

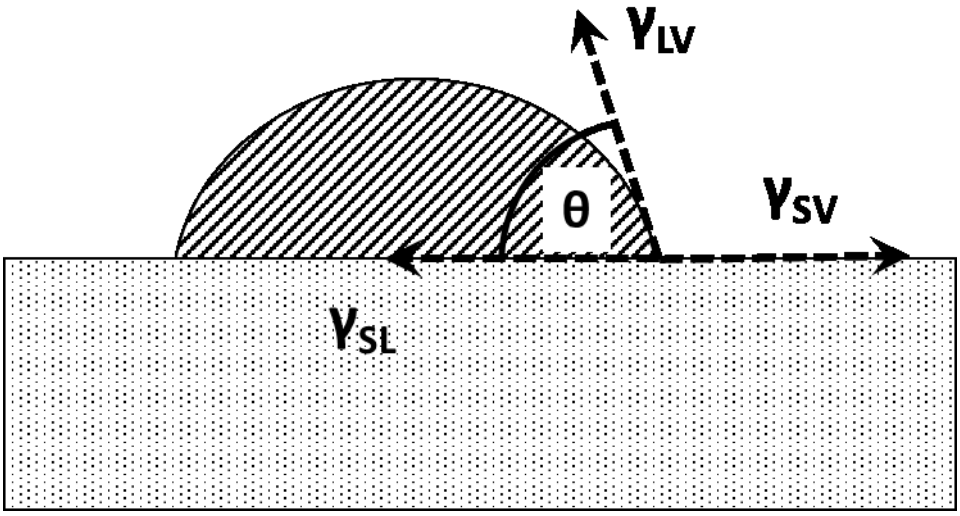

Figure 4.1. Schematic of contact angle of droplet wetted to surface.

a)

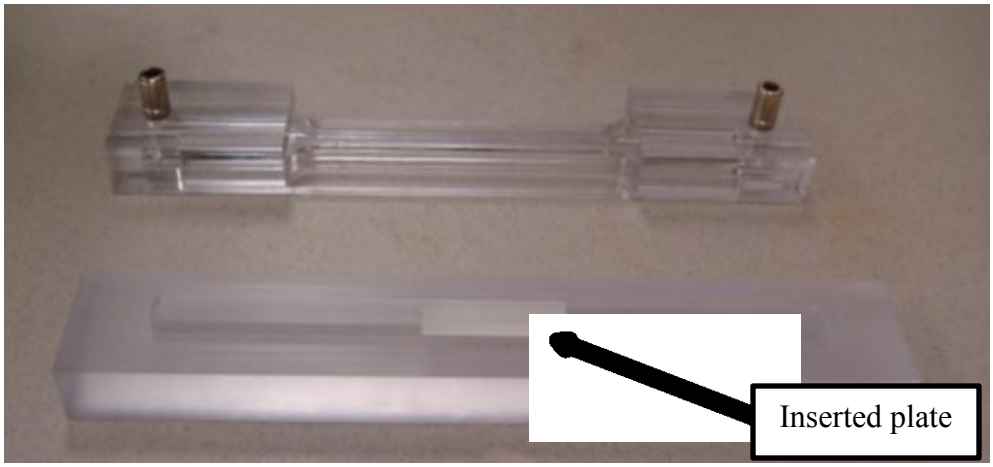

b)

Figure 4.2. Photography of the flow channel used in this study
a) assembly of channel and c) 3 pieces of channel
(channel width = 4 mm, channel depth = 2 mm and channel length = 120 mm).

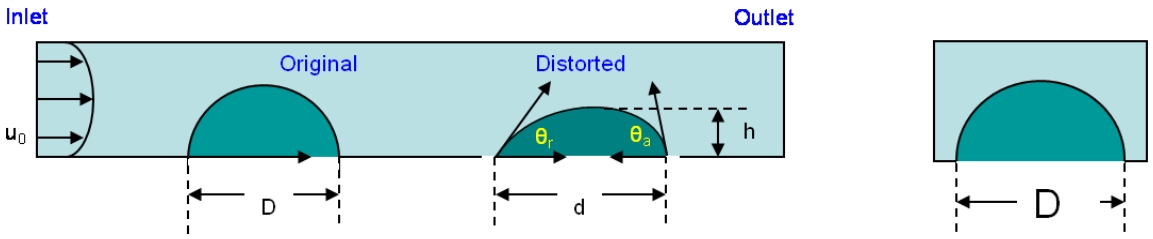

Figure 4.3. Schematic of the drop in the flow channel used in this study.

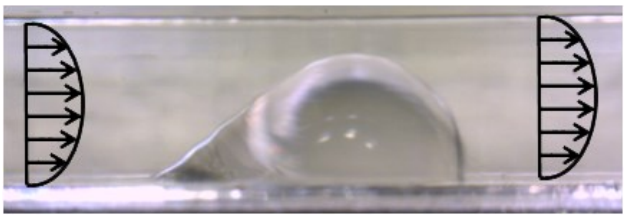

a)

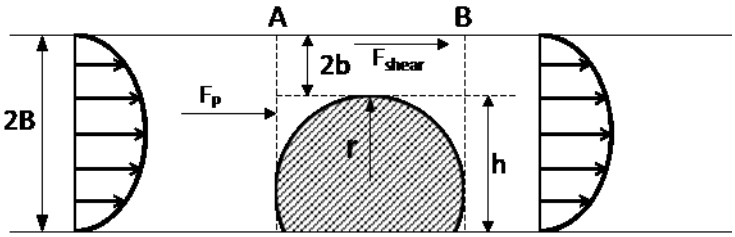

b)

Figure 4.4. a) Image of the droplet in the presence of air flow and b) schematic view of control volume chosen for analysis.

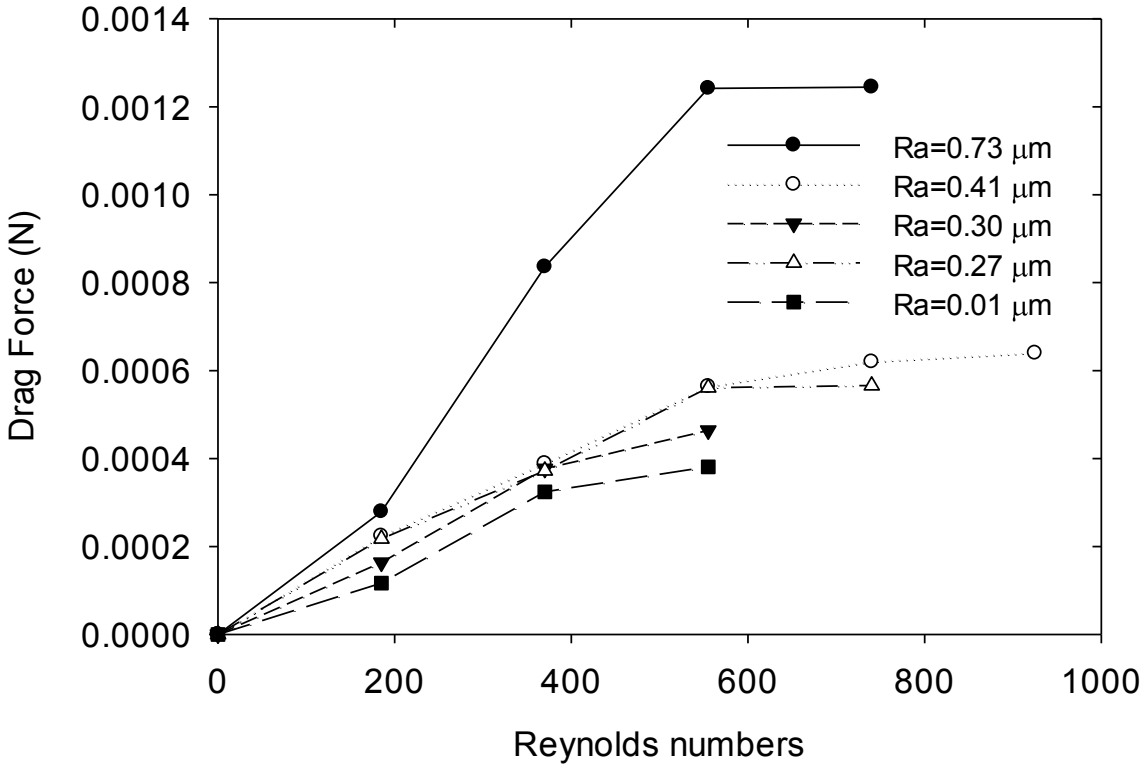

Figure 4.5. Total drag force vs. Reynolds number for different roughness surface.

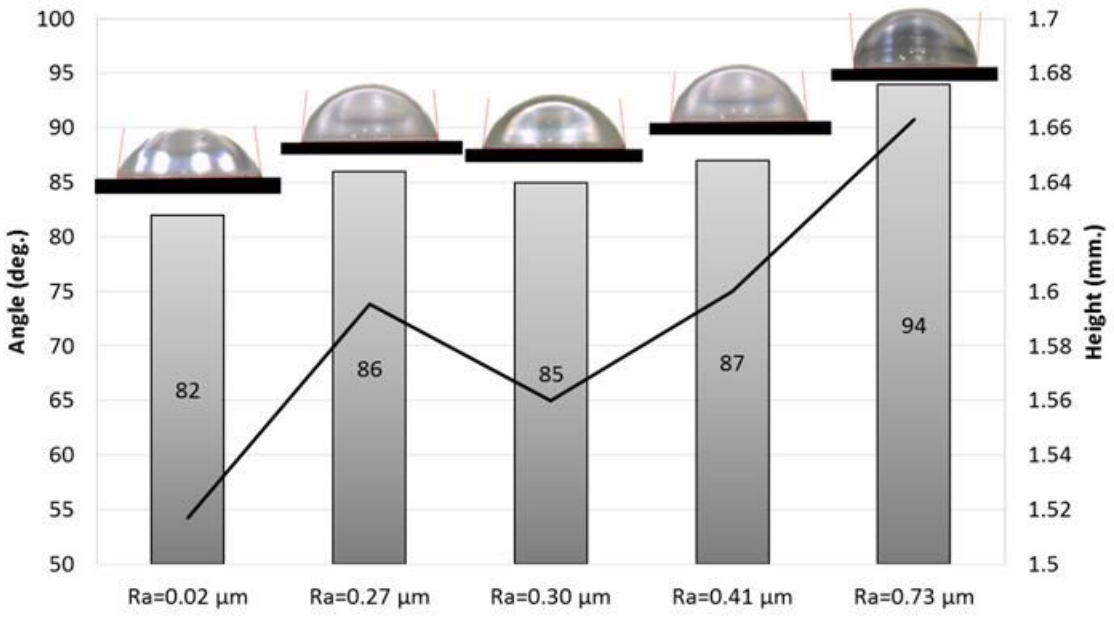

Figure 4.6. Static contact angle of 10 µL water droplet on stainless steel plate.

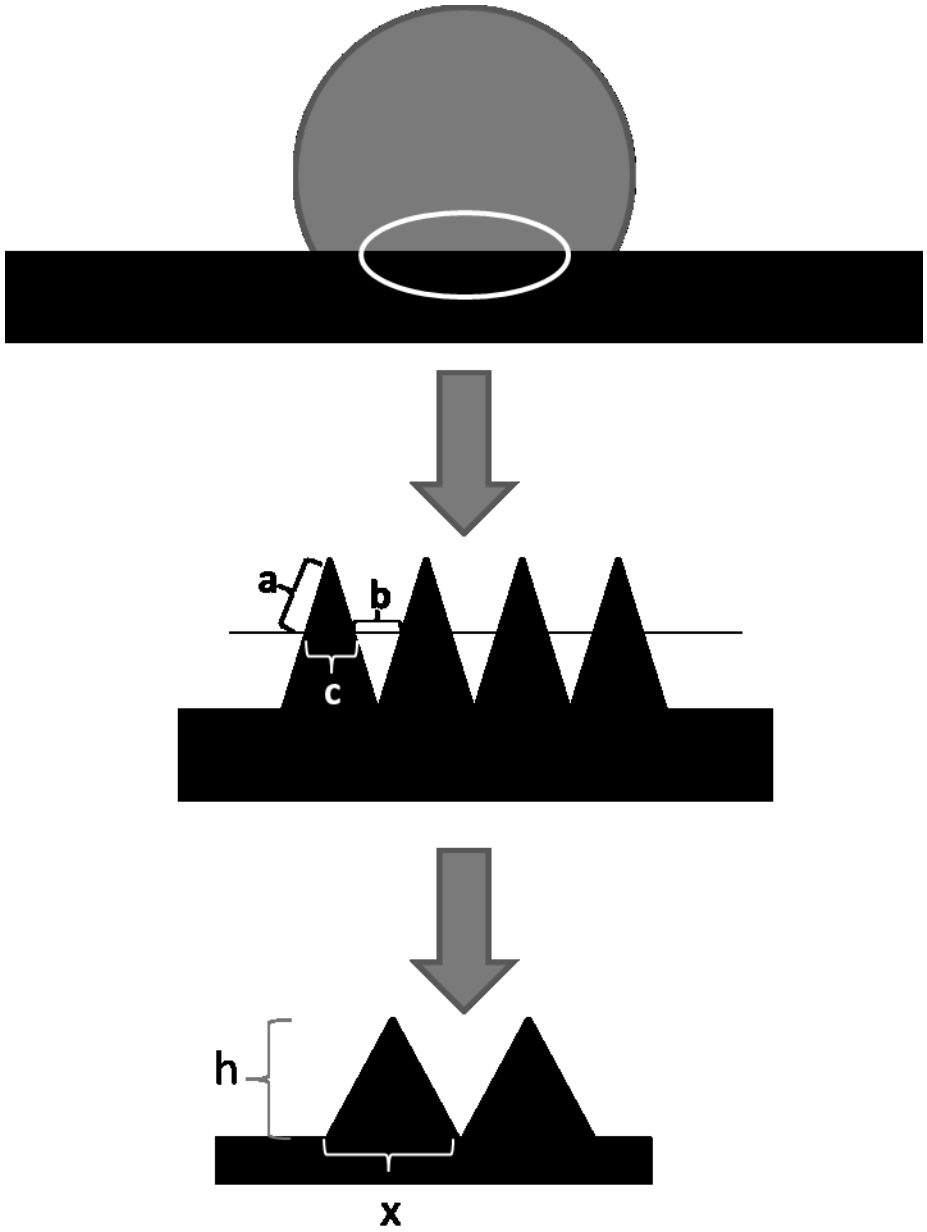

Figure 4.7. Schematic illustration of the surface model with a series of uniform needles.

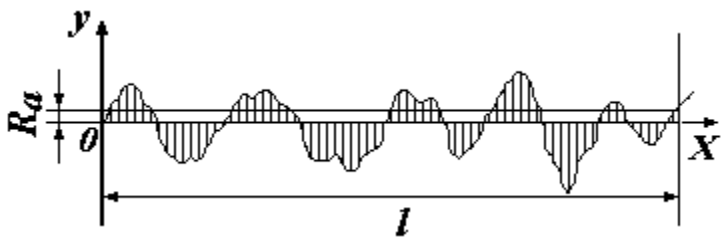

$$Ra = \frac{1}{l}\int_0^l |f(x)|dx$$

Figure 4.8. Schematic illustration of surface roughness.

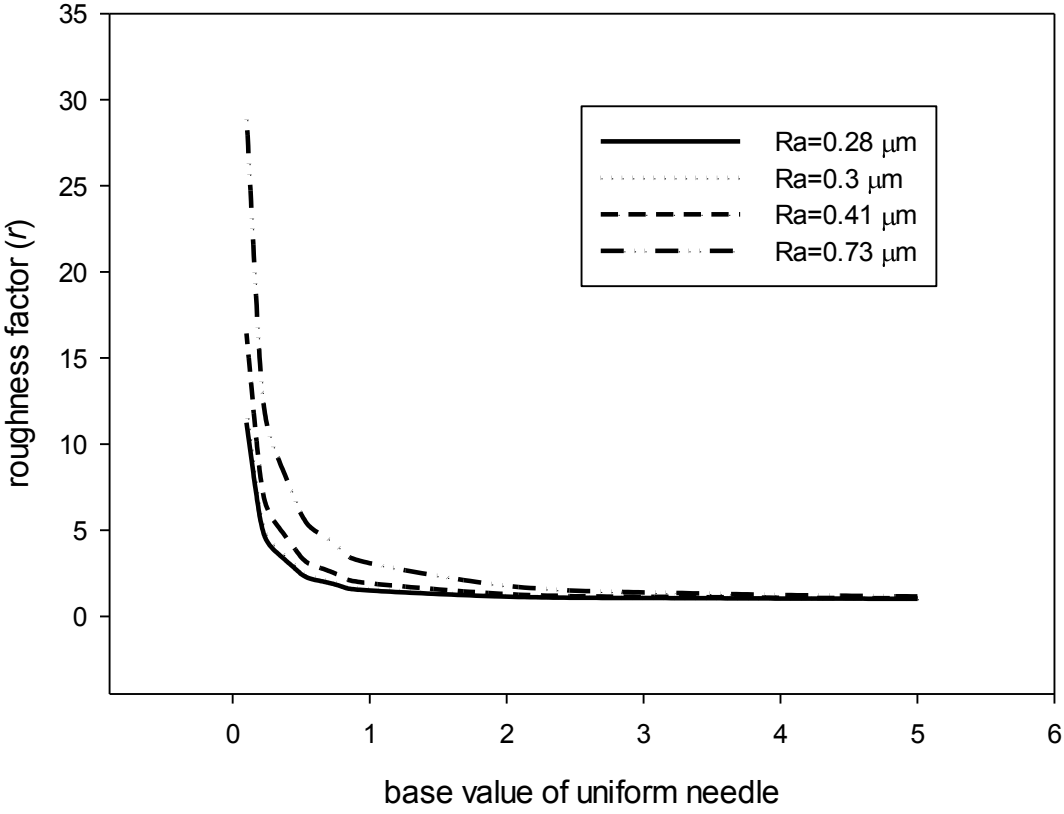

Figure 4.9. The plot of relationship between roughness factor (r) and base value of uniform needle.

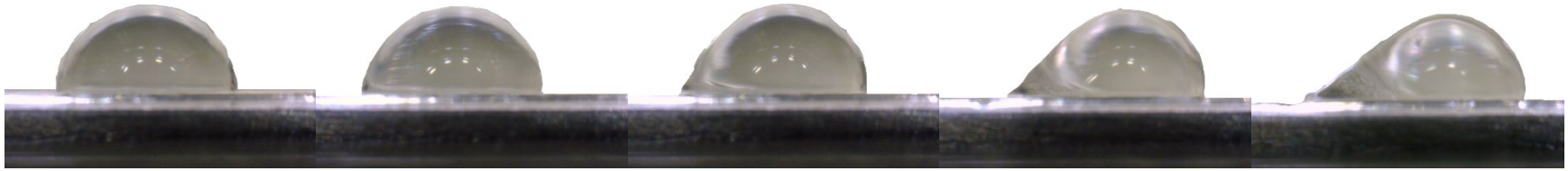

Re=0 Re=185 Re=370 Re=555 Re=740

Figure 4.10. Dynamic images of the water droplet on electrochemical etching stainless steel plate (Ra=0.73 μm.) at different Re.

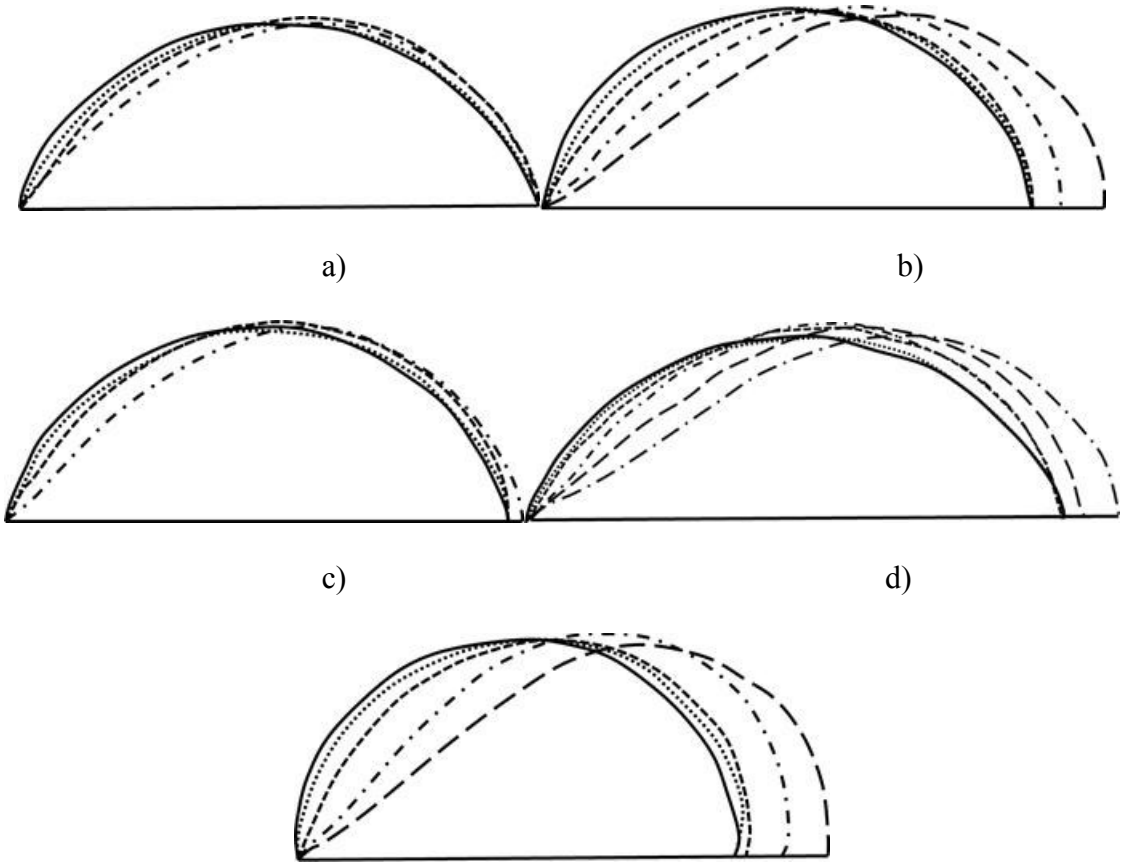

Figure 4.11. Water droplet profile at different Reynolds number
a) on Ra = 0.02 μm, b) on Ra = 0.27 μm, c) on Ra = 0.30 μm,
d) on Ra =0.41 μm, and e) on Ra = 0.73 μm

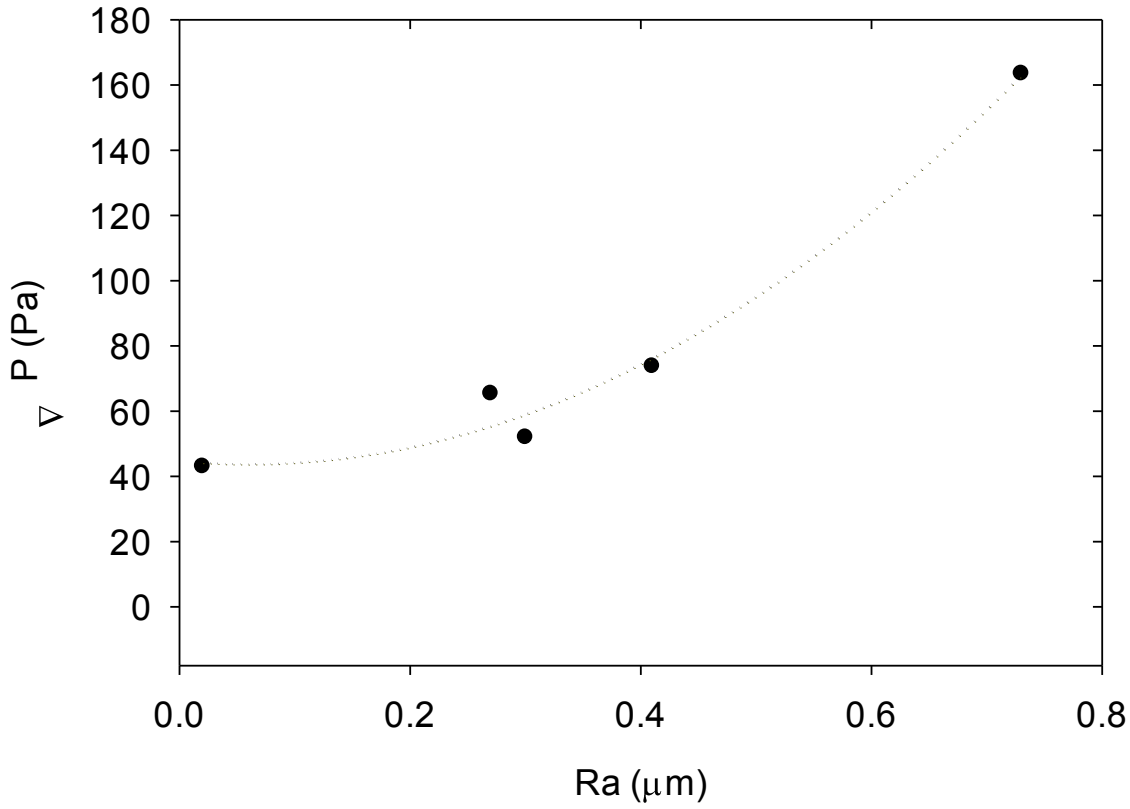

Figure 4.12. Pressure drop pressure drop at critical point vs. surface roughness (Ra).

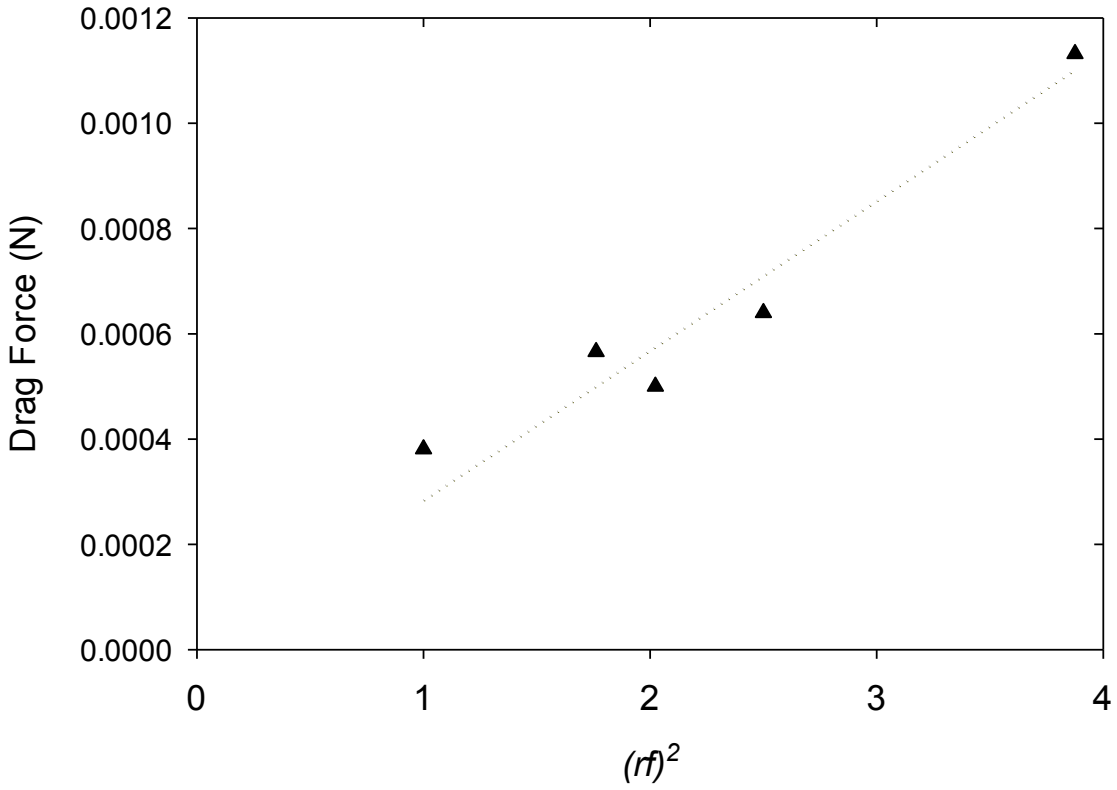

Figure 4.13. Relation between the squre of solid area (rf^2) to the total drag force.

CHAPTER 5

CURRENT DISTRIBUTION BOARD FOR PEM DEVICES

A developed measurement system for current distribution mapping has enabled a new approach for operational measurements in Proton Exchange Membrane Fuel Cells. Currently, there are many issues with the methods to measure current distribution; some of the problems that arise are breaking up the fuel cell component and these measurements are costly. Within this field of work, there is a cost effective method of mapping the current distribution within a fuel cell while not disrupting reactant flow. The physical setup of this more efficient method takes a current distribution board and inserts it between an anode flow field plate and a gas diffusion layer. A From this layout, the current distribution can be directly measured from the current distribution board. This novel technique can be simply applied to different fuel cell hardware. Further it also can be used in fuel cell stack by inserting multiple current distribution boards into the stack cells. The results from the current distribution measurements and the electrochemical predictions from computational fluid dynamics modeling were used to analyze the heat and mass transports inside the fuel cell. This developed system can be a basis for a good understanding of optimization for fuel cell design and operation mode.

5.1 Introduction

Fuel cells are an energy conversion device that directly converts chemical energy into electricity by electrochemical process. The proton exchange membrane fuel cells

(PEMFCs) that operate at significantly low temperatures are one of the most promising future power sources for their high efficiency and energy density among the fuel cell candidates [22, 33]. The PEMFCs are being developed as a sustainable alternative that have a variety of applications such as automotive and stationary power. It is well known that the current distribution in PEMFC is not uniform. This non-uniformity of current distribution in PEMFC can cause the loss of performance, the starvation process within a fuel cell, and the membrane degradation which leads to a reduced lifetime of the PEMFCs [105]. The water accumulation along flow-field can also cause the non-uniformity of current distribution [70, 78] and it is a major problem in maintaining high performance in the PEMFCs [106].

There are several methods of measuring current distribution in PEMFCs including the segmented electrode cell which is an invasive design construction. Current distribution measurement can be categorized into three major techniques: printed circuit board, resistors network, and Hall-effect sensors [19, 50-52]. These techniques require segmentation of one or both of the current collector and the bipolar plate component. The printed circuit board technology [53, 54] was introduced by Cleghorn et al. [53]. This technique uses a printed circuit board that is placed between the flow-field and the end plate for individual current collection. The resistors network technique [56] was introduced by Stumper et al. [51]. Basically, in the resistors network approach, either the anode or the cathode, or both sides are divided into the electrically isolated segments. These isolated segments are connected to the high resolution or shunt resistor network. The current from each segment can be calculated from the voltage drop across the resistor. The Hall-effect sensors technique [59-63] was introduced by Weiser et al. [55].

This technique uses a magnetic loop array connected to the segmented current collector plate to measure current distribution in a PEMFC [55]. The magnetic loop array is working as a current transducer to measure current from the magnetic field induction around the conductor. Beside experimental works, several authors used mathematical models to predict water, temperature, and current distribution in PEMFCs [64]. These efforts included those predictions of distribution profiles across the membrane [59, 65]. Model results have shown that local current distribution is dependent on local water and temperature profiles [59, 65].

Although numerous in-situ measurements of current distribution have been reported, those methods of current mapping may block the flow path, break diffusion media, and are usually very expensive. Therefore in this work, a cost-effective method of mapping the current distribution in a PEMFC was developed that will overcome many of the above limitations. This work aims to use the innovative measurement system [107] for the mapping of current distribution in the PEMFC as well as the understanding of water transport when the fuel cell is being operated.

There are many factors that affect the current distribution in PEMFC such as the difference in humidification temperature, gas flow rate, and gas flow arrangement. The bipolar plate design has a significant effect on overall PEMFC performance [70, 78]. They achieves the function of current collector, mechanical support for MEA, and provides access channel for the fuel and oxidant to PEMFC. The main challenge of current distribution mapping design is to attain the function of the bipolar plate which allows the reactant gases to access the MEA and also allow the current to be measured individually.

The purpose of this work is to establish a reliable and non-invasive method of measuring current distribution in a PEMFCs. To demonstrate the capability of our current distribution mapping design, computational fluid dynamic (CFD) predictions of local current density and transport variables were introduced and discussed along with the experimental data.

5.2 Current distribution measurement system

The novel developed current distribution measurement system consists of three main parts: Current distribution broad (CDB) device, Hall-effect sensor, and data acquisition. Figure 5.1 shows the simplified schematic of the measurement system. Current distribution board device, which was positioned within the fuel cell stack, was used for monitoring of the current density distribution.

5.2.1 Current distribution broad device

The fuel cell used for this current distribution experiment has an active area of 50 cm^2 made by Fuel Cell Technology, Inc. [83], which integrated triple serpentine flow fields on the anode side and quadruple serpentine flow fields on the cathode side. The current distribution was designed to work with this cell without disturbing the flow field.

To measure the current distribution, the CDB was designed and installed between the anode gas diffusion layers (GDL) and the anode flow-field plate as shown in Figure 5.2. Figure 5.2a presents the anode flow-field plate before installing the CDB and it shows flow direction from inlet to outlet. Figure 5.2b shows the anode flow-field after installing the CDB. This figure also presents how each segment is divided and numbered for further analysis. Figure 5.2c shows that the CDB can be simply made and installed to

any fuel cell hardware for a variety of detailed studies (e.g., transport, heat, and contamination studies). However, in this paper the 50-cm^2 serpentine flow-field hardware is the primary focus. Figure 5.3 shows the assembly of the fuel cell with the CDB. The CDB was placed with the conducting material facing the anode side. This current distribution was designed to have the cutout regions areas align with flow channel of the bipolar plate to avoid obstruction of gas during the fuel cell operation (see Figure 5.2b). The CDB is capable of measuring 10 individual areas. Each current collector segment has an area of 5 cm^2. Figure 5.4 shows the schematic of CDB components. This CDB consists of three layers: base, conductor, and insulation tape. A 50 μm Kapton® board was used as the base layer. The conductor consisting of copper bonded to the Kapton®. In order to prevent the corrosion during operational measurement, the copper segment was placed with the gold plate. Finally, 50 μm of Kapton® tape was used as an insulator to eliminate the conduction from material itself over the 10 individual current collection regions. Also, Kapton® tape insulates the copper conductor and maintains uniform thickness around the perimeter of the board to prevent leaks during operation.

Figure 5.5 shows the CDB adaptors, which are designed to have excellent contact between the board and the current-carrying wire. This figure also illustrates the direction of current during operation and the contact points that the current will travel. The first contact point occurs between the CDB and a lug. Each lug allows two points of measurement for each of the 10 regions such that of both current and voltage measurements. To provide a good corrosion resistance of these lugs, they were also coated with a gold flash completely coating the surface area. Therefore, the contact point

between the lug and the current-carrying wire resistance was small due to excellent contact between the lug and the wire.

5.2.2 Calibration of sensors

In order to verify the setup and the testing method, a mock test was used to collect the current distribution when using either a cut gas diffusion layer (GDL) or uncut GDL. This method was reported previously [107]. The purpose of this test is to examine the conductivity nature of the GDL by looking for a "smear "caused from current onto another section. The test was conducted where three amps of current were applied to the top of each segment via a DC power supply. Then, the current was measured from each segment; a significant amount of current was able to travel laterally through the GDL into nearby segments. Through experimentation, results were more accurate with individually segmented GDL. The GDL, AvCarb® EP40T, was segmented by cutting it into 10 pieces the same size as the current collector area of 5 cm^2. The 3-amp current was then applied to the electrode. The current was observed and recorded with the results showing a maximum of 0.9% error from the true applied current of 3-amp.

5.2.3 Hall-effect sensor and data acquisition.

The Hall-effect sensors were used to measure current for the CDB device. To monitor the current distribution in the fuel cell, the current was measured from individual segments separately by the Hall-effect sensors in the Hall-effect box as shown in Figure 5.6. The Hall-effect box consists of 10 Hall-effect sensors connected to the primary load box (Scribner Fuel Cell Test System 850e). This allowed the measuring of the current from ten individual segments in the CDB separately.

The data acquisition (DAQ) board was used to collect and monitor data during the experiment. This DAQ is able to measure 10 current inputs and also ten potential inputs simultaneously at 16 bits. The DAQ was connected to the computer and monitored by LabVIEW program. When running the experiment, the fuel cell was operated by controlling the potential, which was measured from "wire to load box" at Hall-effect sensors box shown in Figure 5.6.

5.3 Experimental Procedure

A PEMFC with an active area of 50 cm^2 was used in the study. The fuel cell assembly consists of an anode bipolar plate, current distribution board, 10 segmented anode GDLs (AvCarb® EP40T), membrane electrode assembly (MEA), un-segmented cathode GDL (AvCarb® EP40T), and a cathode bipolar plate as shown in Figure 5.3. The Gore^{TM} 57 Series MEA, with platinum loadings of 0.1 mg/cm^2 on the anode and 0.4 mg/cm^2 on the cathode, was used in the experiment. Table 5.1 summarizes the geometry details used in this experiment.

The current distribution was measured by using the CDB while the fuel cell was running at various humidity conditions to investigate the effect of humidification on the local performance. To define the humidity condition, the inlet gas dew point temperature was controlled by a fuel cell test station. The operating temperature was always set at 80˚C with the stoichiometry number of 1.5 at the anode and 2.0 at the cathode with co-flow configuration for all following experiments. The relative humidity condition of inlet gas was considered as the varying parameter. All of the experimental conditions are summarized in Table 5.2.

5.4 Model development

A computational continuum mechanics (CCM) technique based on a commercial flow solver, STAR-CD 4.16, was used to solve the coupled governing equations[76]. This software has an add-on tool called expert system of proton exchange membrane fuel cell (ES-PEMFC) version 2.50 that incorporates multi-physics of PEMFC. These require the source terms for species transport, multiphase flow, and heat generation equations [64, 71, 78]. This model has been validated with experimental data and the results were satisfied in both polarization data [71] and water balance data [64].

The PEMFC simulated in this work consisted of two flow-field patterns separated by GDLs and a MEA. The geometry details used in this simulation are also shown in Table 5.1. The operating conditions input into the model were consistent with experimental conditions given in Table 5.2. The number of computational cells used in the model is about one million cells. The predictions of current density distributions were compared with the experimental results taken from the CDB. The analysis of the results using both experimental and numerical information under various conditions was also discussed.

5.5 Results and discussion

Figure 5.7 shows the resistance chart of the fuel cell when the CDB was installed. The total excess of 6 mΩ was obtained, which comes from the wire, connection adapter and also CDB. Consequently, when taking this excess resistance into account, all corrected polarization curves approach the experimental results without the CDB as also shown in Figure 5.8. This figure shows the polarization curves of the PEM fuel cell with

and without CDB for different humidity conditions (a) Anode 25%RH, Cathode 25%RH, b) Anode 75%RH, Cathode 25%RH, and c) Anode 100%RH, Cathode 50%RH.). The overall performance of these three operating conditions reveals that the inlet humidity condition of 25%RH anode /25%RH cathode leads to the lowest performance. Then the performance of PEMFCs increases once the inlet humidity of the anode and/or the cathode is increased. In this particular experiment, the maximum performance is achieved when the anode inlet humidity is 100%RH and the cathode inlet humidity is 50%RH.

During fuel cell testing, the local current at 10 segments on CDB was recorded. Figure 5.9 shows the performance curve of each segment at different inlet humidity conditions similar to Figure 5.8. From these figures, the local polarization curves from segmented experiments can be presented in different profiles when the operating condition changes. For the dryer condition of 25%RH anode/25%RH cathode as shown in Figure 5.9a, the Segments 1 and 2 show the lowest local performance and the Segments 7 to10 display the highest local performance. Meanwhile when the operating condition was changed to higher relative humidity as presented in Figures 5.9b and 5.9c, the Segments 1 to 4 show the highest local performance and the Segment 10 presents the lowest local performance. Further discussion of these behaviors will be given in Figures 10 and 11.

Figure 5.10 shows the local current densities at ten segments at different humidity conditions compared with numerical predictions. Note that the flow direction and the flow-field corresponding to each segment on CDB can be found in Figure 5.2. Figure 5.10a represents the current densities at 25% RH on both the cathode and anode. The cell potential was set at 0.3V with a cell temperature of 80˚C. The maximum current density

is observed at the outlet regions where Segments 7 to 10 are located. This experimental result is consistent with the model prediction as also shown in this figure. In this particular operating condition where the dryer inlet humidity was introduced into both anode and cathode, the water back diffusion from the cathode to the anode shows strong contribution, thus resulting in higher membrane water content and increasing the local performance toward the exit. Figure 5.11 shows the distributions of numerical prediction of total water flux across the membrane. There are positive and negative values indicating the direction of the flux. The positive value indicates that the water transports from the anode to the cathode and the negative number denotes water back diffusion, where the direction of water transport is from the cathode to the anode. Figure 5.11a supports the explanation given in Figure 5.10a that water back diffusion is presented in this condition. Therefore, the local current density increases from the inlet toward the outlet due to increasing membrane conductivity.

When the inlet humidity at the anode was increased to 75%RH while keeping the cathode inlet humidity constant at 25% RH, the current distribution pattern in Figure 5.10b is completely different from the profile shown in Figure 5.10a. The overall average current density is increased to 1.09 A/cm^2 at the cell potential of 0.3V. The highest current density is presented at locations 1 to 4, where the anode inlet is located. Then the local current density is decreasing toward the outlet. The prediction also agrees well with experimental data in this particular study. By increasing the inlet humidity at the anode, the membrane water content and proton conductivity are also increased thus enhancing overall performance. When the membrane is well humidified, the local current density distribution decreases from the inlet to the outlet by following the consumption of

hydrogen and oxygen in this co-current flow direction. Moreover, the water transport across the membrane follows the direction from the anode to the cathode due to the strong contribution of electro-osmotic flux rather than water back diffusion flux as shown in Figure 5.11b. This figure presents the net water flux across the membrane from the anode to the cathode as provided in the positive number. This value is decreased from the inlet toward the outlet as the current density is decreasing thus lowering the electro-osmotic flux.

The local current density profile shown in Figure 5.10c is similar to Figure 5.10b. A similar trend is observed for the net water flux distributions shown in Figure 5.11c and Figure 5.11b, where the highest value is at the inlet region and the lowest value is located around the exit region. In Figure 5.10c, the average current density in this condition is higher (i.e., 1.25 A/cm^2) than the value shown in Figure 5.10b. This is because the inlet humidity condition in Figure 5.10c was increased to 100%RH at the anode and 50%RH at the cathode. Again, increasing humidity inside the PEMFC will enhance proton conductivity of the membrane thus increasing the overall performance. The numerical prediction agrees with the experimental results. When the local current density increases due to higher membrane water content, the net water flux from the anode to the cathode is also increased as shown in Figure 5.11c.

5.6 Conclusions

The current distribution was measured by using the CDB that can be placed inside a fuel cell with minimal obstruction and resistance. The CDB performance was verified using resistance collection. This technique was most consistent and matches the model

prediction. The current distributions at various relative humidity conditions show different behaviors. The higher RH indicates higher overall current densities due to the lower membrane resistance. For high RH, the results also indicated the maximum current density at the inlet regions and lower current density towards the outlet regions of the cell. On the other hand, for low RH, the result shows the lowest current density at the inlet regions and higher current density towards the outlet regions of the cell. CFD predictions agree with the experimental data. Consequently, the electrochemical variables from the model results can be used for further analysis. The novel technique of measuring the current density distribution using CDB sheet can be applied to any type of fuel cell hardware and with less effort.

Table 5.1 Geometry details

Description	Value
Active area	50 cm^2
Channel width	0.8 mm
Channel height	0.5 mm
Rib-spacing width	0.8 mm
GDL thickness	200 μm
MEA thickness	25 μm

Table 5.2. Experimental condition

T_{cell} (°C)	Anode RH (%)	Cathode RH (%)	Stoichiometry		Back pressure (PSIG)
			Anode	Cathode	
	25	25			0
80	75	25	1.5	2.0	0
	100	50			5

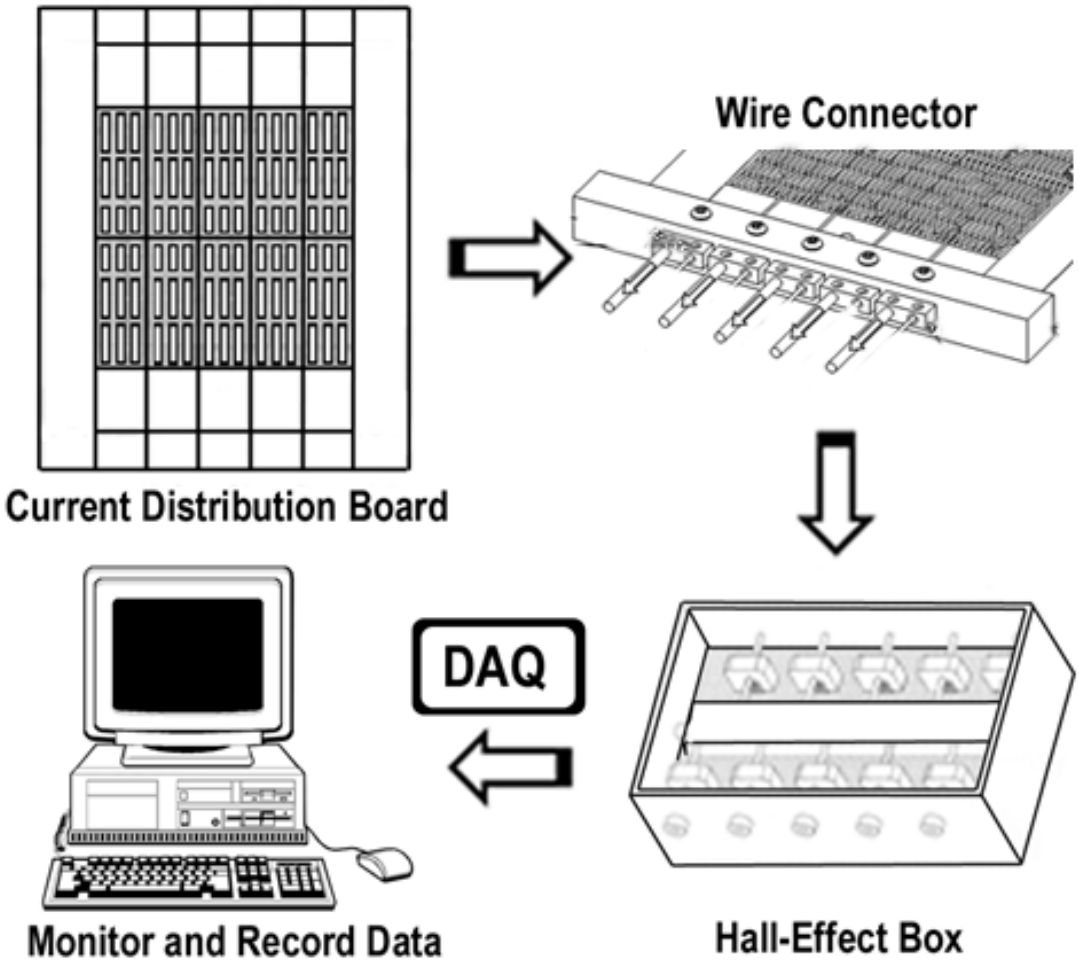

Figure 5.1. Illustration of the hardware and software components of the system.

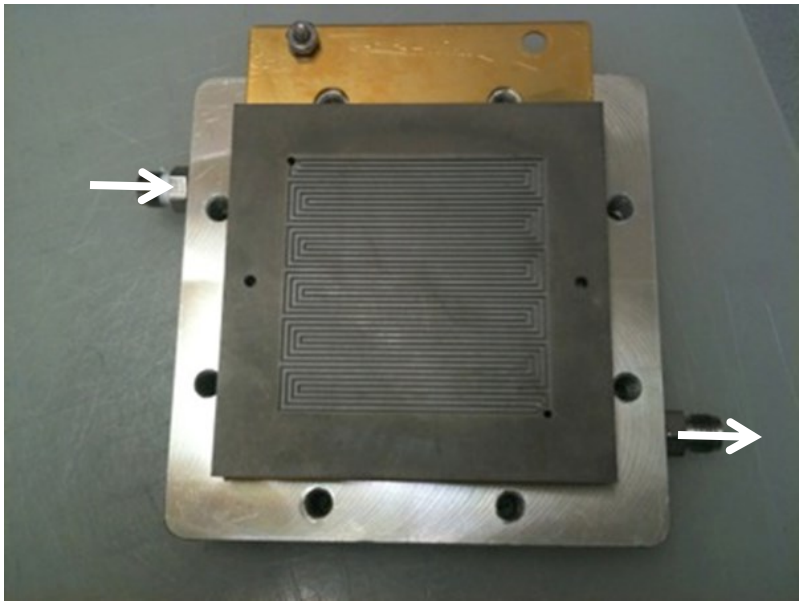

a) Anode flow-filed plate

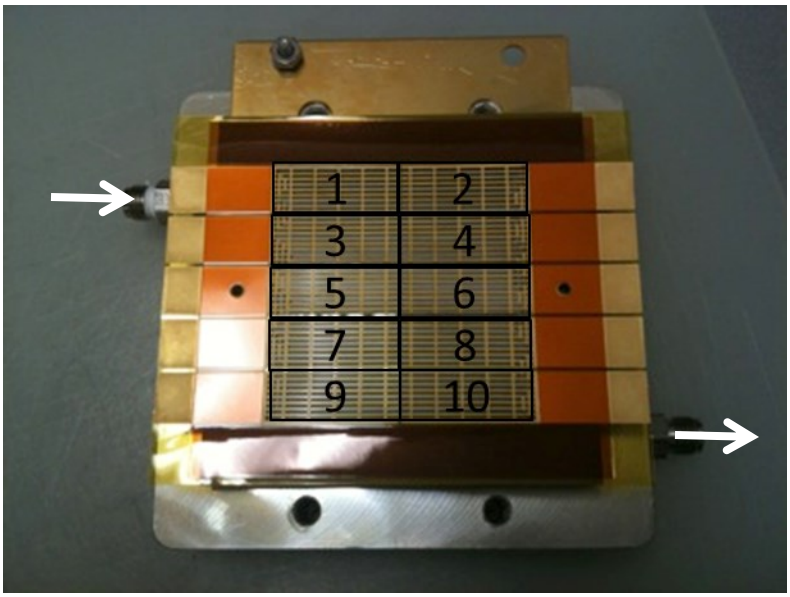

b) CDB on anode flow-field

Figure 5.2. A photograph of the fuel cell bipolar plate a) 50-cm^2 anode serpentine flow field plate, b) alignment current distribution board on 50-cm^2 anode serpentine flow field plate, and c) CDB with different hardware

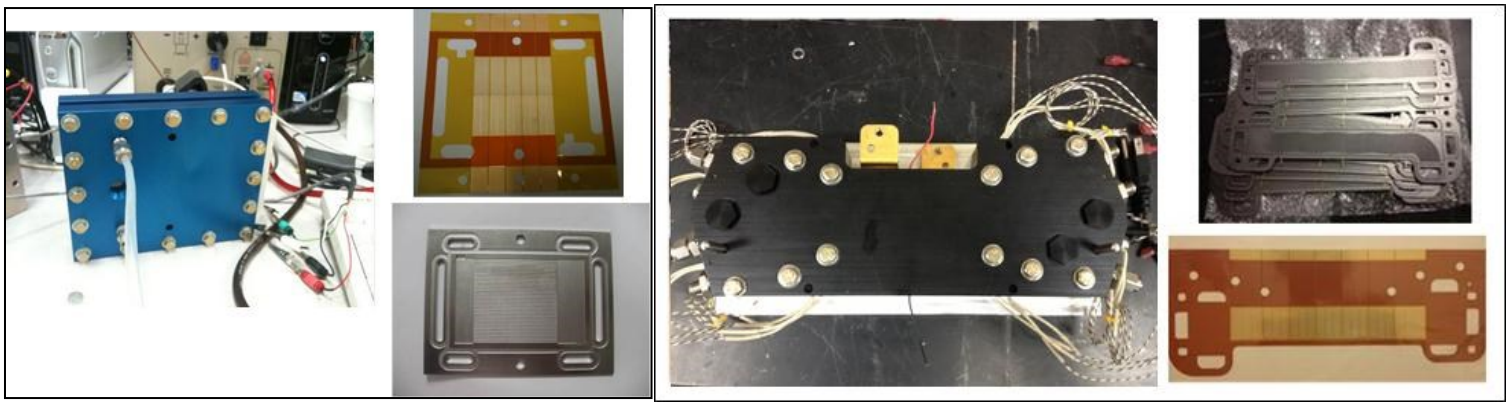

c) Fuel cell hardware

Figure 5.2. A photograph of the fuel cell bipolar plate a) 50-cm^2 anode serpentine flow field plate, b) alignment current distribution board on 50-cm^2 anode serpentine flow field plate, and c) CDB with different hardware

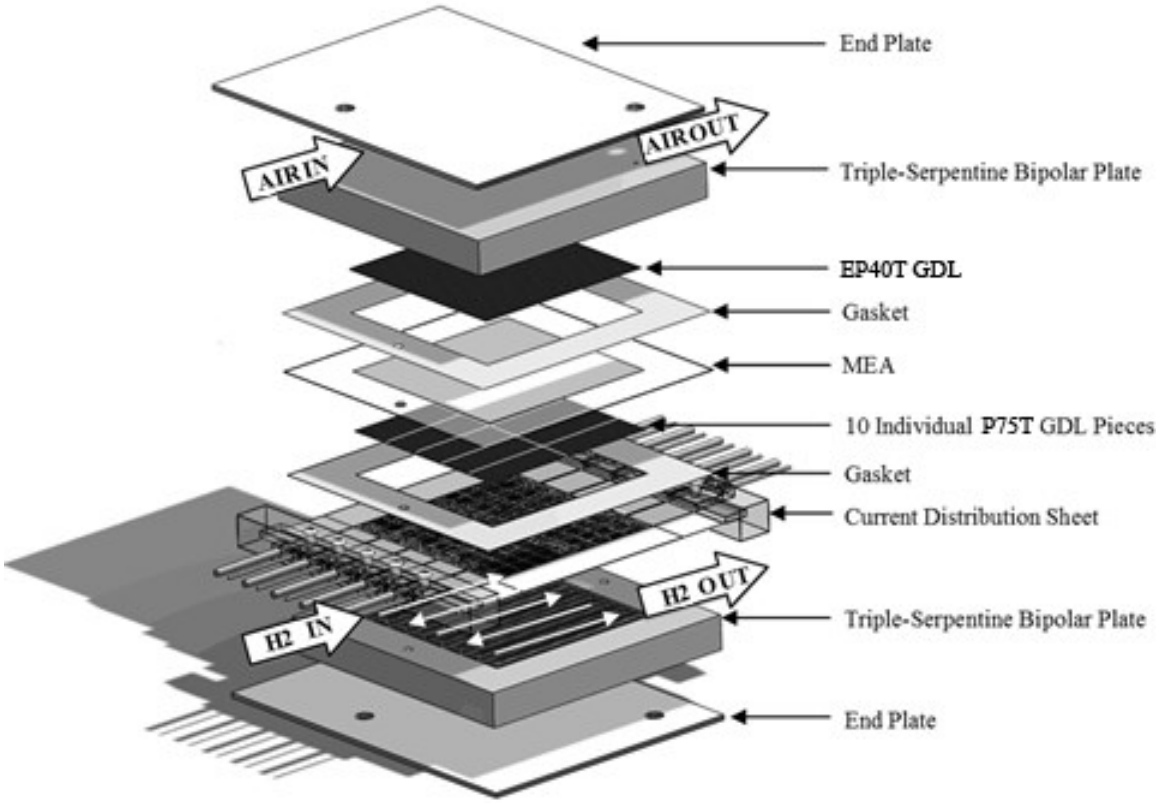

Figure 5.3. Assembly of fuel cell with Current Distribution Board in place.

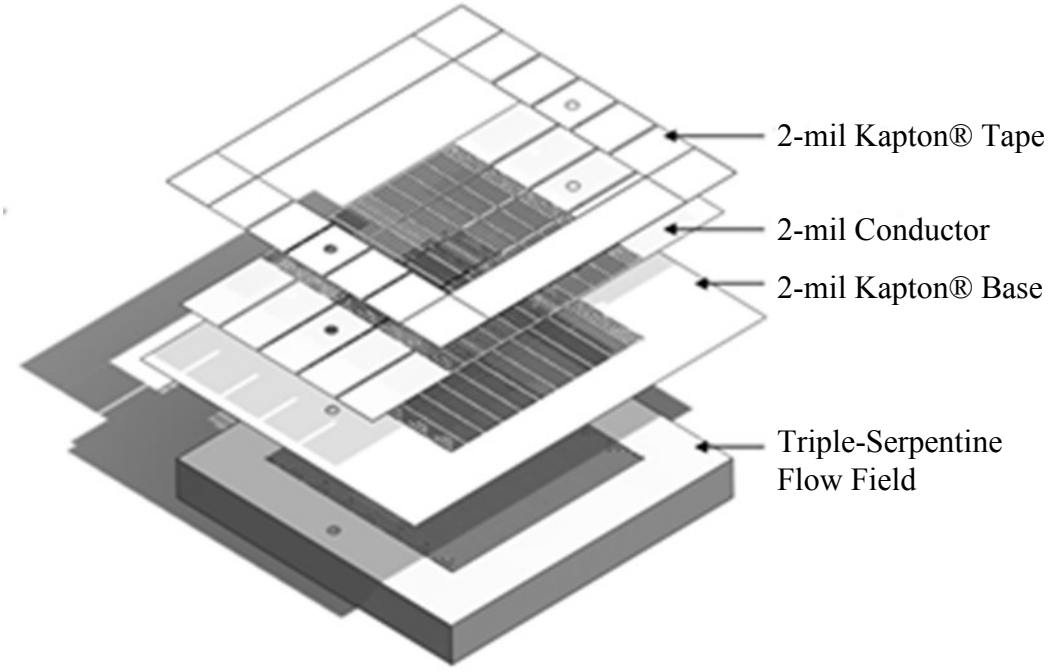

Figure 5.4. The current distribution board component; consist of the 2-mil Kapton® tape, 2-mil conductor, and 2-mil Kapton® base.

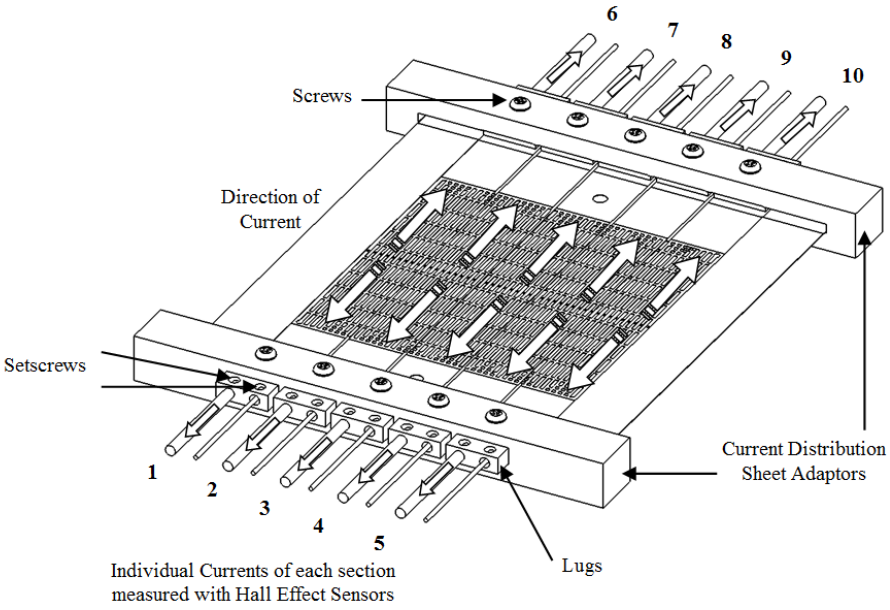

Figure 5.5. Current distribution board with attached adaptors

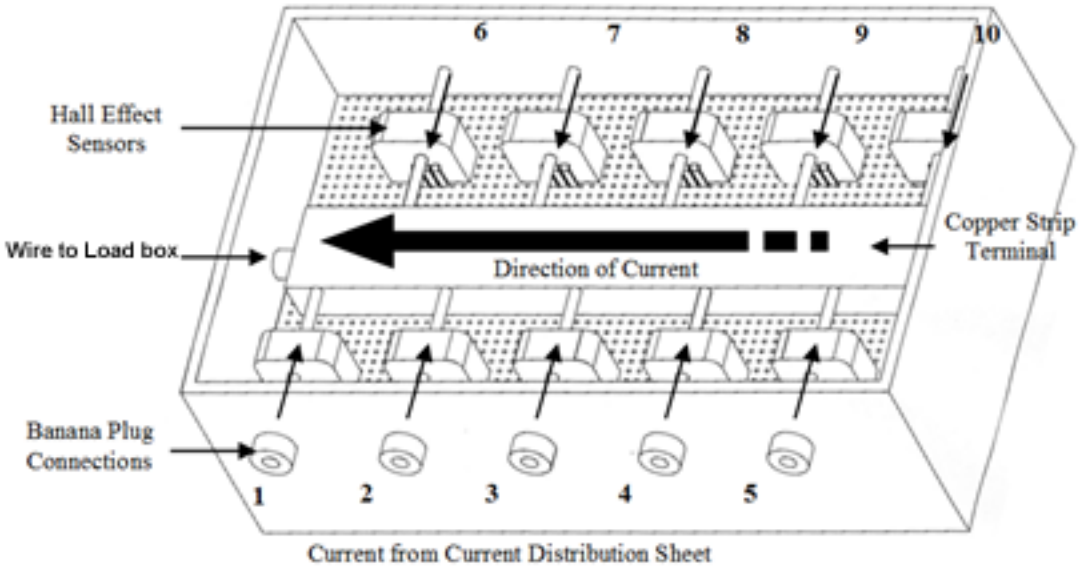

Figure 5.6. The 10 individual collected currents pass through Hall-Effect sensors.

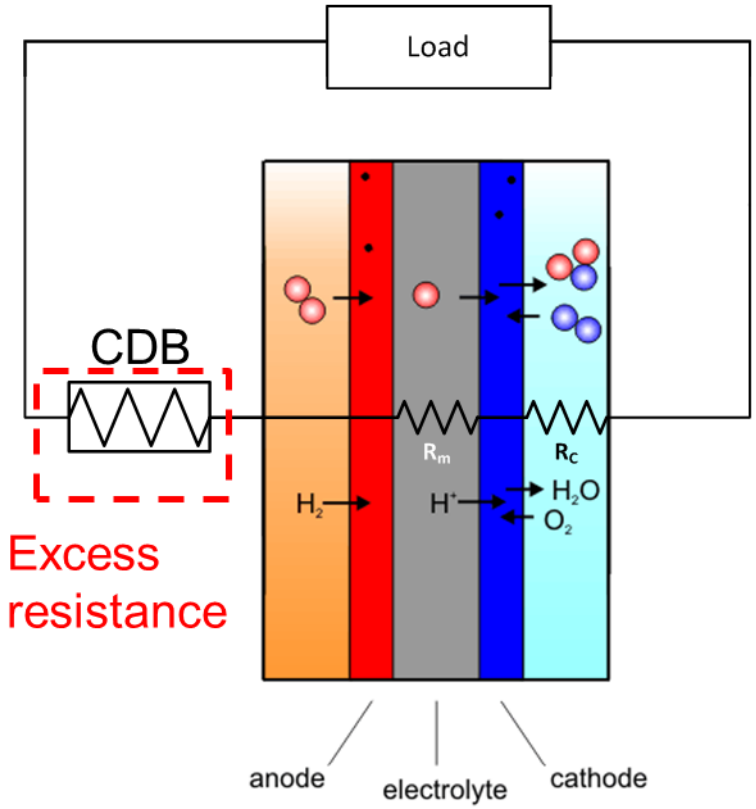

Figure 5.7. Schematic of the resistance chart in fuel cell operate with current distribution board.

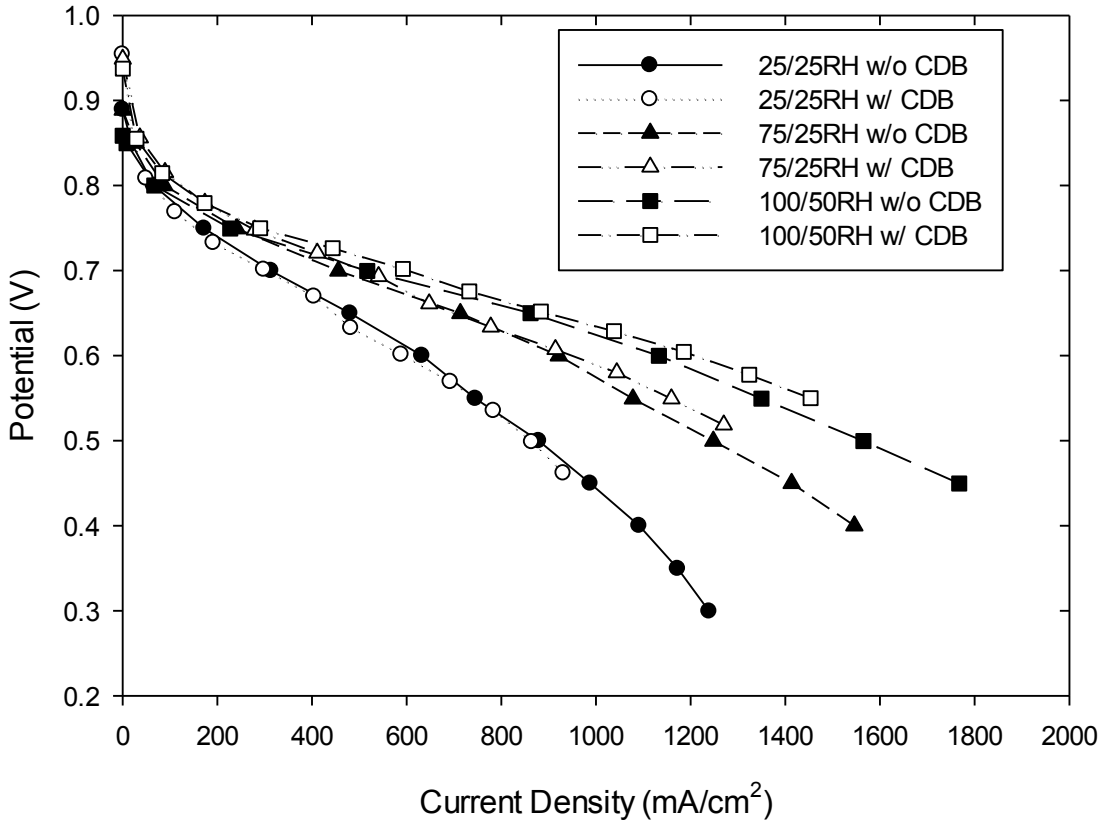

Figure 5.8. Polarization curve of PEMFC with CDB device on different operating condition compare to correction data.

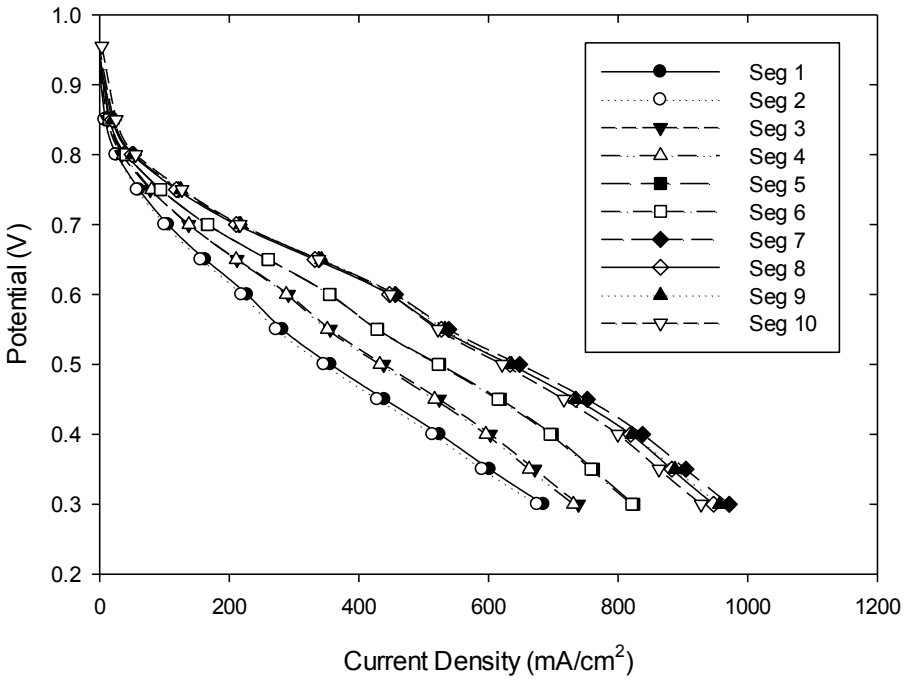

a) Anode 25%RH, Cathode 25%RH

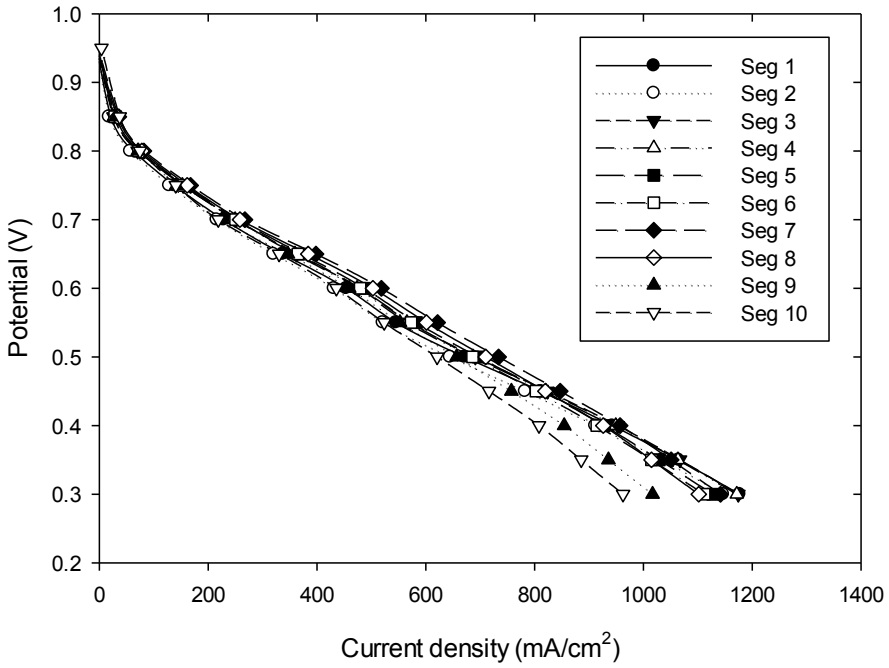

b) Anode 75%RH, Cathode 25%RH

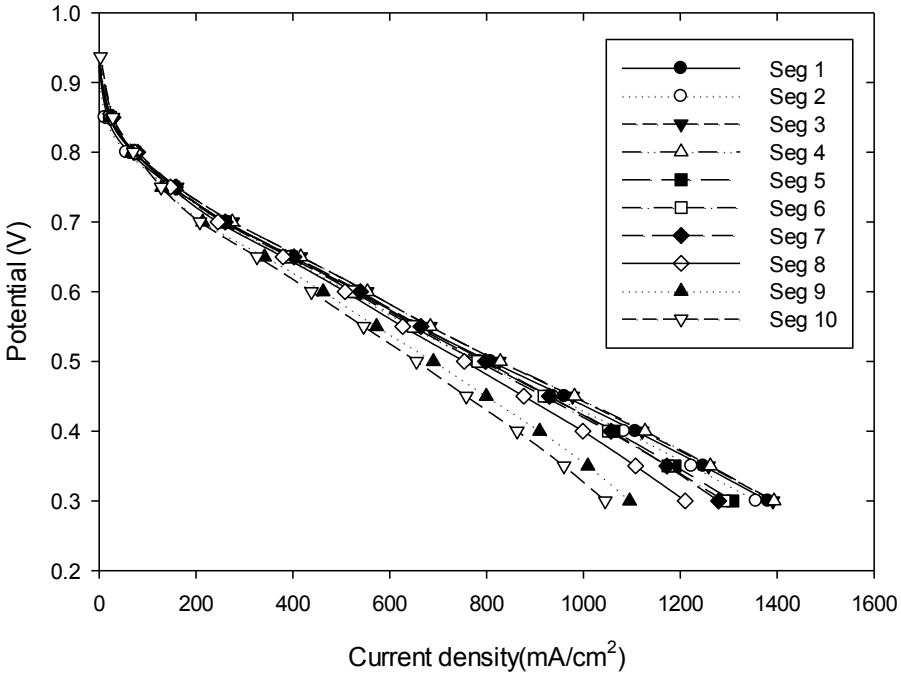

c) Anode 100%RH, Cathode 50%RH

Figure 5.9. Polarization curves of each segment under different humidity conditions: a) Anode 25%RH, Cathode 25%RH, b) Anode 75%RH, Cathode 25%RH, and c) Anode 100%RH, Cathode 50%RH.

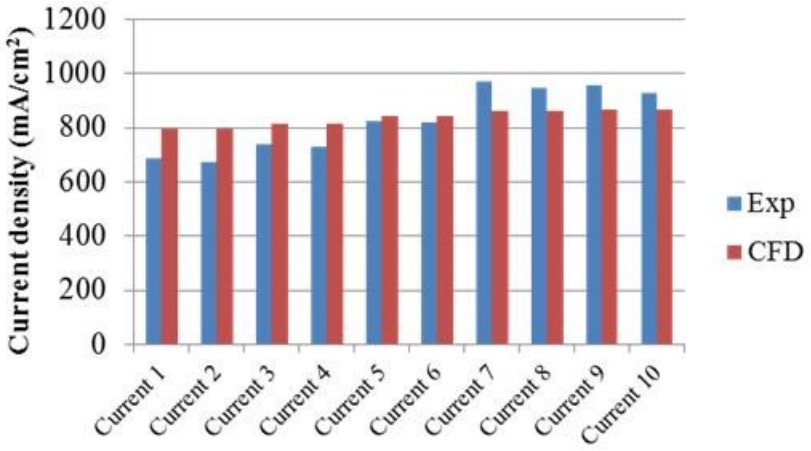

a) I_{avg} = 809 mA/cm^2: Anode 25%RH, Cathode 25%RH

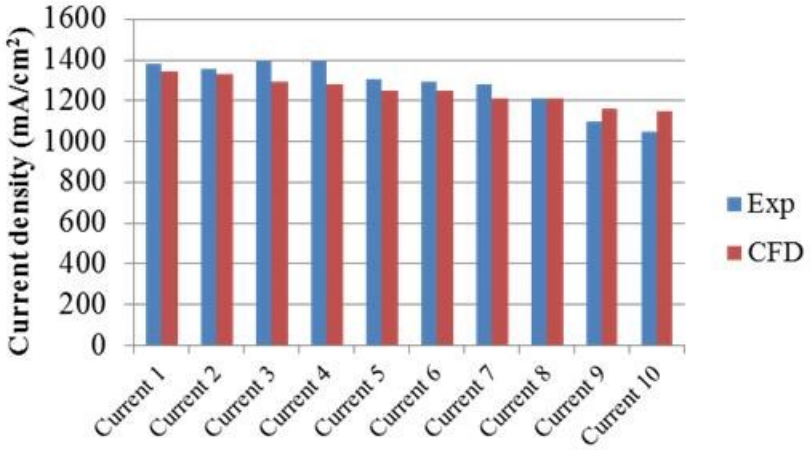

b) I_{avg} = 1094mA/cm^2: Anode 75%RH, Cathode 25%RH

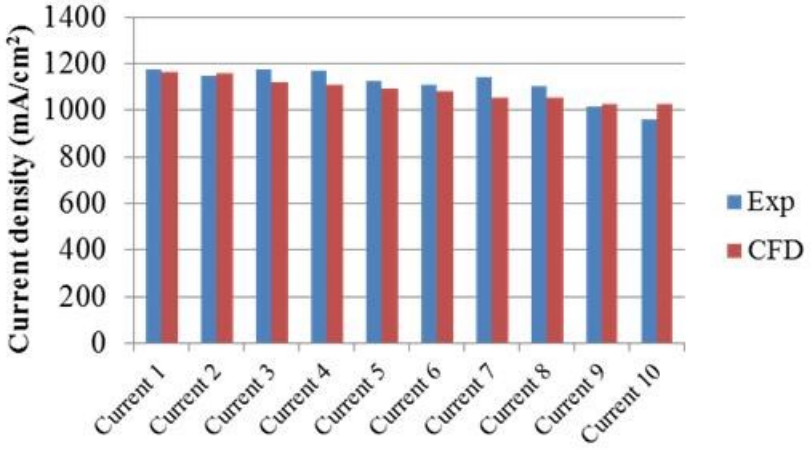

c) I_{avg} = 1250 mA/cm^2: Anode 100%RH, Cathode 50%RH

Figure 5.10. Current density distributions of the three different inlet humidity conditions at potential 0.3V; a) Anode 25%RH, Cathode 25%RH, b) Anode 75%RH, Cathode 25%RH, and c) Anode 100%RH, Cathode 50%RH.

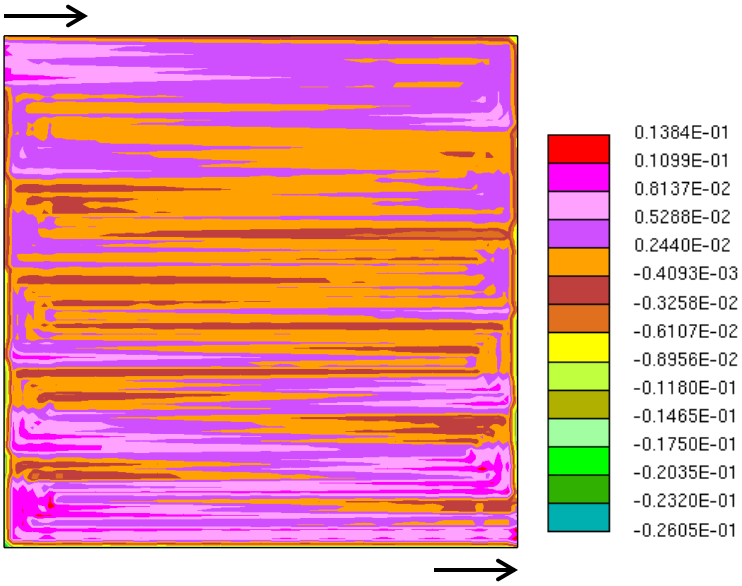

a) Anode 25%RH, Cathode 25%RH

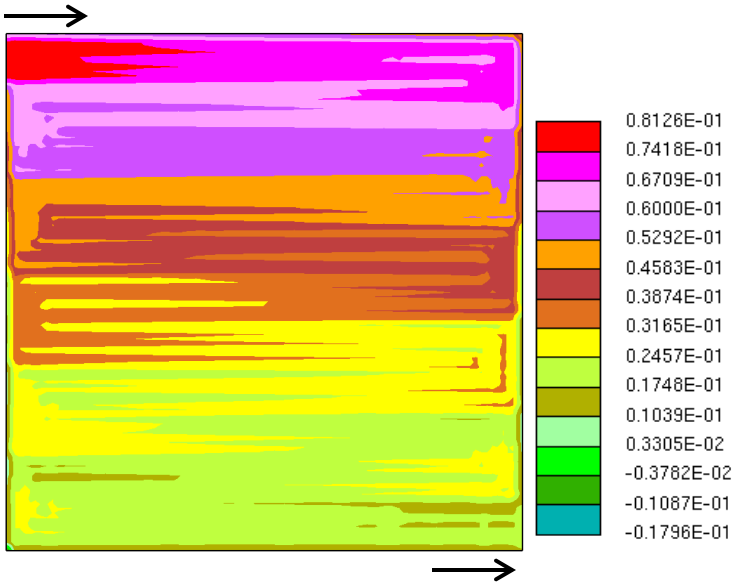

b) Anode 75%RH, Cathode 25%RH

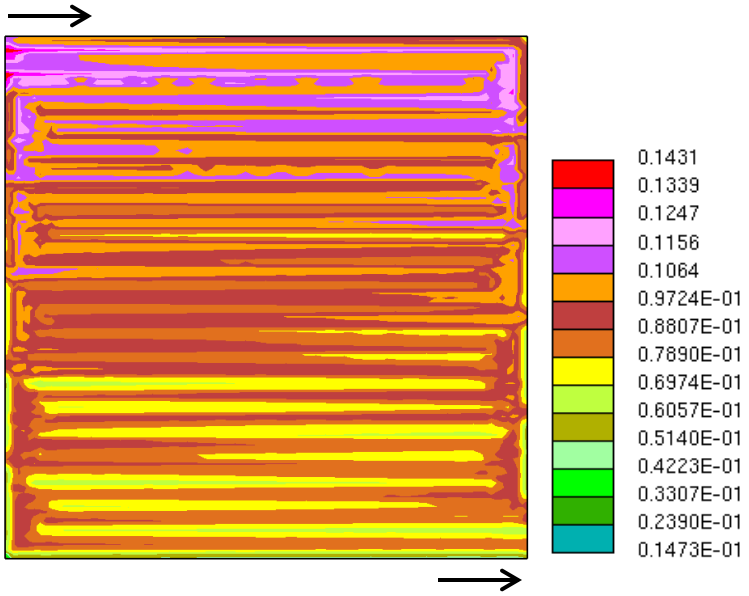

c) Anode 100%RH, Cathode 50%RH

Figure 5.11. Net water flux across the membrane (mg/cm^2-s) of three different inlet humidity conditions at potential of 0.3V. a) Anode 25%RH, Cathode 25%RH, b) Anode 75%RH, Cathode 25%RH, and c) Anode 100%RH, Cathode 50%RH.

CHAPTER 6

THE EFFECT OF MEMBRANE PROPERTIES ON WATER TRANSPORT IN PEMFCS

The effect of water transport of two type of membrane material, Nafion® (NRE 211) and biphenyl sulfone hydrocarbon (6FK-BPSH100), was studied. These two different membrane type was characterized their properties. These membrane materials also were used to fabricate membrane electrode assembly (MEA) and were then tested in the fuel cell system. The experiments were done at different relative humidity (RH) to study the effect of water on the cell performance. Furthermore, the characterized membrane was used in the mathematical modeling. These modeling results were used to have better understanding in water transport in proton exchange membrane fuel cells (PEMFCs).

6.1 Introduction

PEMFCs are the most promising candidate for automotive power source. The proton exchange membrane is one of the most important components in fuel cell system. At present, the challenge of produce low cost PEMFC system is the most concerned for the fuel cell manufacture. Reducing membrane cost is a key for low cost PEMFC system.

The perfluorinated sulfonated copolymer, Nafion® [108], membrane manufactured by Dupont generally is the most common used as membrane for PEMFCs.

A Nafion® membrane exhibits good thermal and chemical stability, and also has. high proton conductivity under hydrated state[109]. However, the most importantly limitations to commercial use is membrane cost. The challenge is to produce a cheaper material for PEMFC membrane that can satisfy the thermal and chemical stability, and high conductivity.

Presently, one of the most promising candidates is the use of hydrocarbon polymer for polymer backbones [4]. The alternative material poly(arylene ether ketone sulfone) [4] multiblock copolymer, 6FK-BPSH100, developed by McGrath's research group in Virginia Tech [110, 111] was used to study in this work. Figure 6.1 shows the chemical structure of 6FK-BPSH100. These aromatic ionomers copolymer has many advantages such as improved mechanical properties and chemical stability [112].

The two different membrane materials were casted and made to MEA for testing. These two membranes were characterized, and they show different properties which effect water transport of PEMFCs. The Water distribution is also a function of current distribution in PEMFCs. Current distribution behaviors are studied in the different operating condition of fuel cell such as humidity and different membrane material. This experiment was setup to understand water transport at different operating condition of membrane material.

6.2 Experimental setup

6.2.1 Membrane preparation

Generally, Nafion® (NRE211) membrane manufactured by Dupont was used as the benchmark membrane. The alternative material poly(arylene ether ketone sulfone) [3]

multiblock copolymer, 6FK-BPSH100, developed and prepared by McGrath group [4,5] was used to compare with Nafion®. The solutions of 6FK-BPSH100 were prepared at Virginia Tech and sent to Giner Electrochemical Systems, LLC which they cast into the membrane. This hydrocarbon membrane has a thickness a 27 μm. The two different membrane materials were completed into MEA.

6.2.2 Membrane characterization

The membrane characterizations, membrane water content, water diffusivity, electro-osmotic drag coefficient (EODC), and proton conductivity were performed at Giner Electrochemical Systems, LLC Newton, MA 02466.

Membrane water content was measured as a function of relative humidity (RH). Definition of Water content, λ, is given as the ratio of the number of water molecules to the number of charge sites, SO_3 [59]. Figure 6.2 (a) shows the comparison result of membrane water content isotherm measurement between Nafion® (NRE) and hydrocarbon (VT) membrane. Both of these membrane material shows similarly result, the membrane water content increase with RH value.

Water diffusivity was measured as a function of membrane water content. The water diffusivity is a factor of water flux to the gradient from chemical property. Figure 6.2 (b) shows the comparison result of water diffusivity measurement between Nafion® (NRE) and hydrocarbon (VT) membrane. The NRE211 has higher water diffusivity compare to VT membrane.

Electro-osmotic drag coefficient (EODC) was also measured as a function of membrane water content. The EODC is defined as the number of water molecules moving with each proton, which the conducting protons draw water in their motion

across the membrane. In fuel cells, there is a serious problem of drying of the hydrogen electrode and the part of the membrane due to the electro-osmotic effect [113]. The membrane characterization results show that NRE211 presents higher EODC value compare to VT membrane as shown in figure 6.2 (c).

Proton conductivity, σ, was measured as a function of RH. The proton conductivity is one of the most important properties for membrane in PEMFCs. For high performance PEMFCs, the membrane should have high proton conductivity more than 10^{-2} S cm^{-1}. The conductivity of NRE211 can reach value of 10^{-2} – 10^{-1} S cm^{-1} and it shows higher value compare to hydrocarbon membrane at low RH range. However, when increasing RH value, the hydrocarbon membrane trend to have slight better proton conductivity that NRE211.

6.2.3 Experiment procedure

Giner Electrochemical Systems, LLC fabricated the two different MEAs by using the two different membrane materials, Nafion® (NRE211) and hydrocarbon membrane from Virginia Tech. These both type of MEA have the same Pt loadings of 0.1 mg/cm^2 on the anode and 0.4 mg/cm^2 on the cathode. The MEA was assembled into a fuel cell hardware made by fuel cell technology. Carbon paper, AVCarb® EP40T, with Wet-proofed treatment with 200 μm thickness was used as GDL. The operating temperature was always set at 80˚C with the stoichiometry number of 1.5 at the anode and 2.0 at the cathode with co-flow configuration for all following experiments.

The fuel cell was running at various humidity conditions to investigate the effect of humidification on the overall performance. The humidity condition of the inlet gas was controlled by a fuel cell test station (Scribner Fuel Cell Test System 850e) which

adjusting dew point temperature of inlet gas. The relative humidity (RH) condition of inlet gas was considered as the varying parameter. All of the experimental conditions are summarized in Table 6.2.

The water balance experiment was performed to acquire the overall water transport across the membrane. The water coming out of the fuel cell will be trapped and weighted. The overall water transport can be calculated by knowing amount of water coming into fuel cell and coming out from fuel cell. Figure 6.3 shows the diagram of water balance experiment setup.

6.2.4 Model development

A computational continuum mechanics (CCM) technique based on a commercial flow solver, STAR-CD 4.16, with add-on tool ES-PEMFC) version 2.50 was used to solve mathematical model. The results of membrane characterization were used to deliver new parameter for the modeling equation. These two different membrane parameter models have been validated with experimental data and the results were satisfied in both polarization and water balance data.

6.3 Results and Discussions

6.3.1 Performance

Figure 6.4 shows polarization curves for the two different RH inlet gas condition. Figure 6.4 a) illustrates the result of 50 % RH for both inlet anode and cathode gas and Figure 6.4b) presents the result of 95% RH for both inlet gas. Figure 6.4 a) and b) show different tendencies for the polarization curves. For the low RH case (50%RH), the Nafion® membrane shows better performance compare to hydrocarbon (VT) membrane.

While the high RH case (95% RH), the hydrocarbon (VT) membrane appear to have better performance. This results should be pointing out that water in the fuel cell affect the overall performance thus, at high RH condition Nafion® membrane is more suffering from the water flooding. Even though, the hydrocarbon membrane has higher proton conductivity at high RH. This is just slightly better thus, it shouldn't cause big different in term of performance.

From the membrane properties, Nafion® membrane shows higher EODC and diffusivity that hydrocarbon membrane thus; Nafion® membrane should have more water transport from anode to cathode than hydrocarbon membrane with this parameter. Therefore, water transport is a major factor of the fuel cell performance.

6.3.2 Water transport

For further investigate of water transport, the water balance experiment was accomplished to obtain overall water transport information from fuel cell. Table 6.2 shows comparison of water balance results between Nafion® and hydrocarbon (VT) membrane. This result also shows that for the same operating condition the Nafion® membrane has more water transport to the cathode side. This result shows that the amount of water transport across Nafion® membrane is about twice amount of water transport across hydrocarbon (VT) membrane as shown in Figure 6.5. These confirm that the falling of Nafion® membrane performance comes from water flooding in cathode flow channel.

6.3.3 Modeling

In order to understand the effect of water transport, the mathematical modeling with computational fluid dynamic (CFD), was used to perform the fuel cell operation. From the membrane characterization results, these can be used in the modeling parameter. The modeling result of polarization curves of Nafion® and hydrocarbon membrane were also shown in Figure 6.4. With the new parameter from hydrocarbon membrane, the results of CFD are consistence with the experimental polarization curve data. These CFD results also have been confirmed with the water balance data as shown in table 6.3. The Table 6.3 presents water balance experimental data on different operating condition compare to CFD data.

The major reason for the performance decrease for Nafion® membrane, the liquid water flooding, is the ability of dragging water from anode to cathode flow channel. Figure 6.6 shows the CFD prediction comparison of local water flux distribution from anode to cathode at 95% RH for both cathode and anode gas inlet comparison between Nafion® and hydrocarbon membrane. The results illustrate the highest water flux occurs at the entrance of the flow channel and then it decreases toward outlet of the fuel cell. This is because the water flux distribution is function of EODC which follow current distribution in fuel cell. At high RH, the current distribution shows the highest value at the entrance and then decrease toward due to the reaction rate from partial pressure of fuel and oxidizer. Furthermore in this study, Figure 6.6 illustrates the liquid water distribution in cathode MEA/GDL interfacial comparison between Nafion® and hydrocarbon membrane. These results show that Nafion® membrane has liquid water present at the beginning of flow channel and more toward the outlet while hydrocarbon

membrane start to have liquid water almost in the middle of the cell. Therefore the Nafion® membrane will suffer more from liquid flooding effect.

6.4 Conclusions

In this chapter, the performance and overall water of PEMFC with two different membrane materials were determined. These two membrane material have been characterized in them of membrane water content, water diffusivity, EODC, and proton conductivity. These properties were used as mathematical parameter for CFD analysis. CFD results were reported on performance, water transport, and local water distribution. The CFD data were verified by experimental polarization curves and overall water balance. CFD predictions agree well with the experimental data.

The effect of membrane properties shows the most impact to PEMFC performance and water transport in the fuel cell. For higher RH, the hydrocarbon membrane performance is better because slightly better proton conductivity and mostly lower EODC value. These low EODC give the lower water transport across from anode to cathode, thus hydrocarbon membrane prevent water flooding at RH condition better than Nafion® membrane.

Table 6.1. Experimental condition

T_{cell} (°C)	Anode RH (%)	Cathode RH (%)	Stoichiometry		Back pressure (PSIG)
			Anode	Cathode	
	75	25			0
80	50	50	1.5	2.0	0
	95	95			0

Table 6.2. Comparison of water balance between Nafion® and Hydrocarbon (VT) membrane.

	i A/cm^2	%RH	Anode Water Balance (mg/sec)			Cathode Water Balance (mg/sec)			
			Water in	Water out	Cross to Cathode	Water in	Gen.	Water out	Cross from Anode
NRE	**0.4**	95	1.10	0.65	0.46	3.51	0.93	4.91	0.47
VT	**0.4**	95	1.10	0.86	0.25	3.51	0.93	4.66	0.22
NRE	**0.6**	95	1.66	0.96	0.69	5.26	1.40	7.36	0.70
VT	**0.6**	95	1.66	1.29	0.37	5.26	1.40	7.04	0.38
NRE	**0.8**	95	2.21	1.35	0.86	7.03	1.87	9.80	0.86
VT	**0.8**	95	2.21	1.68	0.53	7.03	1.87	9.44	0.54

Table 6.3. The water balance Hydrocarbon (VT) membrane at different operating condition.

	i A/cm^2	RH	Anode Water Balance (mg/sec)			Cathode Water Balance (mg/sec)				error (%)
			Water in	Water out	Cross to Cathode	Water in	Gen.	Water out	Cross from Anode	
EXP	**0.4**	75/25	0.75	0.22	0.53	0.59	0.93	2.01	0.49	7.5
CFD	**0.4**	75/25	0.75	0.23	0.52	0.59	0.93	2.03	0.51	2.0
EXP	**0.4**	50/50	0.42	0.29	0.13	1.35	0.93	2.42	0.14	7.1
CFD	**0.4**	50/50	0.42	0.29	0.13	1.35	0.93	2.40	0.12	8.3
EXP	**0.4**	95/95	1.10	0.86	0.25	3.51	0.93	4.73	0.29	13.7
CFD	**0.4**	95/95	1.10	0.90	0.20	3.51	0.93	4.66	0.22	9.0
EXP	**0.6**	75/25	1.12	0.33	0.79	0.88	1.40	3.09	0.81	2.5
CFD	**0.6**	75/25	1.12	0.31	0.81	0.88	1.40	3.13	0.85	4.7
EXP	**0.8**	50/50	0.85	0.55	0.30	2.70	1.87	4.88	0.31	3.2
CFD	**0.8**	50/50	0.85	0.58	0.27	2.70	1.87	4.85	0.28	3.5
EXP	**0.8**	95/95	2.21	1.68	0.53	7.03	1.87	9.44	0.54	1.8
CFD	**0.8**	95/95	2.21	1.66	0.55	7.03	1.87	9.45	0.55	0.0
EXP	**1.2**	95/95	3.32	1.99	1.34	10.55	2.80	14.60	1.25	7.5
CFD	**1.2**	95/95	3.32	2.01	1.31	10.55	2.80	14.72	1.37	4.4

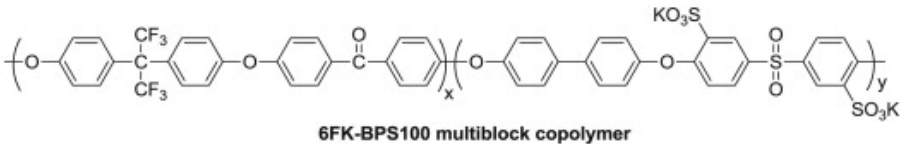

Figure 6.1. Chemical structure of 6FK-BPSH1001 [109]

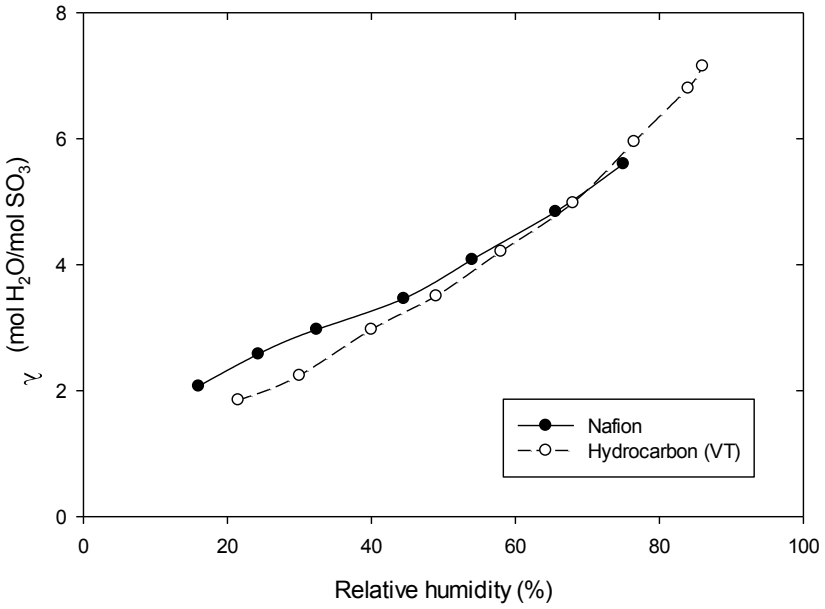

a)

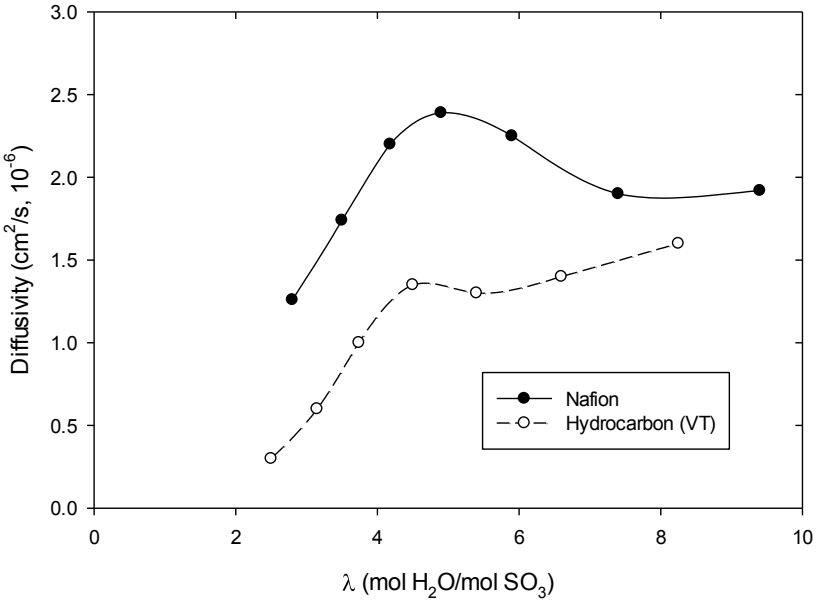

b)

Figure 6.2. Comparison of membrane properties between Nafion® (NRE211) and hydrocarbon (VT) membrane.

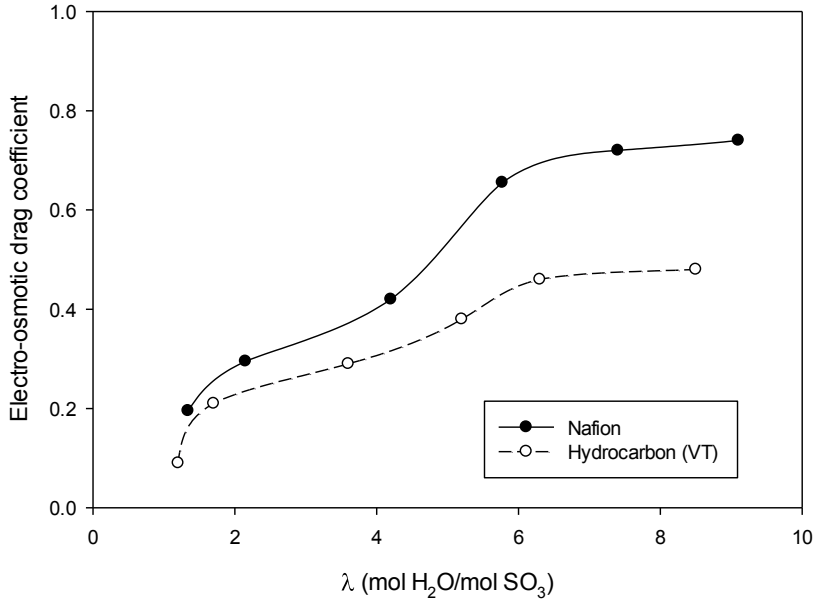

c)

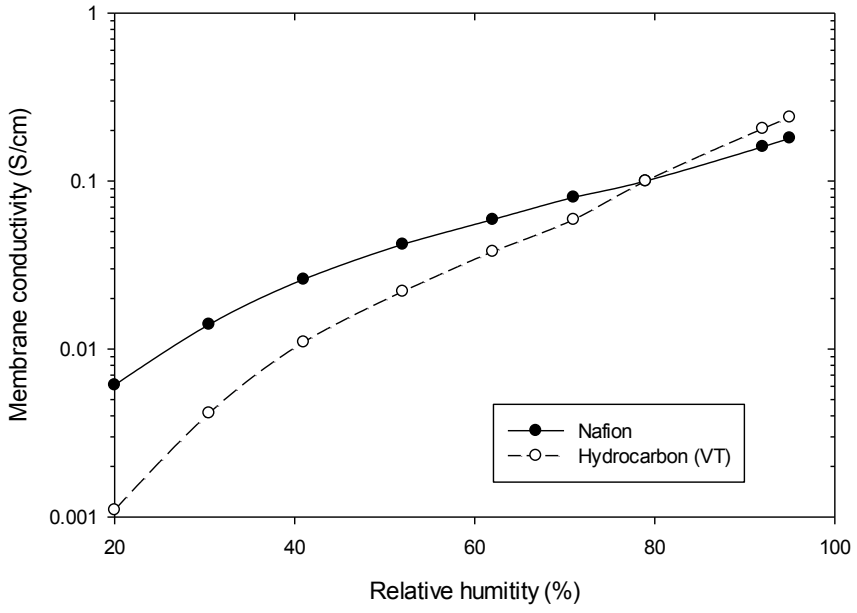

d)

Figure 6.2. Comparison of membrane properties between Nafion® (NRE211) and hydrocarbon (VT) membrane.

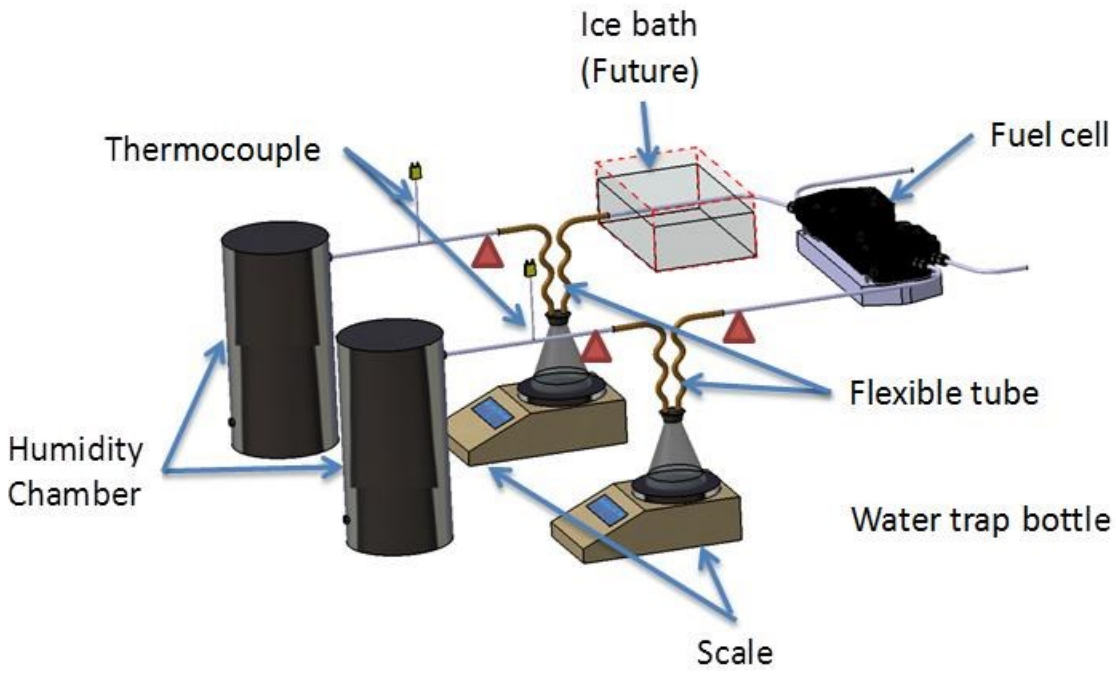

Figure 6.3 Water balance experimental setup.

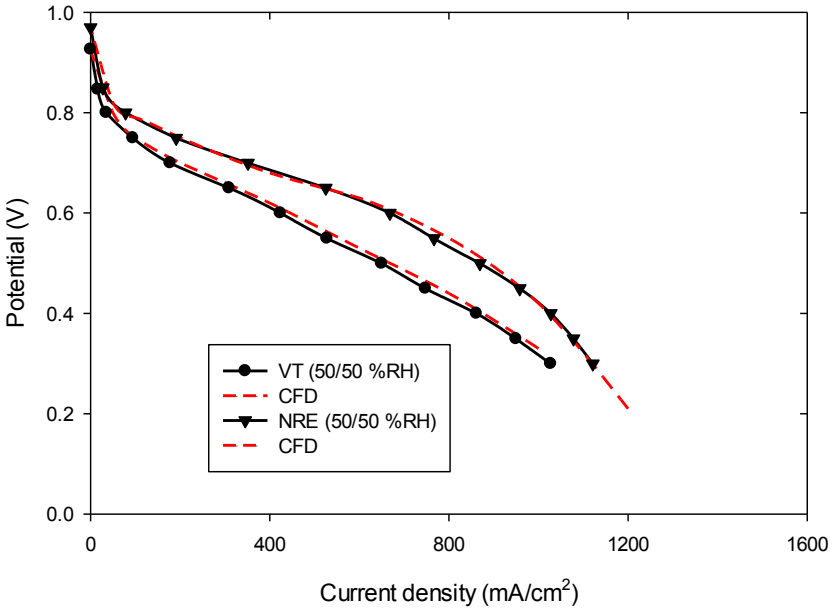

a)

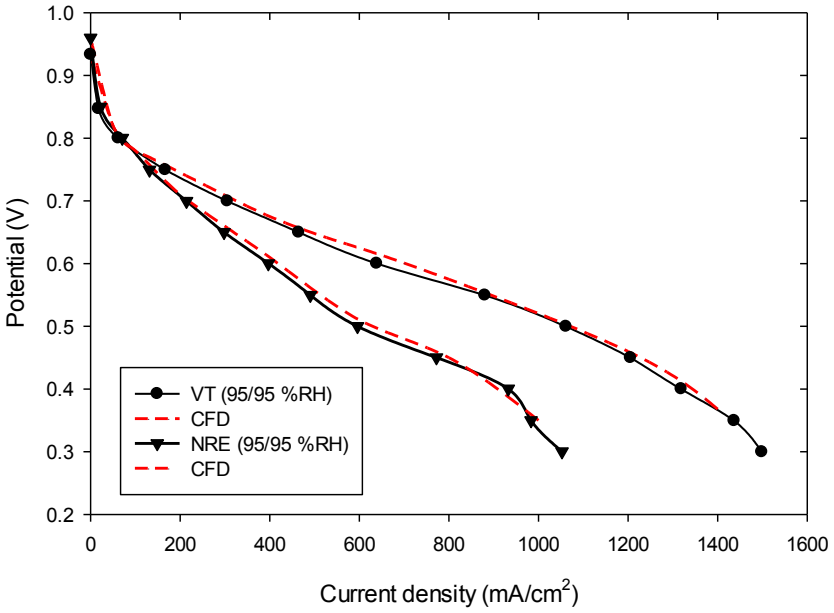

b)

Figure 6.4. Polarization curve of Nafion® (NRE211) and hydrocarbon (VT) membrane at a) 50% RH and b) 95% for both anode and cathode inlet.

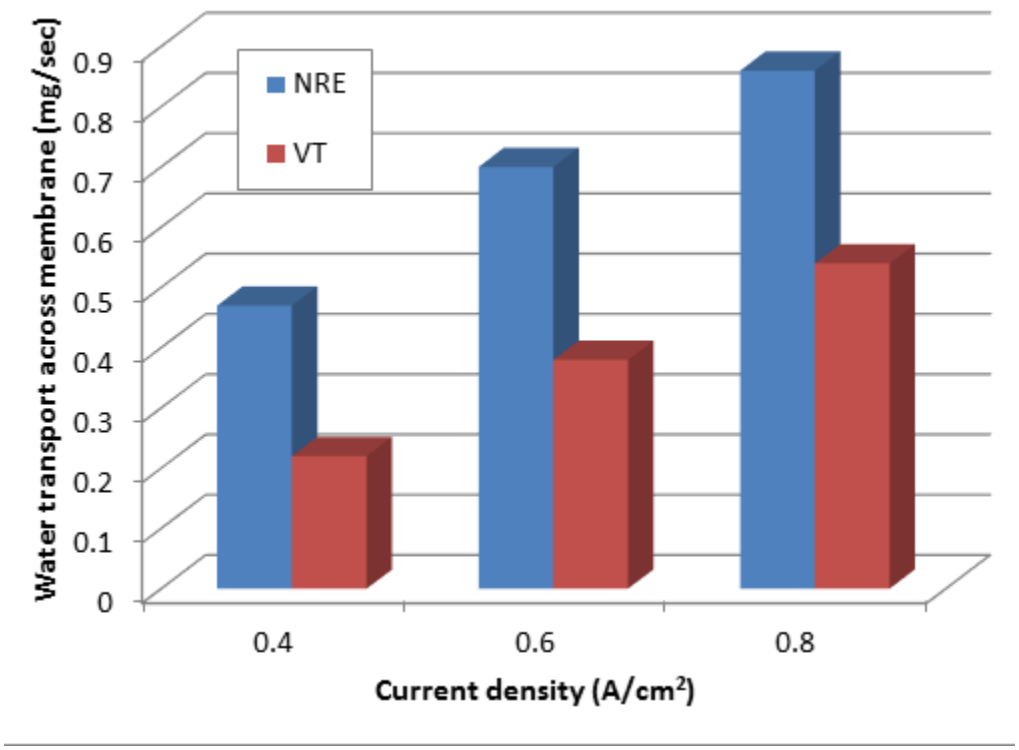

Figure 6.5. Comparison of water transport across membrane between Nafion® (NRE) and hydrocarbon (VT) membrane.

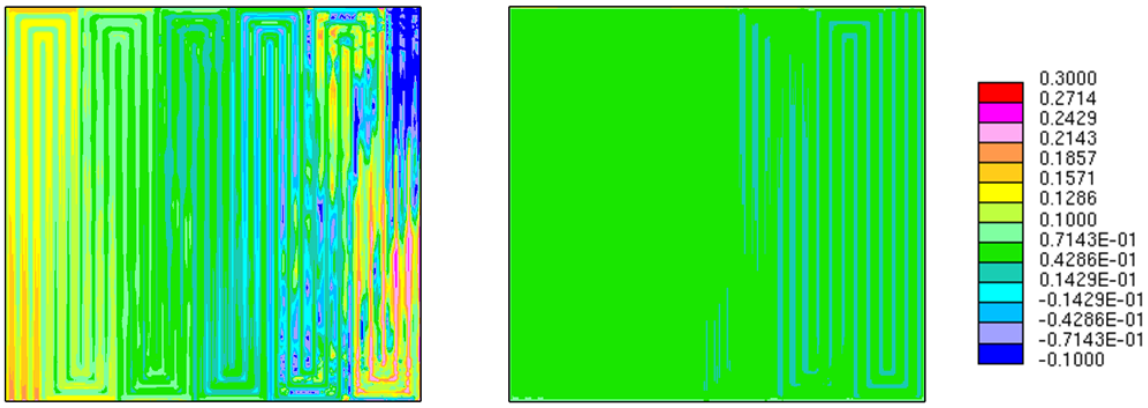

a) b)

Figure 6.6. CFD result of water flux across membrane between a) Nafion® (NRE211) and b) hydrocarbon (VT) membrane

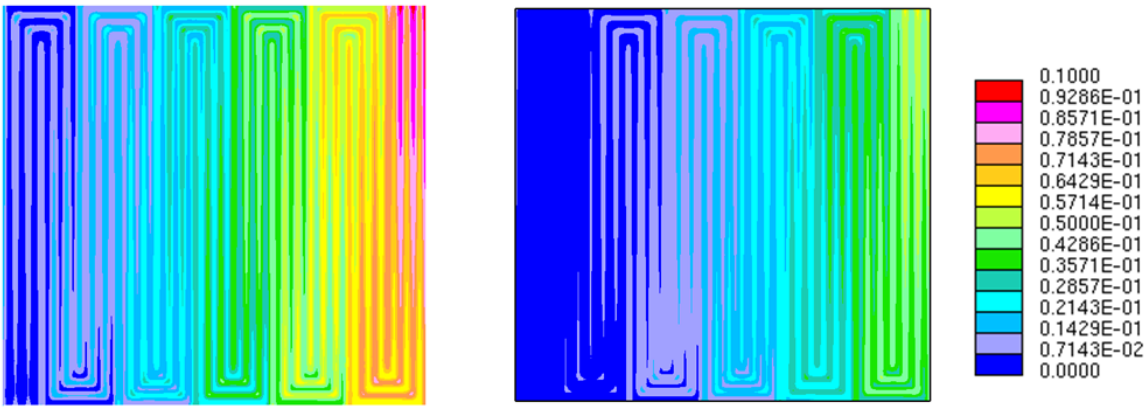

a) b)

Figure 6.7. CFD result of liquid water present in cathode MEA/GDL interface between a) Nafion® (NRE211) and b) hydrocarbon (VT) membrane

REFERENCES

1. B. Cunningham and D. G. Baird, *The development of economical bipolar plates for fuel cells.* Journal of Materials Chemistry, 2006. **16**(45), 4385-4388.

2. E. Middelman, W. Kout, B. Vogelaar, J. Lenssen, and E. de Waal, *Bipolar plates for PEM fuel cells.* Journal of Power Sources, 2003. **118**(1-2), 44-46.

3. I. Bar-On, R. Kirchain, and R. Roth, *Technical cost analysis for PEM fuel cells.* Journal of Power Sources, 2002. **109**(1), 71-75.

4. M. Rikukawa and K. Sanui, *Proton-conducting polymer electrolyte membranes based on hydrocarbon polymers.* Progress in Polymer Science, 2000. **25**(10), 1463-1502.

5. D. P. Davies, P. L. Adcock, M. Turpin, and S. J. Rowen, *Stainless steel as a bipolar plate material for solid polymer fuel cells.* Journal of Power Sources, 2000. **86**(1-2), 237-242.

6. H. McCrabb, A. Lozano-Morales, S. Snyder, L. Gebhart, and E. Taylor, *Through mask electrochemical machining.* ECS Transactions, 2009. **19**(26), 19.

7. H. McCrabb, E. Taylor, A. Lozano-Morales, S. Shimpalee, M. Inman, and J. W. Van Zee, *Through-mask electro-etching for fabrication of metal bipolar plate gas flow field channels.* ECS Transactions, 2010. **33**(1), 991.

8. S. Mahabunphachai and M. Koc, *Fabrication of micro-channel arrays on thin metallic sheet using internal fluid pressure: Investigations on size effects and development of design guidelines.* Journal of Power Sources, 2008. **175**(1), 363-371.

9. M. Koc and S. Mahabunphachai, *Feasibility investigations on a novel micro-manufacturing process for fabrication of fuel cell bipolar plates: Internal pressure-assisted embossing of micro-channels with in-die mechanical bonding.* Journal of Power Sources, 2007. **172**(2), 725-733.

10. S. Mahabunphachai, O. N. Cora, and M. Koc, *Effect of manufacturing processes on formability and surface topography of proton exchange membrane fuel cell metallic bipolar plates.* Journal of Power Sources, 2010. **195**(16), 5269-5277.

11. F. Dundar, E. Dur, S. Mahabunphachai, and M. Koc, *Corrosion resistance characteristics of stamped and hydroformed proton exchange membrane fuel cell metallic bipolar plates.* Journal of Power Sources, 2010. **195**(11), 3546-3552.

12. Y. Devrim, S. Erkan, N. Bac, and I. Eroglu, *Preparation and characterization of sulfonated polysulfone/titanium dioxide composite membranes for proton exchange membrane fuel cells.* International Journal of Hydrogen Energy, 2009. **34**(8), 3467-3475.

13. K. G. Gallagher, B. S. Pivovar, and T. F. Fuller, *Electro-osmosis and Water Uptake in Polymer Electrolytes in Equilibrium with Water Vapor at Low Temperatures.* Journal of the Electrochemical Society, 2009. **156**(3), B330-B338.

14. K. Tüber, D. Pócza, and C. Hebling, *Visualization of water buildup in the cathode of a transparent PEM fuel cell.* Journal of Power Sources, 2003. **124**(2), 403-414.

15. M. Venkatraman, S. Shimpalee, J. W. Van Zee, S. I. Moon, and C. W. Extrand, *Estimates of pressure gradients in PEMFC gas channels due to blockage by static liquid drops.* International Journal of Hydrogen Energy, 2009. **34**(13), 5522-5528.

16. V. Lilavivat, S. Shimpalee, J. W. Van Zee, H. McCrabb, and A. Lozano-Morales, *Fundamental Analyses, Observations, and Predictions of Liquid Droplet Movement on Etched-Metal Surfaces for PEMFC.* ECS Transactions, 2010. **33**(1), 973-978.

17. J. J. Bikerman, *Sliding of Drops from Surfaces of Different Roughnesses.* Journal of Colloid Science, 1950. **5**(4), 349-359.

18. A. Jamekhorshid, G. Karimi, and I. Noshadi, *Current distribution and cathode flooding prediction in a PEM fuel cell.* Journal of the Taiwan Institute of Chemical Engineers, 2011. **42**(4), 622-631.

19. M. M. Mench, C. Y. Wang, and M. Ishikawa, *In situ current distribution measurements in polymer electrolyte fuel cells.* Journal of the Electrochemical Society, 2003. **150**(8), A1052-A1059.

20. Y. G. Yoon, W. Y. Lee, T. H. Yang, G. G. Park, and C. S. Kim, *Current distribution in a single cell of PEMFC.* Journal of Power Sources, 2003. **118**(1-2), 193-199.

21. A. Z. Weber and J. Newman, *Modeling Transport in Polymer-Electrolyte Fuel Cells.* Chemical Reviews, 2004. **104**(10), 4679-4726.

22. C. Y. Wang, *Fundamental models for fuel cell engineering.* Chemical Reviews, 2004. **104**(10), 4727-4765.

23. http://physics.nist.gov/MajResFac/NIF/pemFuelCells.html.

24. B. C. H. Steele and A. Heinzel, *Materials for fuel-cell technologies.* Nature, 2001. **414**(6861), 345-352.

25. H. Tsuchiya and O. Kobayashi, *Mass production cost of PEM fuel cell by learning curve.* International Journal of Hydrogen Energy, 2004. **29**(10), 985-990.

26. Y. Wang and O. Northwood, *Effects of O-2 and H-2 on the corrosion of SS316L metallic bipolar plate materials in simulated anode and cathode environments of PEM fuel cells.* Electrochimica Acta, 2007. **52**(24), 6793-6798.

27. S. Karimi, N. Fraser, B. Roberts, and F. R. Foulkes, *A Review of Metallic Bipolar Plates for Proton Exchange Membrane Fuel Cells: Materials and Fabrication Methods.* Advances in Materials Science and Engineering, 2012.

28. A. Hermann, T. Chaudhuri, and P. Spagnol, *Bipolar plates for PEM fuel cells: A review.* International Journal of Hydrogen Energy, 2005. **30**(12), 1297-1302.

29. D. J. L. Brett and N. P. Brandon, *Review of materials and characterization methods for polymer electrolyte fuel cell flow-field plates.* Journal of Fuel Cell Science and Technology, 2007. **4**(1), 29-44.

30. G. O. Mepsted and J. M. Moore, *Performance and durability of bipolar plate materials*, in *Handbook of Fuel Cells*2010, John Wiley & Sons, Ltd.

31. K. Roßberg and V. Trapp, *Graphite–based bipolar plates*, in *Handbook of Fuel Cells*2010, John Wiley & Sons, Ltd.

32. B. D. Cunningham, J. Huang, and D. G. Baird, *Review of materials and processing methods used in the production of bipolar plates for fuel cells.* International Materials Reviews, 2007. **52**(1), 1-13.

33. V. Mehta and J. S. Cooper, *Review and analysis of PEM fuel cell design and manufacturing.* Journal of Power Sources, 2003. **114**(1), 32-53.

34. J. Wind, A. LaCroix, S. Braeuninger, P. Hedrich, C. Heller, and M. Schudy, *Metal bipolar plates and coatings*, in *Handbook of Fuel Cells*2010, John Wiley & Sons, Ltd.

35. R. C. Makkus, A. H. H. Janssen, F. A. de Bruijn, and R. Mallant, *Use of stainless steel for cost competitive bipolar plates in the SPFC.* Journal of Power Sources, 2000. **86**(1-2), 274-282.

36. J. Andre, L. Antoni, and J. P. Petit, *Corrosion resistance of stainless steel bipolar plates in a PEFC environment: A comprehensive study.* International Journal of Hydrogen Energy, 2010. **35**(8), 3684-3697.

37. H. L. Wang, M. A. Sweikart, and J. A. Turner, *Stainless steel as bipolar plate material for polymer electrolyte membrane fuel cells.* Journal of Power Sources, 2003. **115**(2), 243-251.

38. A. J. Sedriks, *Corrosion of stainless steel, 2. edition*. Other Information: PBD: 19961996. Medium: X; Size: [200] p.

39. Y. Fu, M. Hou, H. F. Xu, Z. J. Hou, P. W. Ming, Z. G. Shao, and B. L. Yi, *Ag-polytetrafluoroethylene composite coating on stainless steel as bipolar plate of proton exchange membrane fuel cell.* Journal of Power Sources, 2008. **182**(2), 580-584.

40. W. J. Lackey, *Carbon–Carbon Composites*, in *Encyclopedia of Materials: Science and Technology (Second Edition)*, K.H.J.B. Editors-in-Chief: , W.C. Robert, C.F. Merton, I. Bernard, J.K. Edward, M. Subhash, and V. Patrick, Editors. 2001, Elsevier: Oxford. p. 952-966.

41. T. M. Besmann, J. W. Klett, J. J. Henry, and E. Lara-Curzio, *Carbon/carbon composite bipolar plate for proton exchange membrane fuel cells.* Journal of the Electrochemical Society, 2000. **147**(11), 4083-4086.

42. C. Del Rio, M. C. Ojeda, J. L. Acosta, M. J. Escudero, E. Hontanon, and L. Daza, *New polymer bipolar plates for polymer electrolyte membrane fuel cells: Synthesis and characterization.* Journal of Applied Polymer Science, 2002. **83**(13), 2817-2822.

43. A. Aiyejina and M. K. S. Sastry, *PEMFC Flow Channel Geometry Optimization: A Review.* Journal of Fuel Cell Science and Technology, 2012. **9**(1).

44. E. Carcadea, I. Stefanescu, R. Ionete, H. Ene, D. Ingham, and L. Ma, *PEM fuel cell geometry optimisation using mathematical modeling.* The International Journal of Multiphysics, 2008. **2**(3), 313-326.

45. N. S. Siefert and S. Litster, *Voltage loss and fluctuation in proton exchange membrane fuel cells The role of cathode channel plurality and air stoichiometric ratio.* Journal of Power Sources, 2011. **196**(4), 1948-1954.

46. X. D. Wang, Y. Y. Duan, W. M. Yan, and X. F. Peng, *Effects of flow channel geometry on cell performance for PEM fuel cells with parallel and interdigitated flow fields.* Electrochimica Acta, 2008. **53**(16), 5334-5343.

47. X. D. Wang, X. X. Zhang, T. Liu, Y. Y. Duan, W. M. Yan, and D. J. Lee, *Channel Geometry Effect for Proton Exchange Membrane Fuel Cell With Serpentine Flow Field Using a Three-Dimensional Two-Phase Model.* Journal of Fuel Cell Science and Technology, 2010. **7**(5).

48. D. Cheddie and N. Munroe, *Review and comparison of approaches to proton exchange membrane fuel cell modeling.* Journal of Power Sources, 2005. **147**(1-2), 72-84.

49. X. Liu, H. Guo, and C. F. Ma, *Water flooding and two-phase flow in cathode channels of proton exchange membrane fuel cells.* Journal of Power Sources, 2006. **156**(2), 267-280.

50. M. Noponen, T. Mennola, M. Mikkola, T. Hottinen, and P. Lund, *Measurement of current distribution in a free-breathing PEMFC.* Journal of Power Sources, 2002. **106**(1-2), 304-312.

51. J. Stumper, S. A. Campbell, D. P. Wilkinson, M. C. Johnson, and M. Davis, *In-situ methods for the determination of current distributions in PEM fuel cells.* Electrochimica Acta, 1998. **43**(24), 3773-3783.

52. Y. Yu, X.-Z. Yuan, H. Li, E. Gu, H. Wang, G. Wang, and M. Pan, *Current mapping of a proton exchange membrane fuel cell with a segmented current collector during the gas starvation and shutdown processes.* International Journal of Hydrogen Energy, 2012. **37**(20), 15288-15300.

53. S. J. C. Cleghorn, C. R. Derouin, M. S. Wilson, and S. Gottesfeld, *A printed circuit board approach to measuring current distribution in a fuel cell.* Journal of Applied Electrochemistry, 1998. **28**(7), 663-672.

54. I. Alaefour, G. Karimi, K. Jiao, and X. Li, *Measurement of current distribution in a proton exchange membrane fuel cell with various flow arrangements - A parametric study.* Applied Energy, 2012. **93**, 80-89.

55. C. Wieser, A. Helmbold, and E. Gulzow, *A new technique for two-dimensional current distribution measurements in electrochemical cells.* Journal of Applied Electrochemistry, 2000. **30**(7), 803-807.

56. G. S. Zhang, S. L. Shen, L. J. Guo, and H. T. Liu, *Dynamic characteristics of local current densities and temperatures in proton exchange membrane fuel cells during reactant starvations.* International Journal of Hydrogen Energy, 2012. **37**(2), 1884-1892.

57. I. Alaefour, G. Karimi, K. Jiao, S. Al Shakhshir, and X. Li, *Experimental study on the effect of reactant flow arrangements on the current distribution in proton exchange membrane fuel cells.* Electrochimica Acta, 2011. **56**(5), 2591-2598.

58. T. V. Reshetenko, G. Bender, K. Bethune, and R. Rocheleau, *A segmented cell approach for studying the effects of serpentine flow field parameters on PEMFC current distribution.* Electrochimica Acta, 2013. **88**, 571-579.

59. T. E. Springer, T. A. Zawodzinski, and S. Gottesfeld, *Polymer Electrolyte Fuel-Cell Model.* Journal of the Electrochemical Society, 1991. **138**(8), 2334-2342.

60. T. F. Fuller and J. Newman, *Water and Thermal Management in Solid-Polymer-Electrolyte Fuel-Cells.* Journal of the Electrochemical Society, 1993. **140**(5), 1218-1225.

61. Z. H. Wang, C. Y. Wang, and K. S. Chen, *Two-phase flow and transport in the air cathode of proton exchange membrane fuel cells.* Journal of Power Sources, 2001. **94**(1), 40-50.

62. T. V. Nguyen and R. E. White, *A Water and Heat Management Model for Proton-Exchange-Membrane Fuel-Cells.* Journal of the Electrochemical Society, 1993. **140**(8), 2178-2186.

63. B. Carnes, D. Spernjak, G. Luo, L. Hao, K. S. Chen, C.-Y. Wang, R. Mukundan, and R. L. Borup, *Validation of a two-phase multidimensional polymer electrolyte membrane fuel cell computational model using current distribution measurements.* Journal of Power Sources, 2013(0).

64. W. K. Lee, S. Shimpalee, and J. W. Van Zee, *Verifying predictions of water and current distributions in a serpentine flow field polymer electrolyte membrane fuel cell.* Journal of the Electrochemical Society, 2003. **150**(3), A341-A348.

65. T. E. Springer, M. S. Wilson, and S. Gottesfeld, *Modeling and Experimental Diagnostics in Polymer Electrolyte Fuel-Cells.* Journal of the Electrochemical Society, 1993. **140**(12), 3513-3526.

66. D. Gerteisen, N. Zamel, C. Sadeler, F. Geiger, V. Ludwig, and C. Hebling, *Effect of operating conditions on current density distribution and high frequency resistance in a segmented PEM fuel cell.* International Journal of Hydrogen Energy, 2012. **37**(9), 7736-7744.

67. D. M. Bernardi and M. W. Verbrugge, *A Mathematical-Model of the Solid-Polymer-Electrolyte Fuel-Cell.* Journal of the Electrochemical Society, 1992. **139**(9), 2477-2491.

68. D. M. Bernardi and M. W. Verbrugge, *Mathematical-Model of a Gas-Diffusion Electrode Bonded to a Polymer Electrolyte.* Aiche Journal, 1991. **37**(8), 1151-1163.

69. S. Shimpalee and S. Dutta, *Numerical prediction of temperature distribution in PEM fuel cells.* Numerical Heat Transfer Part a-Applications, 2000. **38**(2), 111-128.

70. S. Shimpalee, V. Lilavivat, J. W. Van Zee, H. McCrabb, and A. Lozano-Morales, *Understanding the effect of channel tolerances on performance of PEMFCs.* International Journal of Hydrogen Energy, 2011. **36**(19), 12512-12523.

71. S. Shimpalee, M. Ohashi, J. W. Van Zee, C. Ziegler, C. Stoeckmann, C. Sadeler, and C. Hebling, *Experimental and numerical studies of portable PEMFC stack.* Electrochimica Acta, 2009. **54**(10), 2899-2911.

72. S. Shimpalee, D. Spuckler, and J. W. Van Zee, *Prediction of transient response for a 25-cm(2) PEM fuel cell.* Journal of Power Sources, 2007. **167**(1), 130-138.

73. S. Shimpalee and J. W. Van Zee, *Numerical studies on rib & channel dimension of flow-field on PEMFC performance.* International Journal of Hydrogen Energy, 2007. **32**(7), 842-856.

74. S. Dutta, S. Shimpalee, and J. W. Van Zee, *Numerical prediction of mass-exchange between cathode and anode channels in a PEM fuel cell.* International Journal of Heat and Mass Transfer, 2001. **44**(11), 2029-2042.

75. S. Dutta, S. Shimpalee, and J. W. Van Zee, *Three-dimensional numerical simulation of straight channel PEM fuel cells.* Journal of Applied Electrochemistry, 2000. **30**(2), 135-146.

76. CD Adapco Group, Star-CD 4.14 Methodology, http://www.adapco.com

77. CD Adapco Group, ES-PEMFC 2.50 methodology and tutorial manual, http://www.adapco.com

78. D. H. Jeon, S. Greenway, S. Shimpalee, and J. W. Van Zee, *The effect of serpentine flow-field designs on PEM fuel cell performance.* International Journal of Hydrogen Energy, 2008. **33**(3), 1052-1066.

79. A. P. Manso, F. F. Marzo, A. R. Pierna, J. Barranco, A. Lorenzo, and J. Barroso, *Design Optimization of a Polymer Electolyte Membrane Fuel Cell, PEMFC.* Journal of New Materials for Electrochemical Systems, 2009. **12**(2-3), 133-137.

80. S. Lee, H. Jeong, B. Ahn, T. Lim, and Y. Son, *Parametric study of the channel design at the bipolar plate in PEMFC performances.* International Journal of Hydrogen Energy, 2008. **33**(20), 5691-5696.

81. K. B. S. Prasad and S. Jayanti, *Effect of channel-to-channel cross-flow on local flooding in serpentine flow-fields.* Journal of Power Sources, 2008. **180**(1), 227-231.

82. A. P. Manso, F. F. Marzo, M. G. Mujika, J. Barranco, and A. Lorenzo, *Numerical analysis of the influence of the channel cross-section aspect ratio on the performance of a PEM fuel cell with serpentine flow field design.* International Journal of Hydrogen Energy, 2011. **36**(11), 6795-6808.

83. http://www.fuelcelltechnologies.com/fuelcell/products/single_cell_hardware.asp.

84. K. Tuber, D. Pocza, and C. Hebling, *Visualization of water buildup in the cathode of a transparent PEM fuel cell.* Journal of Power Sources, 2003. **124**(2), 403-414.

85. H. Yamada, T. Hatanaka, H. Murata, and Y. Morimoto, *Measurement of flooding in gas diffusion layers of polymer electrolyte fuel cells with conventional flow field.* Journal of the Electrochemical Society, 2006. **153**(9), A1748-A1754.

86. A. Turhan, S. Kim, M. Hatzell, and M. M. Mench, *Impact of channel wall hydrophobicity on through-plane water distribution and flooding behavior in a polymer electrolyte fuel cell.* Electrochimica Acta, 2010. **55**(8), 2734-2745.

87. N. Akhtar, A. Qureshi, J. Scholta, C. Hartnig, M. Messerschmidt, and W. Lehnert, *Investigation of water droplet kinetics and optimization of channel geometry for PEM fuel cell cathodes.* International Journal of Hydrogen Energy, 2009. **34**(7), 3104-3111.

88. C. W. Extrand, *A thermodynamic model for contact angle hysteresis.* Journal of Colloid and Interface Science, 1998. **207**(1), 11-19.

89. T. Young, *An Essay on the Cohesion of Fluids.* Philosophical Transactions of the Royal Society of London, 1805. **95**(ArticleType: research-article / Full publication date: 1805 /), 65-87.

90. R. N. Wenzel, *Resistance of solid surfaces to wetting by water.* Industrial and Engineering Chemistry, 1936. **28**, 988-994.

91. A. B. D. Cassie and S. Baxter, *Wettability of porous surfaces.* Transactions of the Faraday Society, 1944. **40**, 0546-0550.

92. V. Hejazi and M. Nosonovsky, *Contact angle hysteresis in multiphase systems.* Colloid and Polymer Science, 2013. **291**(2), 329-338.

93. M. Sakai, H. Kono, A. Nakajima, X. Zhang, H. Sakai, M. Abe, and A. Fujishima, *Sliding of water droplets on the superhydrophobic surface with ZnO nanorods.* Langmuir, 2009. **25**(24), 14182-6.

94. L. Gao and T. J. McCarthy, *How Wenzel and cassie were wrong.* Langmuir, 2007. **23**(7), 3762-5.

95. N. A. Patankar, *On the modeling of hydrophobic contact angles on rough surfaces.* Langmuir, 2003. **19**(4), 1249-1253.

96. X. F. Chen, X. P. Wang, and X. M. Xu, *Effective contact angle for rough boundary.* Physica D-Nonlinear Phenomena, 2013. **242**(1), 54-64.

97. X. M. Li, D. Reinhoudt, and M. Crego-Calama, *What do we need for a superhydrophobic surface? A review on the recent progress in the preparation of superhydrophobic surfaces.* Chemical Society Reviews, 2007. **36**(9), 1529-1529.

98. A. Theodorakakos, T. Ous, A. Gavaises, J. M. Nouri, N. Nikolopoulos, and H. Yanagihara, *Dynamics of water droplets detached from porous surfaces of relevance to PEM fuel cells.* Journal of Colloid and Interface Science, 2006. **300**(2), 673-687.

99. John Wiley & Sons, Inc, Transport phenomena,

100. E. C. Kumbur, K. V. Sharp, and M. M. Mench, *Liquid droplet behavior and instability in a polymer electrolyte fuel cell flow channel.* Journal of Power Sources, 2006. **161**(1), 333-345.

101. K. S. Chen, M. A. Hickner, and D. R. Noble, *Simplified models for predicting the onset of liquid water droplet instability at the gas diffusion layer/gas flow channel interface.* International Journal of Energy Research, 2005. **29**(12), 1113-1132.

102. M. Miwa, A. Nakajima, A. Fujishima, K. Hashimoto, and T. Watanabe, *Effects of the surface roughness on sliding angles of water droplets on superhydrophobic surfaces.* Langmuir, 2000. **16**(13), 5754-5760.

103. V. Mortazavi, R. M. D'Souza, and M. Nosonovsky, *Study of contact angle hysteresis using the Cellular Potts Model.* Physical Chemistry Chemical Physics, 2013. **15**(8), 2749-2756.

104. E. Wolfram and R. Faust, *Wetting, spreading, and adhesion*, in *Wetting, spreading, and adhesion*1978, Academic Press.

105. L. You and H. Liu, *A two-phase flow and transport model for the cathode of PEM fuel cells.* International Journal of Heat and Mass Transfer, 2002. **45**(11), 2277-2287.

106. U. Pasaogullari and C. Y. Wang, *Liquid water transport in gas diffusion layer of polymer electrolyte fuel cells.* Journal of the Electrochemical Society, 2004. **151**(3), A399-A406.

107. C. K. Mittelsteadt, P. Cortes, V. Lilavivat, S. Shimpalee, and J. W. Van Zee, *Novel Current Distribution Board for PEM Devices.* ECS Transactions, 2011. **41**(1), 549-559.

108. http://www2.dupont.com/FuelCells/en_US/products/nafion.html.

109. V. A. Sethuraman, J. W. Weidner, A. T. Haug, and L. V. Protsailo, *Durability of perfluorosulfonic acid and hydrocarbon membranes: Effect of humidity and temperature.* Journal of the Electrochemical Society, 2008. **155**(2), B119-B124.

110. Y. Chen, R. L. Guo, C. H. Lee, M. Lee, and J. E. McGrath, *Partly fluorinated poly(arylene ether ketone sulfone) hydrophilic-hydrophobic multiblock copolymers for fuel cell membranes.* International Journal of Hydrogen Energy, 2012. **37**(7), 6132-6139.

111. H. S. Lee, O. Lane, and J. E. McGrath, *Development of multiblock copolymers with novel hydroquinone-based hydrophilic blocks for proton exchange membrane (PEM) applications.* Journal of Power Sources, 2010. **195**(7), 1772-1778.

112. M. A. Hickner, H. Ghassemi, Y. S. Kim, B. R. Einsla, and J. E. McGrath, *Alternative polymer systems for proton exchange membranes (PEMs).* Chemical Reviews, 2004. **104**(10), 4587-4611.

113. M. Eikerling, Y. I. Kharkats, A. A. Kornyshev, and Y. M. Volfkovich, *Phenomenological theory of electro-osmotic effect and water management in polymer electrolyte proton-conducting membranes.* Journal of the Electrochemical Society, 1998. **145**(8), 2684-2699.

114. C. K. Mittelsteadt and J. Staser, *Simultaneous Water Uptake, Diffusivity and Permeability Measurement of Perfluorinated Sulfonic Acid Polymer Exchange Membranes.* Meeting Abstracts, 2011. **MA2011-02**(16), 800.

115. W. Braff and C. K. Mittelsteadt, *Electroosmotic Drag Coefficient of Proton Exchange Membrane as a Function of Relative Humidity.* ECS Transactions, 2008. **16**(2), 309-316.

116. H. Xu, J. Ma, and C. Mittelsteadt, *Novel System for Characterizing Electro-Osmotic Drag Coefficient of Proton Exchange Membranes.* Meeting Abstracts, 2012. **MA2012-02**(13), 1304.

117. Y. Chen, J. R. Rowlett, C. H. Lee, O. R. Lane, D. J. VanHouten, M. Zhang, R. B. Moore, and J. E. McGrath, *Synthesis and characterization of multiblock partially fluorinated hydrophobic poly(arylene ether sulfone)-hydrophilic disulfonated poly(arylene ether sulfone) copolymers for proton exchange membranes.* Journal of Polymer Science Part A: Polymer Chemistry, 2013. **51**(10), 2301-2310.

APPENDIX A

MODEL METHODOLOGY[76]

The Computational Fluid Dyanimcs (CFD) model used in this dissertation is commercially available from the CD-adapco company and marketed under the product name, es-pemfc (http://www.cd-adapco.com/). This appendix summarizes the model methodology.

A typical PEMFC is composed of the anode flow channel, anode diffusion layer, MEA, cathode diffusion layer, and cathode flow channel as show in Figure A.1. This figure also shows a typical grid arrangement for different PEMFC components. Four chemical species (hydrogen, oxygen, nitrogen, and water) are considered in the model. The water can exist in either liquid or gas phase and nitrogen can exist on either side of the MEA. The model will solve the complete three-dimensional (3-D) Navier-Stokes equations to obtain the velocity and pressure distributions along the flow channels. Moreover, the temperature distribution of the entire PEMFC will be computed by a 3-D energy equation. The conservation of mass equation in the 3-D model was modified to include the electrochemical aspects of fuel cell as shown in Table A.1. This table shows the governing of mass, momentum, and energy balance equation. The Table A.2 describes the spatial source terms including species and heat sources created by the electrochemical and phase-change reactions. The phase change of water is calculated with the source terms, S_m, shown by Equations A.8 and A.10-A.15. These electrochemical reaction terms correspond to the consumption of hydrogen and water

vapor in the anode, and the consumption of oxygen and production of water vapor in the cathode. Equation A.11 accounts for the phase change in water by comparing the partial pressure of water vapor to the saturation pressure at the local temperature. If the partial pressure of water vapor is larger than the saturation pressure, water vapor condenses to form liquid water. On the other hand, if the partial pressure of water vapor is lower than saturation pressure, the liquid water evaporates to form water vapor. The amount evaporated is limited by the amount of liquid water available in each control volume. Equation A.12 and A.13 present the source terms of water vapor produced and consumed by electrochemical effects on the membrane surface of both the anode and cathode. The flux of water through the MEA is included as source terms at the anode and cathode by accounting for net water flux per proton, water content in the membrane, and water diffusion coefficient as defined by Equations A.20,21, and 23. The momentum transport equation has a source term for the porous media ($z3 \leq z \leq z4$ and $z2 \leq z \leq z1$) used to model flows through the diffusion layer as shown in Table A.2.

The species transport equations (Equations A.3-6) are solved for the mass flow rates of hydrogen, water vapor, liquid water, and oxygen species based on the bulk-mixture velocities, *u*, *v*, and *w*, and the diffusion mass fluxes $\mathbf{J}(\zeta,n)$. The liquid water in this model is assumed to be the small droplets and freely suspended in the gas flow and, thus a Laplacian form of the Navier-Stokes equation is used. Therefore, the model considers two phase flow together (homogeneous two-phase flow). This assumption also holds for normal operating conditions of a PEMFC because high liquid loading will not allow for steady state operation. The binary diffusion coefficients are calculated as shown by Equation A.19. The diffusion coefficient of each species in the mixture should be

reduced in the diffusion layer to account for the effect of porosity and pore-tortuosity. The flux of water through the membrane is critical to the predictions. Equation A.22 gives the relationship between the electro-osmotic drag coefficient and water content in the membrane. The diffusion coefficient function (Equation A.23) uses the corrected diffusion coefficient (D_λ) and it depends on cell temperature and water content of membrane surface.

The expressions for water concentration in liquid and gaseous phases at the anode and cathode sides are presented in Equation A.24 and A.25. The local current density equation given in Equation A.26 is a function of membrane properties, cell voltage, and cell over-potential. The equation for local membrane conductivity of membrane ionic resistance is also provided in Equation A.27. Equation A.28 shows the expression of local cell over-potential which includes the effect of polarization due to dilution of the hydrogen by nitrogen as well as the oxygen over-potential.

The source terms in Table A.2 correspond to the control volume and not the boundary conditions at the anode and cathode interfaces. For the correct determination of the concentrations and activities at the membrane-diffusion layer interface, mole fraction for each species used in these equations is extrapolated to the membrane surface. The exception to this linear extrapolation is when there is a liquid film of sufficient thickness. In that case, the solubility for the reacting gases at the gas/water film interface was included and the mass transfer resistance of gas diffusing through the film (if it exists) was accounted for more accurately. The Henry's law was used to calculate the solubility of hydrogen and oxygen in the liquid water film if it is present on the surface of MEA. The diffusion length of this soluble gas is determined by the thickness of the film of the

water on the MEA corrected for the porosity of the GDL. Thus the average pore flooding is excused by considering an average film thickness. The equations for these effects are shown in Equation A.29-33.

The heat sources used in this model combine the electrochemical energy loss (S_{he}) and the thermal effects produced by the phase change of water (S_{hp}). The heat source created by electrochemical energy losses occurs inside the MEA at z_8 in Figure A.1. This electrochemical heat source is given by the difference of the total energy released by the electrochemical reaction at cathode membrane surface (z2 in Figure A.1) and the electrical energy extracted out of the fuel cell as shown in Equation A.16. A second heat source (S_{hp}) is produced by the phase change effects of water and it can take place anywhere in the flow channels and diffusion layers (Equation A.17).

A control volume technique base on commercial CFD solver, STAR-CD (version 4.26) was used to solve the coupled governing equations. The STAR-CD allows es-pemfc to provide efficient computation time and numerical convergence of the governing equations to a desired tolerance. This software requires specification of the source terms for species transport equations, the phase change equations for water, and heat generation equations created by electrochemical reactions as shown in Table A.2.

Table A.1. Governing equations

Description	Mathematical expression	
Conservation of Mass	$\frac{\partial(\rho u)}{\partial x}+\frac{\partial(\rho v)}{\partial y}+\frac{\partial(\rho w)}{\partial z}=S_m$	(A.1)
Momentum transport	$u\frac{\partial(\rho u)}{\partial x}+v\frac{\partial(\rho u)}{\partial y}+w\frac{\partial(\rho u)}{\partial z}=-\frac{\partial P}{\partial x}+\frac{\partial}{\partial x}\left(\mu\frac{\partial u}{\partial x}\right)+\frac{\partial}{\partial y}\left(\mu\frac{\partial u}{\partial y}\right)+\frac{\partial}{\partial z}\left(\mu\frac{\partial u}{\partial z}\right)+S_{px}$ $u\frac{\partial(\rho v)}{\partial x}+v\frac{\partial(\rho v)}{\partial y}+w\frac{\partial(\rho v)}{\partial z}=-\frac{\partial P}{\partial y}+\frac{\partial}{\partial x}\left(\mu\frac{\partial v}{\partial x}\right)+\frac{\partial}{\partial y}\left(\mu\frac{\partial v}{\partial y}\right)+\frac{\partial}{\partial z}\left(\mu\frac{\partial v}{\partial z}\right)+S_{py}$ $u\frac{\partial(\rho w)}{\partial x}+v\frac{\partial(\rho w)}{\partial y}+w\frac{\partial(\rho w)}{\partial z}=-\frac{\partial P}{\partial z}+\frac{\partial}{\partial x}\left(\mu\frac{\partial w}{\partial x}\right)+\frac{\partial}{\partial y}\left(\mu\frac{\partial w}{\partial y}\right)+\frac{\partial}{\partial z}\left(\mu\frac{\partial w}{\partial z}\right)+S_{pz}$	(A.2)
Hydrogen transport (anode side)	$u\frac{\partial(\rho m_{H_2})}{\partial x}+v\frac{\partial(\rho m_{H_2})}{\partial y}+w\frac{\partial(\rho m_{H_2})}{\partial z}=\frac{\partial(J_{x,H_2})}{\partial x}+\frac{\partial(J_{y,H_2})}{\partial y}+\frac{\partial(J_{z,H_2})}{\partial z}+S_{H_2}$	(A.3)
Water Vapor transport	$u\frac{\partial(\rho m_{wv})}{\partial x}+v\frac{\partial(\rho m_{wv})}{\partial y}+w\frac{\partial(\rho m_{wv})}{\partial z}$ $=\frac{\partial(J_{x,wv})}{\partial x}+\frac{\partial(J_{y,wv})}{\partial y}+\frac{\partial(J_{z,wv})}{\partial z}+S_{wv_P}+S_{awv_e}+S_{cwv_e}$	(A.4)
Water liquid transport	$u\frac{\partial(\rho m_{wl})}{\partial x}+v\frac{\partial(\rho m_{wl})}{\partial y}+w\frac{\partial(\rho m_{wl})}{\partial z}=\frac{\partial(J_{x,wl})}{\partial x}+\frac{\partial(J_{y,wl})}{\partial y}+\frac{\partial(J_{z,wl})}{\partial z}+S_{wl_P}$	(A.5)
Oxygen transport (cathode side)	$u\frac{\partial(\rho m_{O_2})}{\partial x}+v\frac{\partial(\rho m_{O_2})}{\partial y}+w\frac{\partial(\rho m_{O_2})}{\partial z}=\frac{\partial(J_{x,O_2})}{\partial x}+\frac{\partial(J_{y,O_2})}{\partial y}+\frac{\partial(J_{z,O_2})}{\partial z}+S_{O_2}$	(A.6)
Energy equation	$\frac{\partial(\rho uh)}{\partial x}+\frac{\partial(\rho vh)}{\partial y}+\frac{\partial(\rho wh)}{\partial z}=\frac{\partial}{\partial x}\left(k\frac{\partial T}{\partial x}\right)+\frac{\partial}{\partial y}\left(k\frac{\partial T}{\partial y}\right)+\frac{\partial}{\partial z}\left(k\frac{\partial T}{\partial z}\right)+S_{h_P}+S_{h_e}$	(A.7)

Table A.2. Source terms for governing equation

Description	Non-zero volumetric source terms and location of application according to Figure A.1	
Conservation of Mass	$S_m = S_{H_2} + S_{wv_P} + S_{wl_P} + S_{awv_e}\ at\ z = z_3$ $S_m = S_{O_2} + S_{wv_P} + S_{wl_P} + S_{cwv_e}\ at\ z = z_2$	(A.8)
Momentum transport	$S_{px} = -\frac{\mu u}{\beta_x}, S_{py} = -\frac{\mu v}{\beta_y}, S_{pz} = -\frac{\mu w}{\beta_z}\ at\ z_1 \le z \le z_2\ and\ z_3 \le z \le z_4$	(A.9)
Hydrogen transport (anode side)	$S_{H_2} = -\frac{I(x,y)}{2F} M_{H_2} A_{cv}\ at\ z = z_3$	(A.10)
Water Vapor transport	$S_{wv_p} = \frac{M_{H_2O} \sum_{n\ of\ V} \frac{mass_{n\ of\ v}}{M_{n\ of\ v}}}{\left(1 - \frac{P_{wv}^{sat}}{P}\right)} \left[\frac{P_{wv}^{sat} - P_{wv}}{P}\right] \times r\ at\ z_0 \le z \le z_5$	(A.11)
	$S_{awv_e} = -\frac{\alpha(x,y)}{F} I(x,y) M_{H_2O} A_{cv}\ at\ z = z_3$	(A.12)
	$S_{cwv_e} = \frac{1 + 2\alpha(x,y)}{F} I(x,y) M_{H_2O} A_{cv}\ at\ z = z_2$	(A.13)
Water liquid transport	$S_{wl_p} = -S_{wv_p}\ at\ z_0 \le z \le z_5$	(A.14)
Oxygen transport (cathode side)	$S_{O_2} = -\frac{I(x,y)}{4F} M_{O_2} A_{cv}\ at\ z = z_2$	(A.15)
Energy equation	Heat source by energy losses $S_{h_e} = h_{rxn} \times \left[\frac{1}{2F}\ I(x,y)\ \times A_{cv}\right]_{z=z_2} - (I(x,y) V_{cell} A_{cv})_{z=z_2}\ at\ z = z_8$	(A.16)
	Heat source by phase change $S_{h_p} = S_{wl_p} \times h_{fg}\ at\ z_0 \le z \le z_5$	(A.17)

Table A.3. Constitutive equations for modeling electrochemical effects.

Description	Mathematical expression
Diffusion mass flux of species n in ζ direction	$J_{\xi,n} = -\rho D_{\xi,n} \frac{\partial m_{K,n}}{\partial \xi}$ (A.18)
Binary diffusion coefficient	$\frac{P D_{n,j}(x,y)}{\left(P_{c-n} \times P_{c-j}\right)^{\frac{1}{3}} \cdot \left(T_{c-n} T_{c-j}\right)^{\frac{5}{12}} \cdot \left(\frac{1}{M_n} + \frac{1}{M_j}\right)^{\frac{1}{2}}} = 3.64 \times 10^{-8} \left(\frac{T(x,y)}{\sqrt{T_{c-n} T_{c-j}}}\right)^{2.334}$ (A.19)
Net water transfer coefficient per proton	$\alpha(x,y) = n_d(x,y) - \frac{F}{I(x,y)} D_w(x,y) \frac{C_{wc}(x,y) - C_{wa}(x,y)}{t_m}$ (A.20)
Water content in the membrane	$\lambda = 0.043 + 17.81 a_a - 39.85 a_a^2 + 36.0 a_a^3 \,; 0 < a_a \leq 1$ $= 14 + 1.4(a_a - 1) \,; 1 < a_a \leq 3$ (A.21)
Electro-osmotic drag coefficient	$n_d = 0.0029\lambda^2 + 0.05\lambda - 3.4 \times 10^{-19}$ (A.22)
Water diffusion coefficient	$D_w = D_\lambda \exp\left(2416\left(\frac{1}{303} - \frac{1}{T(x,y)}\right)\right) ; D_\lambda = 10^{-10}, \lambda < 2 \,; D_\lambda = 10^{-10}\left(1 + 2(\lambda - 2)\right), 2 \leq \lambda \leq 3$ $D_\lambda = 10^{-10}\left(3 - 1.67(\lambda - 3)\right), 3 < \lambda < 4.5 \,;\; D_\lambda = 1.25 \times 10^{-10}, \lambda \geq 4.5$ (A.23)
Water vapor concentration for anode and cathode surface of the MEA	$C_{wK}(x,y) = \frac{\rho_{m,dry}}{M_{m,dry}} (0.043 + 17.8 a_K - 39.8 a_K^2 + 36.0 a_K^3) \,; a_K \leq 1$ $= \frac{\rho_{m,dry}}{M_{m,dry}} \left(14 + 1.4(a_K - 1)\right) ; for\ a_k > 1\,, where\ K = a\ or\ c$ (A.24)
Water activity	$a_K = \frac{X_{w,K} P(x,y)}{P_{w,K}^{sat}}$ (A.25)
Local current density	$I(x,y) = \frac{\sigma_m(x,y)}{t_m} \{V_{OC} - V_{cell} - \eta(x,y)\}$ (A.26)
Local membrane conductivity	$\sigma_m(x,y) = \left(0.514 \frac{M_{m,dry}}{\rho_{m,dry}} C_{wa}(x,y) - 0.326\right) \exp\left(1268\left(\frac{1}{303} - \frac{1}{T(x,y)}\right)\right)$ (A.27)
Local overpotential	$\eta(x,y) = \frac{RT(x,y,z_2)}{\alpha_c F} \ln\left[\frac{I(x,y) P(x,y,z_2)}{I_{0_{O_2}} P_{O_2}(x,y,z_2)}\right] + \frac{RT(x,y,z_3)}{\alpha_a F} \ln\left[\frac{I(x,y) P(x,y,z_3)}{I_{0_{H_2}} P_{H_2}(x,y,z_3)}\right]$ (A.28)
Water film thickness	$t_{f,k} = \frac{m_{w,l}(\sum mass_n)}{\varepsilon \rho_{wl} Area_{cv}}$ (A.29)
Gas Solubility	$P_{O_2}(x,y,z_2) = X_{O_2}(x,y,z_2) P(x,y,z_2)$ (A.30) $-\frac{I(x,y)}{4F} M_{O_2} = \rho_{O_2} D_{O_2,l} \left[\frac{X_{O_2}(x,y,z_2 - t_{f,c}) P(x,y,z_2 - t_{f,c}) H_{O_2,l}^{-1} - X_{O_2}(x,y,x_2)}{t_{f,c}}\right]$ (A.31) $P_{H_2}(x,y,z_3) = X_{H_2}(x,y,z_3) P(x,y,z_3)$ (A.32) $-\frac{I(x,y)}{2F} M_{H_2} = \rho_{H_2} D_{H_2,l} \left[\frac{X_H(x,y,z_3 - t_{f,a}) P(x,y,z_3 - t_{f,a}) H_{H_2,l}^{-1} - X_{H_2}(x,y,x_3)}{t_{f,a}}\right]$ (A.33)

Nomenclature

A_{cv} specific surface area of the control volume (c.v.), m^{-1}

a_k activity of water in stream k, dimensionless

$Area_{cv}$ surface area of control volume, m^2

C_{wk} concentration of water vapor at k^{th} interface of membrane, mol m^{-3}

C_{wlk} concentration of water liquid at k^{th} interface of membrane, mol m^{-3}

$D_{H2,l}$ diffusion coefficient of H_2 in liquid water film, $6.3x10^{-9}$ m^2 s^{-1}

$D_{n,j}$ binary diffusion coefficient of species n in gas mixture j, m^2 s^{-1}

$D_{O2,l}$ diffusion coefficient of O_2 in liquid water film, $2.4x10^{-9}$ m^2 s^{-1}

D_w diffusion coefficient of water, m2 s^{-1}

F Faraday constant, 96487 C mole-of-electrons^{-1}

h_{fg} enthalpy of vaporization for water, kJ $kmol^{-1}$

$H_{H2,l}$ Henry's law constant for H2 in liquid water film, 8.9x109 Pa

$H_{O2,l}$ Henry's law constant for O2 in liquid water film, 2.12x1010 Pa

h_{rxn} enthalpy of water fromation, kJ $kmol^{-1}$

I local current density, A m^{-2}

$I_{o,K}$ exchange current density for reaction K, A m^{-2}

$mass_n$ mass of species n, kg

$M_{m,dry}$ equivalent weight of a dry membrane, kg mol^{-1}

M_n molecular weight of species n, kg mol^{-1}

$m_{n,k}$ mass fraction of species n in stream k, dimensionless

$m_{w,l}$ mass fraction of liquid water

n_d electro osmotic drag coefficient (number of water carried per proton)

P	pressure, Pa
P_n	partial pressure of species n, Pa
$P^{sat}_{w,k}$	saturated vapor pressure of water in stream k, Pa
Q	volume flow rate, m^{-3} s^{-1}
R	universal gas constant, 8.314 J mol^{-1} K^{-1}
R	condensation rate, s^{-1}
S	source term
S_{h_e}	heat source term from electrochemical losses for energy equations
S_{h_p}	heat source term from water phase change for energy equations
T	temperature, K
$t_{f,a}$	liquid water film on the anode, m
$t_{f,c}$	liquid water film on the cathode, m
t_m	membrane thickness, m
u, v, w	velocities in x, y and z directions respectively, m s^{-1}
V_{cell}	cell voltage, V
V_{oc}	cell open circuit voltage, V
$X_{i,k}$	mole fraction of species I in stream k
X_L	channel length measured from anode inlet, m

Greek symbol

A	kinetic transfer coefficient for reaction K
$\alpha(x,y)$	net water flux per proton flux
$\beta\zeta$	permeability in the ζ direction
ε	porosity of gas diffusion layer
η	overpotential for oxygen reaction
λ	water content in the membrane
μ	dynamic viscosity, kg-s m^{-2}
ρ	density of the mixture, kg m^{-3}
$\rho_{m,dry}$	density of a dry membrane, kg m^{-3}
ρ_n	density of species n, kg m^{-3}
σ_m	membrane conductivity, S m^{-1}

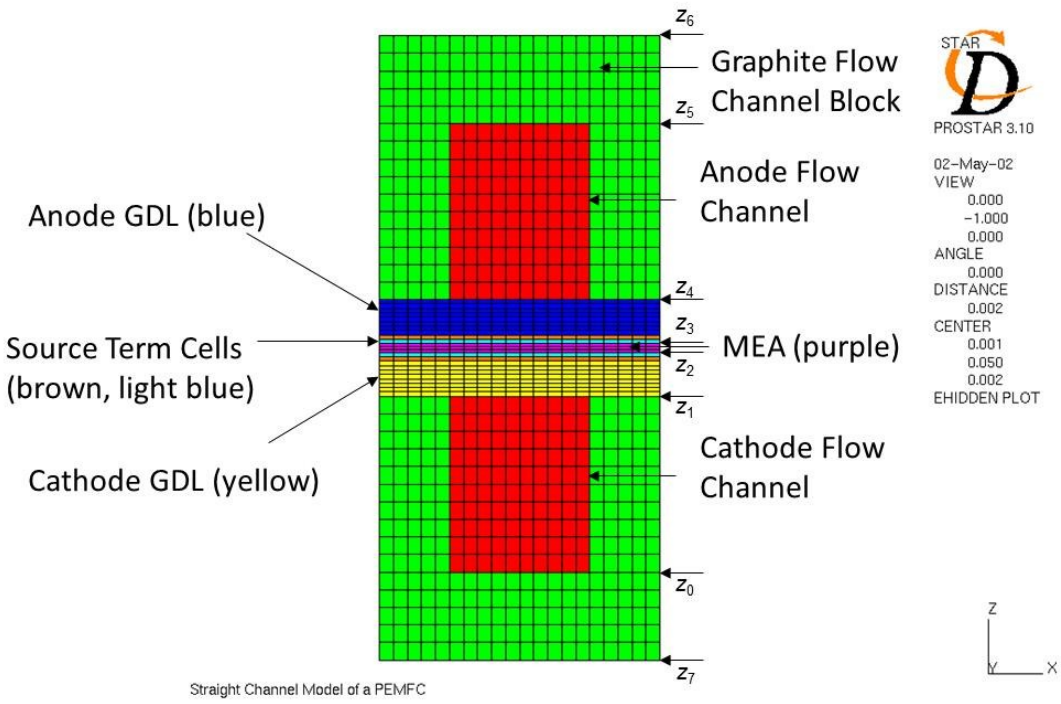

Figure A.1. The geometrical model of the fuel cell model.

APPENDIX B

MODELING RESULT OF UNDERSTANDING THE EFFECT OF CHANNEL TOLERANCES ON PERFORMANCE OF PEMFCS

The mathematical results of Chapter 3 have been shower in the table below. These results came from the modeling equation in Appendix A. The operating conditions were shown in Chapter 3.

Table B.1. The effect of draft angle on PEMFC performance result from Figure 3.6 the effect of draft angle on PEMFC performance.

Current density (A/cm^2)	Potential (V)							
	Stationary condition				Automotive condition			
Etch factor	STD	5	3.8	1.5	STD	5	3.8	1.5
0	0.960	0.960	0.960	0.960	0.960	0.960	0.960	0.960
0.1	0.740	0.732	0.740	0.730	0.765	0.770	0.765	0.770
0.2	0.675	0.660	0.675	0.663	0.720	0.718	0.710	0.712
0.4	0.600	0.598	0.600	0.591	0.643	0.640	0.640	0.625
0.6	0.550	0.553	0.550	0.545	0.580	0.580	0.575	0.555
0.8	0.512	0.512	0.510	0.493	0.517	0.515	0.505	0.485
1.0	0.480	0.478	0.470	0.435	0.450	0.440	0.430	0.410
1.2	0.440	0.435	0.420	0.360	0.385	0.375	0.370	0.335

Table B.2. The effect of draft angle on PEMFC performance result from Figure 3.10 the effect of channel radius on PEMFC performance.

Current density (A/cm^2)	Potential (V)							
	Stationary condition				Automotive condition			
Radius (mm)	STD	0.3	0.6	1.0	STD	0.3	0.6	1.0
0	0.960	0.960	0.960	0.960	0.960	0.960	0.960	0.960
0.1	0.740	0.740	0.720	0.720	0.765	0.769	0.770	0.770
0.2	0.675	0.650	0.660	0.660	0.720	0.718	0.715	0.715
0.4	0.600	0.598	0.595	0.594	0.643	0.640	0.643	0.643
0.6	0.550	0.550	0.550	0.550	0.580	0.585	0.582	0.585
0.8	0.512	0.513	0.512	0.512	0.517	0.520	0.515	0.521
1.0	0.480	0.480	0.472	0.472	0.450	0.445	0.440	0.455
1.2	0.440	0.443	0.434	0.435	0.385	0.387	0.385	0.390

Table B.3. The effect of draft angle on PEMFC performance result from Figure 3.10 the effect of channel radius on maximum pressure drop.

Current density (A/cm^2)	Pressure drop (Pa)							
	Stationary condition				Automotive condition			
Radius (mm)	STD	0.3	0.6	1.0	STD	0.3	0.6	1.0
0	0	0	0	0	0	0	0	0
0.1	39	37	39.41	39.88	10	9.5	9.5	9.535
0.2	77	78	78	78.07	19	19	19.3	19.42
0.4	157	156	156	157.5	40	40	39.6	39.84
0.6	239	238	239	239.7	61	61	60.6	60.97
0.8	322	321	321	322.2	83	82	82.3	82.7
1.0	406	404	406	406.4	105	105	105	105.6
1.2	493	491	492.5	493	129	128	128	128.6

Table B.4. The effect of draft angle on PEMFC performance result from Figure 3.11 the effect of channel radius on PEMFC performance.

Current density (A/cm^2)	Potential (V)									
	Stationary condition					Automotive condition				
Plate No.	#1	#2	#3	#4	#5	#1	#2	#3	#4	#5
0	0.960	0.960	0.960	0.960	0.960	0.960	0.960	0.960	0.960	0.960
0.1	0.733	0.730	0.722	0.730	0.730	0.773	0.770	0.770	0.770	0.730
0.2	0.672	0.670	0.670	0.660	0.662	0.718	0.710	0.715	0.712	0.662
0.4	0.605	0.600	0.600	0.605	0.602	0.633	0.630	0.631	0.635	0.602
0.6	0.560	0.555	0.558	0.558	0.552	0.565	0.565	0.565	0.565	0.552
0.8	0.525	0.525	0.525	0.530	0.527	0.505	0.505	0.505	0.505	0.527
1.0	0.486	0.490	0.498	0.500	0.490	0.445	0.440	0.440	0.440	0.490

Table B.5. The effect of draft angle on PEMFC performance result from Figure 3.11 the effect of channel radius on maximum pressure drop.

Current density (A/cm^2)	Pressure drop (Pa)									
	Stationary condition					Automotive condition				
Plate No.	#1	#2	#3	#4	#5	#1	#2	#3	#4	#5
0	0	0	0	0	0	0	0	0	0	0
0.1	2107	2360	2860	3234	2888	500	564	650	879	731
0.2	4362	4918	5823	6735	6067	1045	1186	1374	1780	1506
0.4	9636	10950	12950	14820	13410	2225	2505	2896	3370	3184
0.6	16010	18290	21710	24980	22500	3541	3988	4607	5178	5032
0.8	23540	27150	32690	37880	33730	4981	5622	6488	7310	7060
1.0	33150	38660	46520	54450	48000	6564	7427	8577	9653	9278

APPENDIX C

EXPERIMENTAL DATA OF FUNDAMENTAL ANALYSES, OBSERVATIONS, AND PREDICTIONS OF LIQUID DROPLET MOVEMENT ON ETCHED-METAL SURFACES FOR PEMFC

First, the liquid water droplets behaviors were analyzed thought the changing of contact angle. For example Figure C.1 illustrates the liquid water droplet in flow channel. When the droplet expose to the flowing stream in channel, the front edge of the droplet creeps forward while the rear edge remains still. As this occurs, the contact angle of the front edge (advancing contact angle) increase and the contact angle of the rear edge (receding contact angle) decrease. The liquid water droplet contact angles were taken at varies Reynolds numbers (200-1500) to measure the contact angles as shown in Figure C.2.

The effects of surface properties on the droplet behavior at different Reynolds numbers as shown in Table C.1 were extended the effort to include the effect of droplet size on its behavior. Force balance equations were analyzed to explain liquid droplet movement. The critical advancing and receding angles for the droplet movement are independent on the surface properties.

Table C.1. Drag force and pressure drop calculate at the critical point.

Surface roughness (RA)	Droplet height (mm)	Volume flow rate (ccm)	Reynolds's number	Drag force (N)	Pressure drop (Pa)
0.02μm	1.5	1500	555	3.81×10^{-4}	43.1
0.27μm	1.53	2000	740	5.66×10^{-4}	65.4
0.30μm	1.53	1500	555	4.64×10^{-4}	52.0
0.41μm	1.51	2500	925	6.40×10^{-4}	73.8
0.73μm	1.66	2000	740	1.25×10^{-3}	163.5

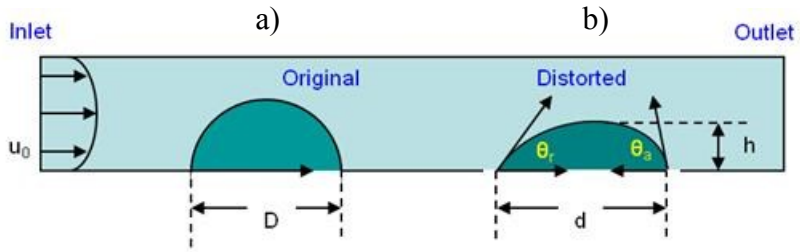

Figure C.1. Schematic side view of liquid droplet in flow channel a) without flow and b) with flow.

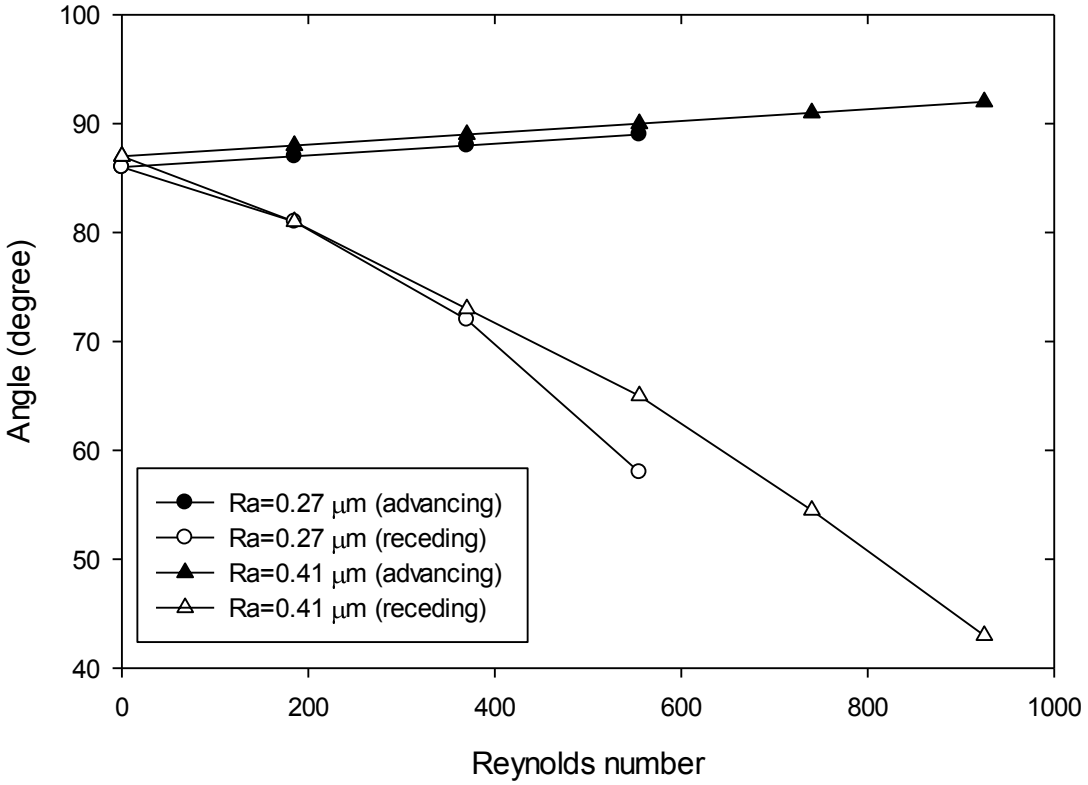

Figure C.2. Advansing and receding contact angle vs. Reynold's number (flow rate).

APPENDIX D

PARALLEL FLOW-FIELD PEMFCS (USC DESIGN)

The Serpentine flow-field, which is commonly used in PEMFC, has advantages of high performance and high utilizations of fuel gases, while it has penalty of high internal pressure drop and non-uniform flow distributions due to sharp turns of channel bend. Straight parallel flow-field can be an excellent candidate to get uniform flow distributions due to its compact design and for enhanced uniformity if it has uniform flow-field.

In order to get the uniform flow distribution, the effect of manifold designs to flow profiles and pressure distributions were studied. 50-cm^2 straight parallel PEMFC was designed and simulated by computational fluid dynamics (CFD) analysis considering electrochemical reaction. There are three significant geometrical factors were found as: (1) manifold inlet location; (2) manifold outlet location; (3) manifold inlet width. The optimized 50-cm^2 straight parallel PEMFC anode and cathode designed drawing are shown in Figure D.1 and D.2. Manifold inlet/outlet location and manifold inlet/outlet width were found as key factors. Cathode manifold inlet location and cathode manifold outlet location were found having opposite effect on the flow profiles. Uniform flow profiles were found when cathode manifold inlet width was large and anode manifold inlet location was located away from channel. These studies look forward to be useful information for the uniform flow design of straight parallel PEM fuel cells.

The optimum cell of straight parallel flow-field has been studied as shown in Table D.1. The optimum cell showed more uniform flow profiles compare to serpentine

cell. Moreover, the performance of optimum cell was observed slightly higher performance and more uniform temperature distribution than serpentine cell.

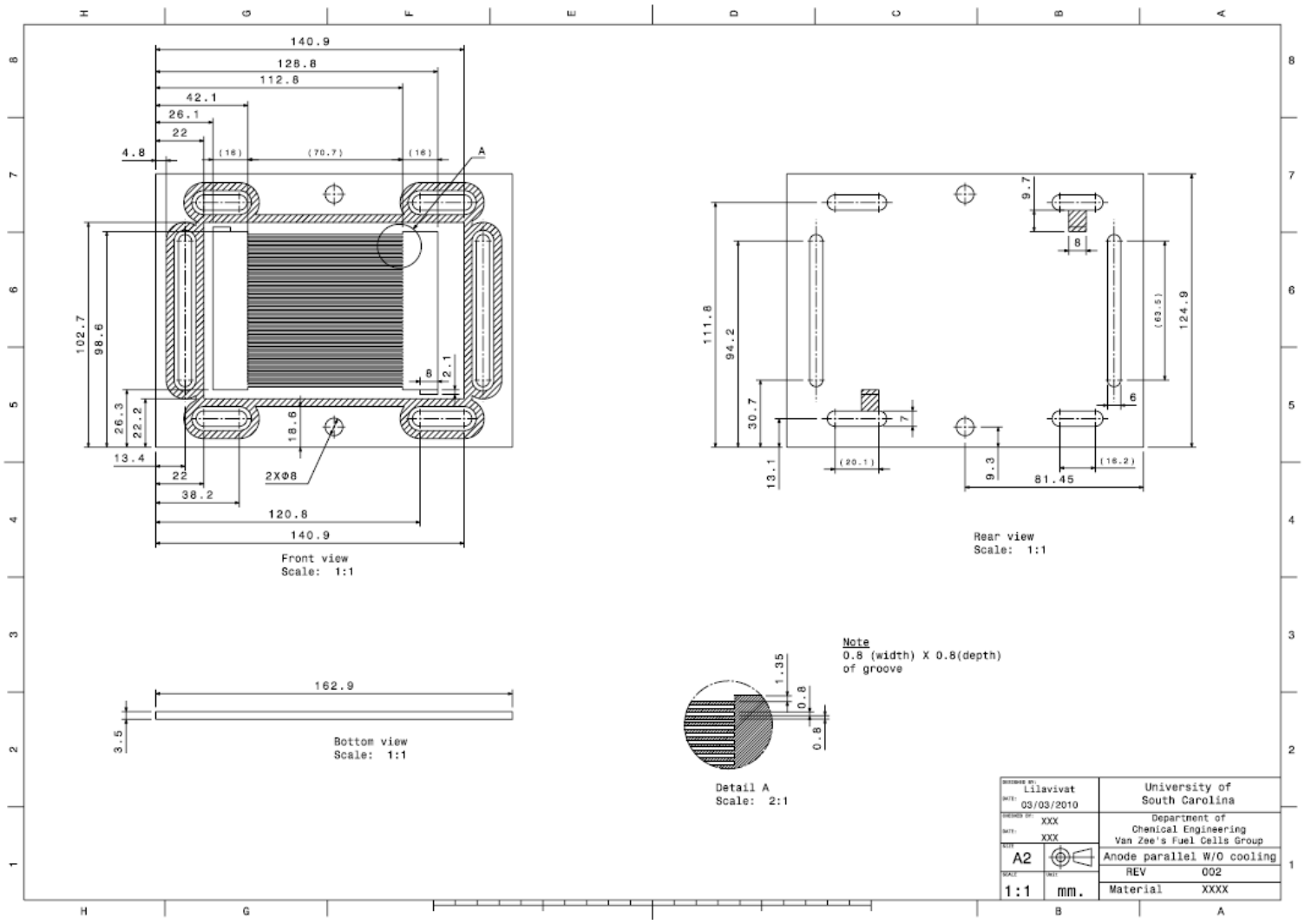

Figure D.1. Drawing of USC designed anode parallel flow field.

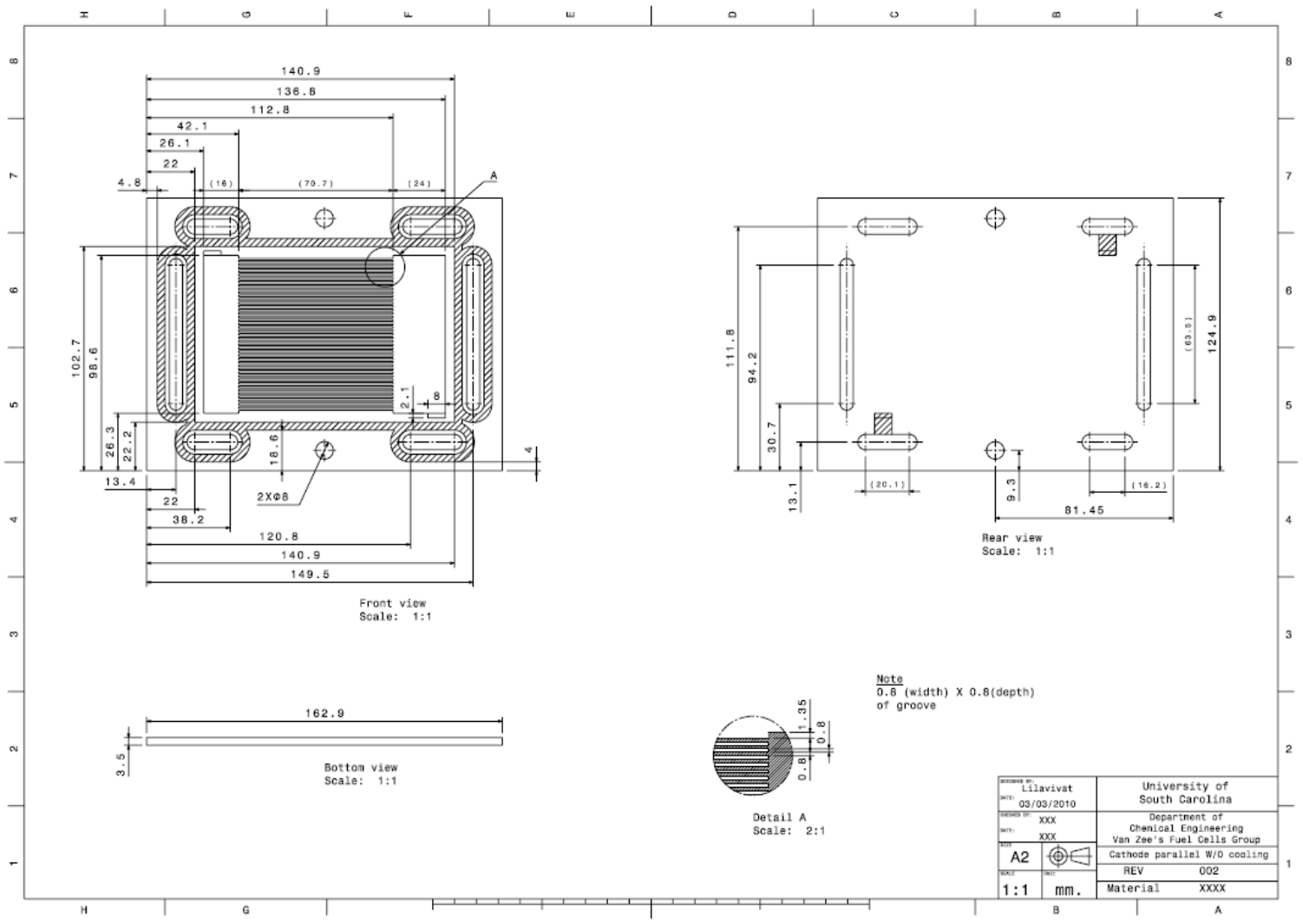

Figure D.2. Drawing of USC designed cathode parallel flow field

Table D.1. Comparison PEMFC flow-field design results.

	i_{avg} = 0.2 Acm^{-2}		i_{avg} = 0.6 Acm^{-2}		i_{avg} = 1.0 Acm^{-2}	
	V^{cell}(V)	T_{avg}(K)	V^{cell}(V)	T_{avg}(K)	V^{cell}(V)	T_{avg}(K)
Serpentine Cell	0.712	354.2	0.561	360.0	0.431	361.8
Optimum Cell	0.713	353.9	0.563	356.9	0.437	359.8

APPENDIX E

CURRENT SMEAR TEST

To verify the setup and testing method, a current smear test was used to collect the current distribution when using either a whole GDL or the GDL cut into 10 individual pieces. The purpose of the test was to observe if any current applied to one section would "smear" to another region due to the conductivity nature of the GDL. The test was conducted as illustrated in Figure E.1 where 3 Amps of current was applied to the top endplate via a DC power supply. A 1-mil Kapton® sheet with a cut-out window the size which matches to the each segment of CDB (1-10) was then placed between the endplate and the GDL. Finally the Current Distribution was placed under the GDL to observe the current distribution. The results when using a whole GDL are shown on Figure E.2. Although 3 Amps were applied to the endplate, a significant amount of this current was able to travel laterally through the thickness of the GDL leading to current "smearing." The most significant amount of the current "smearing" is observed when applying current through the middle regions such as 2-4 and 7-9.

When the GDL is cut into 10 individual pieces, we observed that the lateral resistance through the thickness of the GDL (horizontal) was much greater than the resistance through the GDL (vertical) due to the slight physical separation of each individual GDL piece. Thus we are able to observe the current run vertically as illustrated in Figure E.3 without any observed current "smearing". The results from the 10

individually cut GDL pieces experiment with the cutout Kapton® window justifies cutting the GDL. When 3 Amps was applied to a single region, the current was observed and recorded with the results showing a maximum of 0.9% error to the true applied current of 3 Amps.

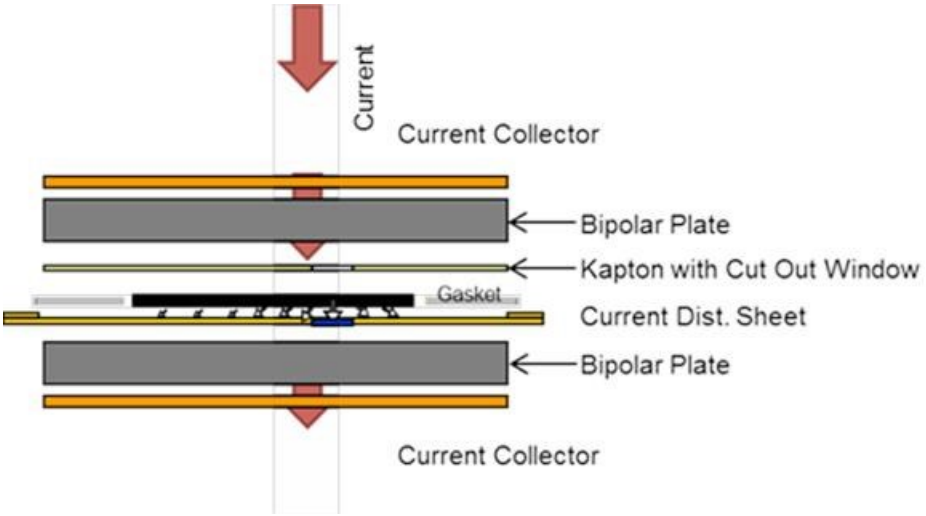

Figure E.1. Schematic of current smear test.

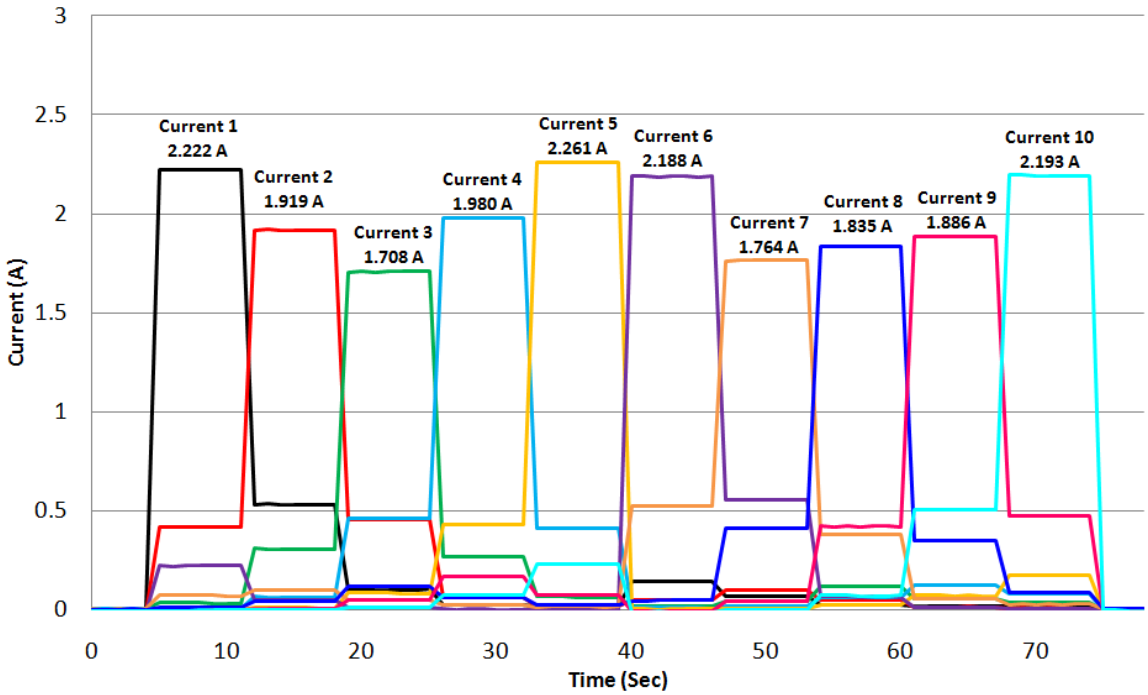

Figure E.2. Results of the cutout “window” current distribution with whole GDL with 3 Amps applied from DC power supply.

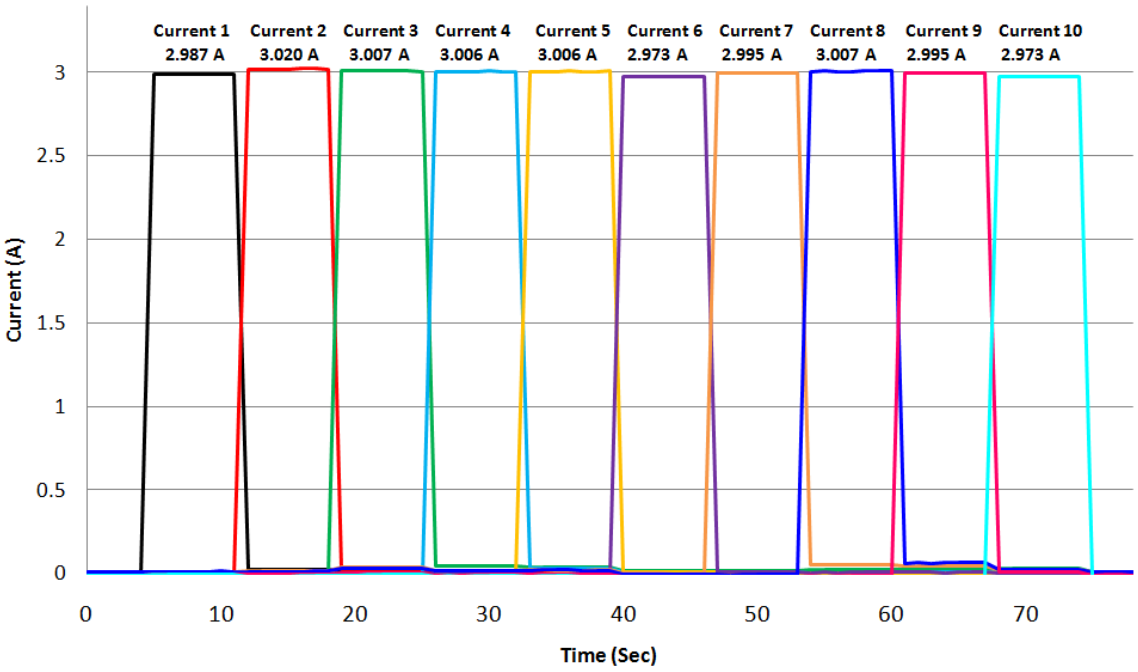

Figure E.3. Results of the cutout "window" current distribution with 10 individually cut GDL pieces with 3 Amps applied from DC power supply.

APPENDIX F

WATER BALANCE EXPERIMENT

The water balance experimental setup is shown in Figure F.1. The gas outlets from the fuel cell are connecting to the flexible tube. These tubes are connected to the flasks placed on the scale for measuring the liquid water exiting the fuel cell. Most of the water that exits fuel cell was condensed and collected in the flask bottle which shown in Figure F.2. The rest of water that is still in vapor form will flow pass though the humidity chamber which can measure dew point temperature. The thermocouples measured the outlet gas temperature. The water vapor coming in and out rate can be calculated from ideal gas law following:

$$Q_{water} = Q \times \frac{P_{water}}{P_{Tot} - P_{water}} \tag{F.1}$$

$$\dot{m}_{water} = \frac{P_{Tot} Q_{water}}{RT} \tag{F.2}$$

where Q is volume flow rate of gas, Q_{water} is volume flow rate of water, P_{Tot} is total pressure, P_{water} is partial pressure of water which can be calculated from dew point temperature, $\dot{m}_{water}$ is mass flow rate of water, R is gas constant, and T is temperature.

The overall water balance results from the water balance on the fuel cell are shown in Table F.1 and F.2 for Hydrocarbon membrane (BPSH-6FPAEB 7K-7K) and Nefion® membrane (NRE212). The water coming into the cell rate was calculated from the known relative humidity set point with Equation F.1 and F.2. The water coming out

rate was calculated from the slope of water balance data that measured from the scale (Figure F.2) plus the calculated from the known relative humidity outlet. The error in Table F.1 is the difference of water cross to cathode at anode side and water cross from anode at cathode side.

Table F.1. Water balance measeurment under different condition of hydrocarbon membrane (BPSH-6FPAEB 7K-7K).

	i (A/cm^2)	RH	Anode water balance (mg/sec)			Cathode water balance (mg/sec)				Error (%)
			Water in	Water out	Cross to cathode	Water in	Gen.	Water out	Cross from anode	
EXP	0.4	72/25	0.75	0.22	0.53	0.59	0.93	2.01	0.49	7.5
CFD	0.4	75/25	0.75	0.23	0.52	0.59	0.93	2.03	0.51	2.0
EXP	0.6	75/25	1.12	0.33	0.79	0.88	1.40	3.09	0.81	2.5
CFD	0.6	75/25	1.12	0.31	0.81	0.88	1.40	3.13	0.85	4.7
EXP	0.4	50/50	0.42	0.29	0.13	1.35	0.93	2.42	0.14	7.1
CFD	0.4	50/50	0.42	0.29	0.13	1.35	0.93	2.40	0.12	8.3
EXP	0.8	50/50	0.85	0.55	0.30	2.70	1.87	4.88	0.31	3.2
CFD	0.8	50/50	0.85	0.58	0.27	2.70	1.87	4.85	0.28	3.5
EXP	0.4	95/95	1.10	0.86	0.25	3.51	0.93	4.73	0.29	13.7
CFD	0.4	95/95	1.10	0.90	0.20	3.51	0.93	4.66	0.22	9.0
EXP	0.8	95/95	2.21	1.68	0.53	7.03	1.87	9.44	0.54	1.8
CFD	0.8	95/95	2.21	1.66	0.55	7.03	1.87	9.45	0.55	0.0
EXP	1.2	95/95	3.32	1.99	1.34	10.55	2.80	14.60	1.25	7.5
CFD	1.2	95/95	3.32	2.01	1.31	10.55	2.80	14.72	1.37	4.4

(80˚C, 1.5/2.0 stoichiometry ratio H_2/Air)

Table F.2. Water balance measeurment under different condition of Nefion® membrane (NRE212).

	i (A/cm^2)	RH	Anode water balance (mg/sec)			Cathode water balance (mg/sec)				Error (%)
			Water in	Water out	Cross to cathode	Water in	Gen.	Water out	Cross from anode	
EXP	0.4	25/25	0.37	0.42	-0.2	1.15	1.87	2.81	-0.21	4.6
CFD	0.4	25/25	0.37	0.52	-0.15	1.15	1.87	2.85	-0.17	10
EXP	0.4	75/25	1.5	0.55	0.94	1.15	1.87	3.79	0.91	3.8
CFD	0.4	75/25	1.5	0.53	0.97	1.15	1.87	4	0.98	1
EXP	0.6	75/25	2.25	0.87	1.38	1.7	2.8	5.8	1.3	5.9
CFD	0.6	75/25	2.25	0.81	1.44	1.7	2.8	6	1.5	4
NRE	0.4	95/95	1.1	0.65	0.45	3.51	0.93	4.91	0.47	4.2
CFD	0.4	95/95	1.1	0.64	0.46	3.51	0.93	4.91	0.47	2.1
NRE	0.6	95/95	1.66	1.00	0.66	5.26	1.4	7.36	0.70	5.7
CFD	0.6	95/95	1.66	0.98	0.68	5.26	1.4	7.35	0.69	1.5
NRE	0.8	95/95	2.21	1.35	0.86	7.03	1.87	9.8	0.9	4.4
CFD	0.8	95/95	2.21	1.36	0.85	7.03	1.87	9.74	0.84	1.2

(80˚C, 1.5/2.0 stoichiometry ratio H_2/Air)

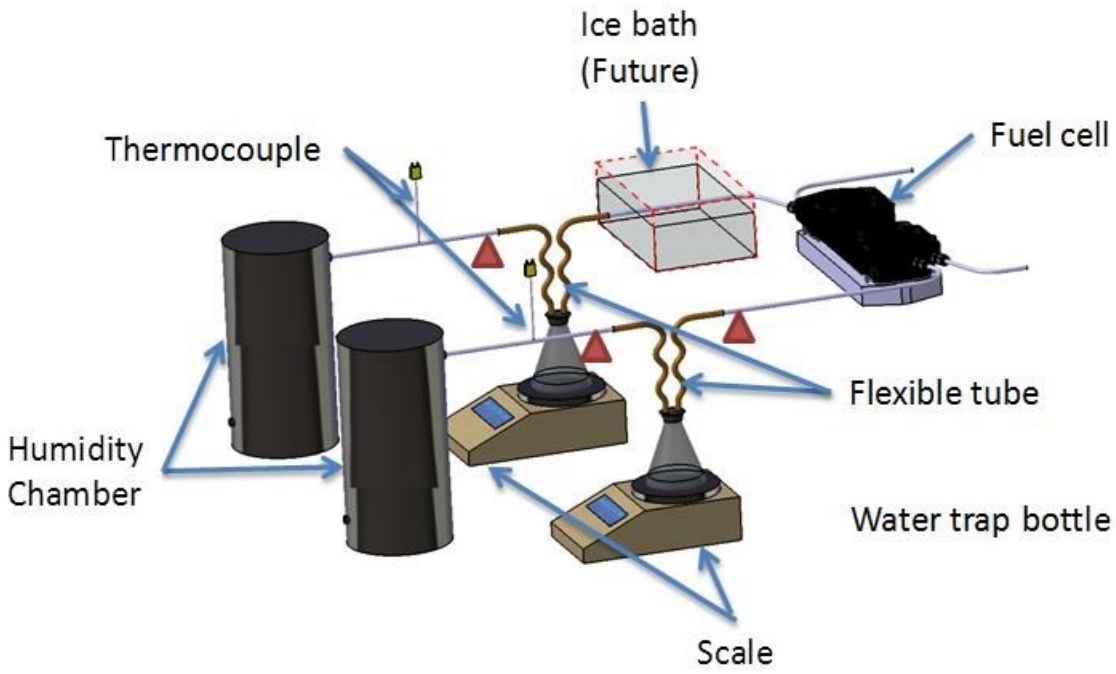

Figure F.1 Water balance experimental setup.

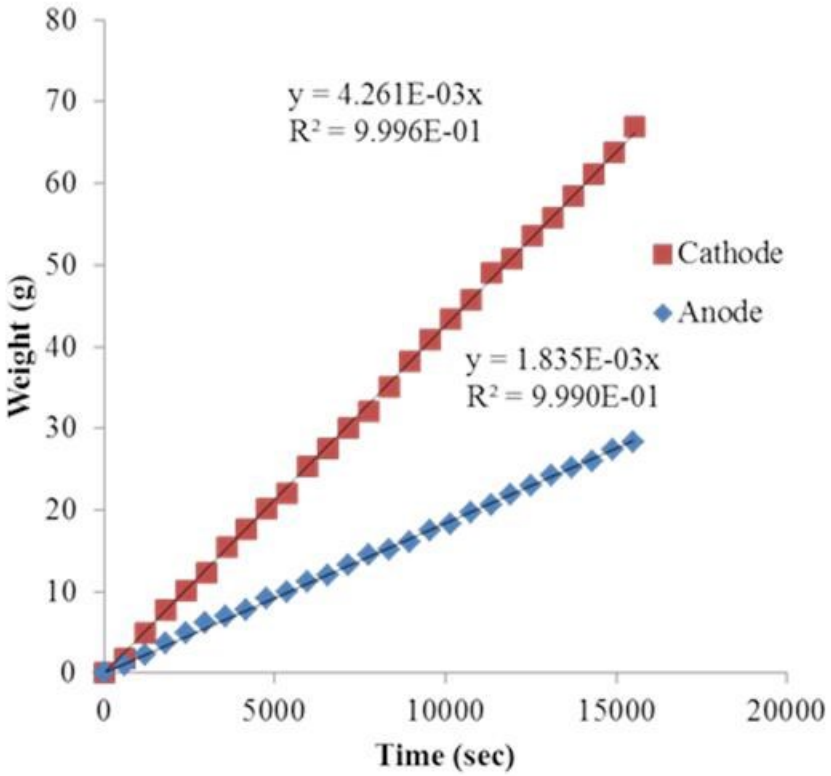

Figure F.2. Example water weight collecting result from scale.

APPENDIX G

MEMBRANE CHARACTERIZATION AND EXPERIMENTAL SETUP

This appendix is included for completeness. Data for the water diffusion coefficients and electroosmotic drag were obtained at Giner Electrochemical Systems, LLC, and used the techniques and apparatus discussed below. Those data were used in the CFD model to calculate the predictions of the water balance as shown in Table F.1 and F.2. Those data are summarized and shown in Table G.1:

G.1 Water uptake and diffusivity

The technique to measured water uptake and diffusion coefficient was developed by Mittelsteadt [114] which can eliminate gas/gas diffusion for more effective process. The membrane was placed in a vacuum chamber of known volume which removes all gas/gas diffusion. Then a known amount of water vapor was added into the chamber. The chamber pressure initially increases with the added vapor, then decreases as the membrane absorbs water. The rate of water absorption by the membrane can be calculated by measuring the decrease of pressure in the chamber. By knowing the weight and the amount of water vapor added to the chamber thus, the water uptake isotherm and diffusivity can be obtained. Figure 6.2 a) and b) shows the membrane water content and diffusion coefficient.

G.2 Electro-Osmotic Drag Coefficient (EODC)

The EODC measuring technique was developed by Braff and Mittelsteadt [115, 116]. The EODC characterization was measured by a dead-ended hydrogen pump which effectively decoupled the diffusion from EODC. The dead-end hydrogen pump is further modified in a way that water vapor condensation has been eliminated and thus the EODC can be attained at more precisely controlled relative humidifies. The Nafion® membranes and hydrocarbon membranes supplied by Virginia Tech have also been characterized using this system as shown in Figure 6.2 c).

G.3 Proton conductivity

The proton conductivities of the membranes were measured by an AC impedance spectroscopy .The conductivity σ of samples in the transverse direction was calculated from the impedance data, using the relationship:

$$\sigma = \frac{d}{RS} \qquad \text{(G.1)}$$

where d is the thickness, S is face area of the membrane, and R was derived from the low intersection of the high frequency semi-circle on a complex impedance plane with the Re(Z) axis.

Table G.1. Equations for modeling from experiment

Description	Mathematical expression	
Water content in the membrane	$\lambda = -5.49 + 0.50RH - 0.0096RH^2 + 6.55 \times 10^{-5}RH^3$	(Hydrocarbon)
	$\lambda = 0.134RH - 1.89 \times 10^{-3}RH^2 + 1.42 \times 10^{-5}RH^3$	(Nefion®)
Electro-osmotic drag coefficient	$EODC = 0.1371 + 0.0118\lambda + 0.0104\lambda^2 - 0.0005\lambda^3$	(Hydrocarbon)
	$EODC = 0.0849 + 0.2078\lambda - 0.0018\lambda^2 - 0.0005\lambda^3$	(Nefion®)

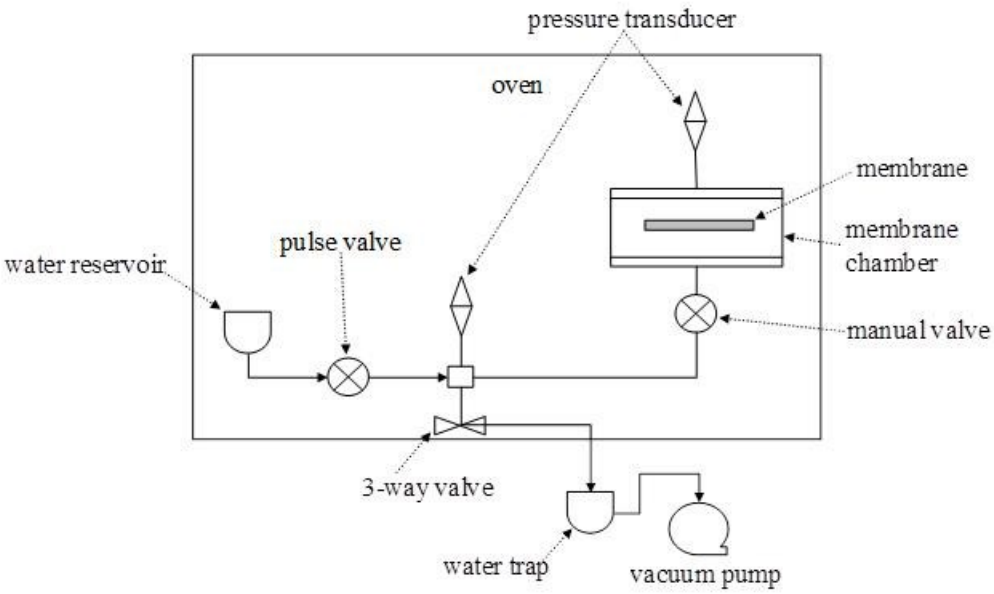

Figure G.1. Schematic of experiemtal setup to measure mambreane water uptake and water diffusivity [114].

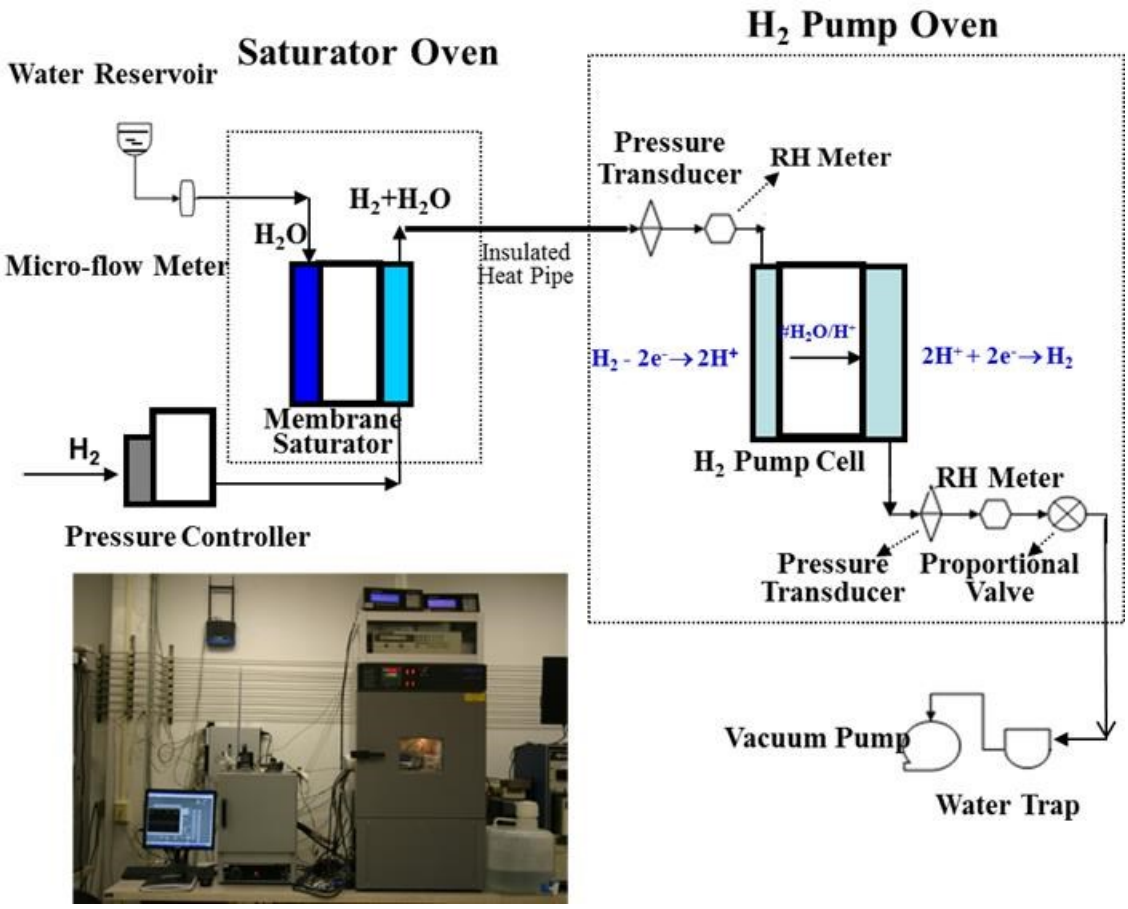

Figure G.2 Schematic of experiemtal setup to measure EODC of membrane [116].

APPENDIX H

MEMBRANE STRUCTURE AND PROPERTIES

The McGrath group at VA Tech has developed a procedure for the 6FPAEB-BPS100 copolymer synthesis, which enables to simplify the synthesis of the copolymer in a comparison with previous two-oligomer approach. Second, 6FxBP100-xPAEB oligomers with different composition of 6F-BisA have been successfully synthesized and the structure of 6FxBP100-xPAEB oligomers has been confirmed by 1H- NMR; the 6F-BisA was introduced to reduce the cost and permeability of the membranes. Finally, 6FxBP100-xPAEB-BPS100 multiblock copolymers have been synthesized. The properties of their membranes like conductivity and diffusivity will be also used in modeling work at USC to investigate the fuel cell performance, water distribution and current distribution. The procedure for synthesizing 6FPAEB-BPS100 copolymers is shown in Figure H.1.

Based on 6FPAEB and HQS100 oligomers, the McGrath group at VA Tech successfully synthesized block copolymer HQS100-6FPAEB via low temperature coupling reactions as shown in Figure H.2. They obtained the copolymers with a variety of molecular weights, from 6K-6K, 9K-9K, ro 11K-11K. They subsequently characterized these block copolymer, water uptake, ion exchange capacity (IEC), and proton conductivity. The water transport properties of 6K-6K 6FPAEB-HQS100 block copolymers are listed in Table H.1 in comparison with BPSH-6FPAEB copolymers and Nafion 212.

Figure H.3 shows the diffusivities of Giner Cast BPSH-6FPAEB 7K-7K at 80^{o}C. A few observations can be made here. The effective area of the membrane was 50 cm^{2}. First, the diffusivities of Giner Cast BPSH-6FPAEB 7K-7K membranes demonstrate very good reproducibility, regardless of measurent approaches (dynamic water uptake and steady state water uptake) and membrane thickness (3 mil and 1.5-2 mil). Second, the diffusivity of 7k-7k BPSH-6FPAEB membrane is 2 times lower than that of Nafion membranes. The lower water diffusivity of VA Tech membranes may be due to the aromatic sulfonic acid group binding the water more tightly at lower RH than the Nafion membrane.

The EODC of a series of VA Tech membranes has been characterized using a dead-end hydrogen pump system developed as discussed in Appendix G. Figure H.4 shows the result that 6FPAEB-BPSH100 membranes exhibit lower EODC than the baseline (Nafion 112 membrane). The lower EODC could be due to their difference in crosslink, phase segregation or other structure and properties.

Table H.1. Water transport properties of HQSH-6FPAEN

BPSH-6FPAEB	IEC (meq/g)[a]	Water uptake (%)	Proton Conductivity (S/cm)[b]
7K-7K	1.55	42	0.13
9K-9K	1.53	44	0.14
13K-13K	1.60	51	0.15
15K-15K	1.55	46	0.16
HQSH-6FPAEB			
6K-6K	1.76	49	0.15
9K-9K	1.65	55	0.15
11K-11K	1.50	64	0.15
Nafion 212	0.90	22	0.12

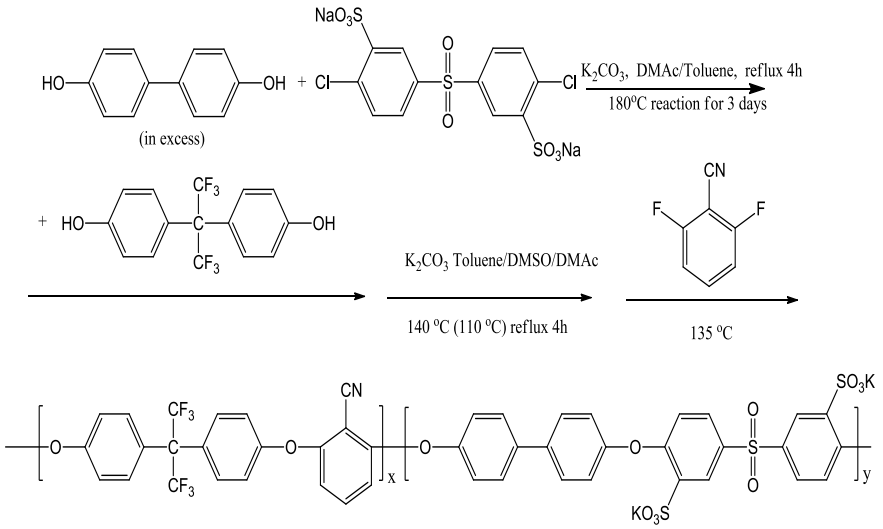

Figure H.1. Synthetic routes for 6FPAEB-BPS100 copolymers[117].

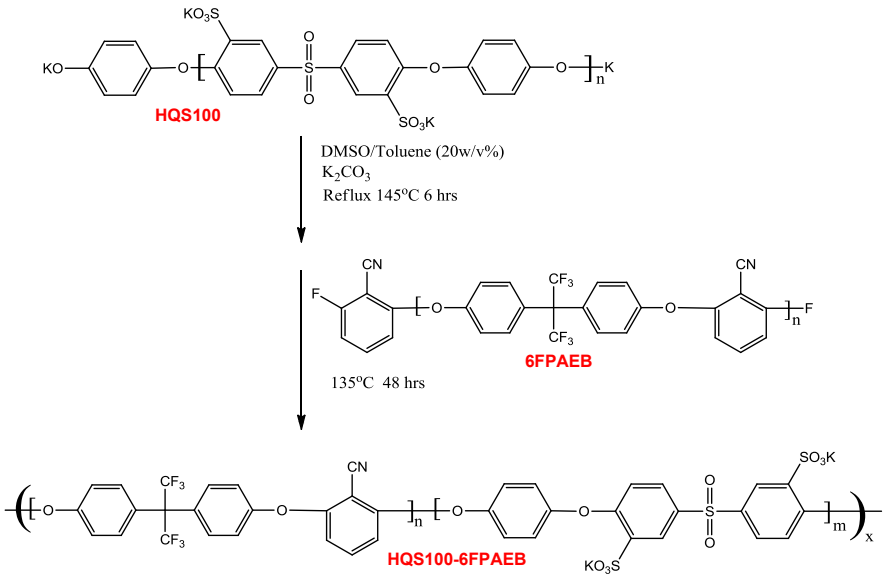

Figure H.2. Synthetic routes for 6FPAEB-HQS1000 Coupling Reactions[117].

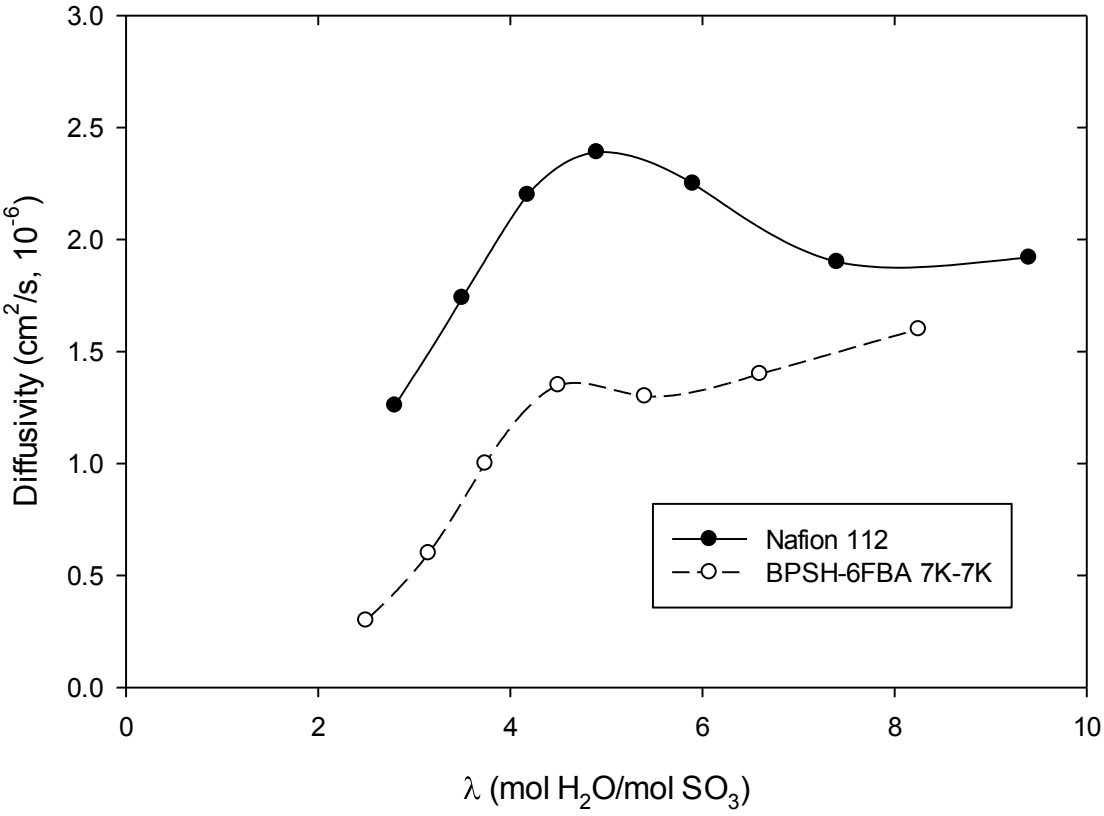

Figure H.3. Diffusivity: Nafion 112 vs. Giner Cast BPSH-6FPAEB 7K-7K (80˚C)

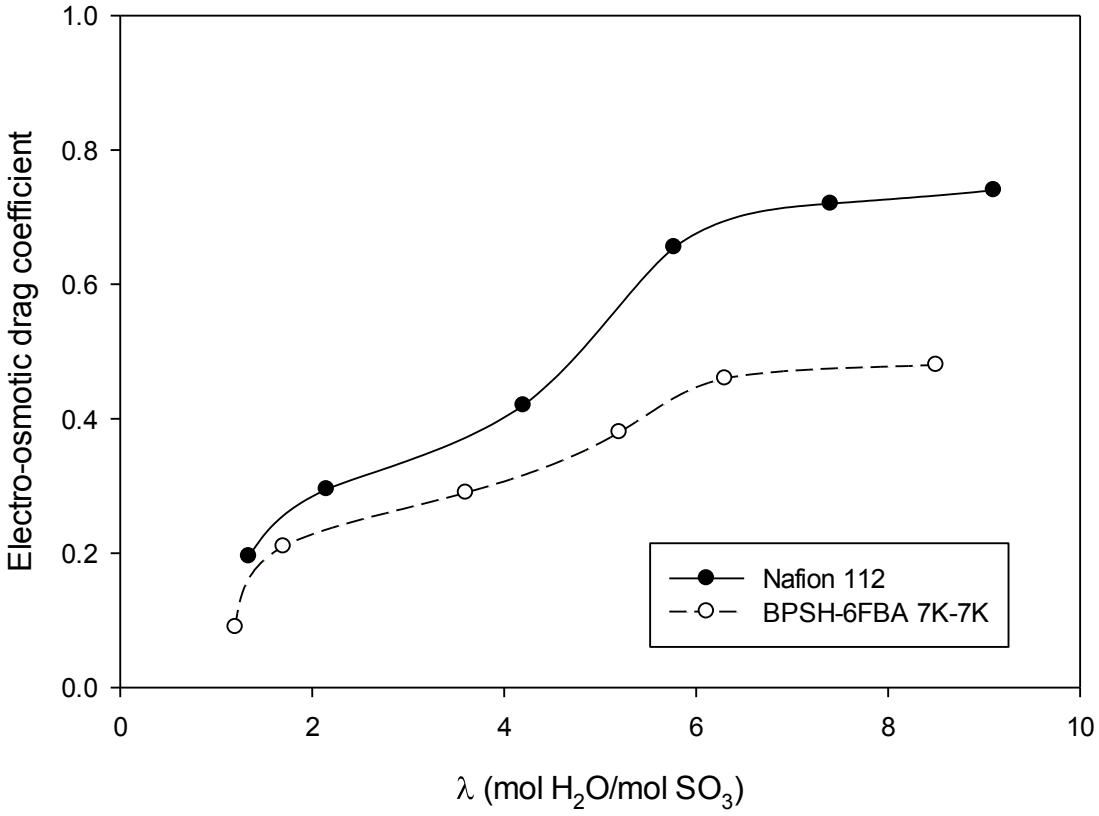

Figure H.4. EODC as a function of water uptake for a various membranes

VITA

Mr. Visarn Lilavivat was born in Bangkok, Thailand on the 17th April 1983. He was awarded the degree of Bachelor of Mechanical Engineering at Chulalongkorn University in 2005. After graduation he worked in Isuzu Technical Center Asia Co, Ltd. as a designed engineering. After two year of designed work, he was awarded a Royal Thai Scholarship to study for a higher degree in the engineering field.

Mr. Lilavivat came to study in Ph.D. in Chemical Engineering at University of South Carolina with Professor John W. Van Zee of the Chemical Engineering Department of University of South Carolina with the help of Dr. Sirivatch Shimpalee, Research Associate Professor.

Permanent Mailing Address

Visarn Lilavivat

99/11 Ratchadapisek 44 Rd.

Bangkok 10900